Geophysical Journal International

Geophys. J. Int. (2022) **230,** 392–426
Advance Access publication 2022 January 05
GJI Seismology

https://doi.org/10.1093/gji/ggab533

High-rate very-long-period seismicity at Yasur volcano, Vanuatu: source mechanism and decoupling from surficial explosions and infrasound

Robin S. Matoza [1], Bernard A. Chouet [2], Arthur D. Jolly [3,4], Phillip B. Dawson [5], Rebecca H. Fitzgerald [3,6], Ben M. Kennedy,[6] David Fee [7], Alexandra M. Iezzi [1], Geoff N. Kilgour,[8] Esline Garaebiti[9] and Sandrine Cevuard[9]

[1] *Department of Earth Science and Earth Research Institute, University of California, Santa Barbara, CA 93106, USA. E-mail: rmatoza@ucsb.edu*
[2] *Arzier-Le Muids, Switzerland*
[3] *GNS Science, Lower Hutt, New Zealand*
[4] *U.S. Geological Survey, Hawaiian Volcano Observatory, Hilo, HI, USA*
[5] *U.S. Geological Survey, Moffett Field, CA, USA*
[6] *The School of the Earth and Environment, University of Canterbury, Christchurch, New Zealand*
[7] *Alaska Volcano Observatory and Wilson Alaska Technical Center, Geophysical Institute, University of Alaska Fairbanks, Fairbanks, AK, USA*
[8] *GNS Science, Wairakei Research Centre, Taupo, New Zealand*
[9] *Vanuatu Meteorology and Geohazards Department, Port Vila, Vanuatu*

Accepted 2022 0. Received 2021 December 4; in original form 2021 July 27

SUMMARY

Yasur volcano, Vanuatu is a continuously active open-vent basaltic-andesite stratocone with persistent and long-lived eruptive activity. We present results from a seismo-acoustic field experiment at Yasur, providing locally dense broad-band seismic and infrasonic network coverage from 2016 July 27 to August 3. We corroborate our seismo-acoustic observations with coincident video data from cameras deployed at the crater and on an unoccupied aircraft system (UAS). The waveforms contain a profusion of signals reflecting Yasur's rapidly occurring and persistent explosive activity. The typical infrasonic signature of Yasur explosions is a classic short-duration and often asymmetric explosion waveform characterized by a sharp compressive onset and wideband frequency content. The dominant seismic signals are numerous repetitive very-long-period (VLP) signals with periods of ∼2–10 s. The VLP seismic events are 'high-rate', reoccurring near-continuously throughout the data set with short interevent times (∼20–60 s). We observe variability in the synchronization of seismic VLP and acoustic sources. Explosion events clearly delineated by infrasonic waveforms are underlain by seismic VLPs. However, strong seismic VLPs also occur with only a weak infrasonic expression. Multiplet analysis of the seismic VLPs reveals a systematic progression in the seismo-acoustic source decoupling. The same dominant seismic VLP multiplet occurs with and without surficial explosions and infrasound, and these transitions occur over a timescale of a few days during our field campaign. We subsequently employ template matching, stacking, and full-waveform inversion to image the source mechanism of the dominant VLP multiplet. Inversion of the dominant VLP multiplet stack points to a composite source consisting of either a dual-crack (plus forces) or pipe-crack (plus forces) mechanism. The derived mechanisms correspond to a point-source directly beneath the summit vents with centroid depths in the range ∼900–1000 m below topography. All mechanisms suggest a northeast trending crack dipping relatively shallowly to the northwest and indicate a VLP source centroid and mechanism controlled by a stable structural geologic feature beneath Yasur. We interpret the results in the framework of gas slug ascent through the conduit responsible for Yasur explosions. The VLP mechanism and timing with infrasound (when present) are explained by a shallow-buffered top-down model in which slug ascent is relatively aseismic until reaching the base of a shallow section. Slug disruption in this shallow zone triggers a pressure disturbance that propagates downward

and couples at the conduit base (VLP centroid). If the shallow section is open, an explosion propagates to the surface, producing infrasound. In the case of (the same multiplet) VLPs occurring without surficial explosions and weak or no infrasound, the decoupling of the dominant VLPs at ∼900–1000 m depth from surficial explosions and infrasound strongly indicates buffering of the terminal slug ascent. This buffering could be achieved by a variety of conditions at or directly beneath the vents, such as a high-viscosity layer of crystal-rich magma, a debris cap from backfill, a foam layer, or a combination of these. The dominant VLP at Yasur captured by our experiment has a source depth and mechanism separated from surface processes and is stable over time.

Key words: Earthquake source observations; Volcano seismology; Atmospheric effects (volcano); Eruption mechanisms and flow emplacement; Explosive volcanism; Magma migration and fragmentation.

1 INTRODUCTION

Yasur (19.532°S, 169.447°E), southeastern Tanna Island, in the southern Vanuatu volcanic arc (Figs 1a and b), is a continuously active open-vent basaltic-andesite volcano (Carney & McFarlane 1979; Nairn *et al.* 1988; Vergniolle & Métrich 2016). Activity at Yasur is characterized by frequent strombolian (typically every ∼1–5 min) to vulcanian explosions accompanied by ballistics and ash emissions (ash-rich or ash-poor), with persistent degassing and spattering (mean SO_2 emission rate of 633 Mg d^{-1}; Bani *et al.* 2012), and occasional larger (subplinian) eruptions (Nairn *et al.* 1988; Oppenheimer *et al.* 2006; Bani *et al.* 2013; Gaudin *et al.* 2014; Meier *et al.* 2016; Fitzgerald *et al.* 2020; Simons *et al.* 2020a). Yasur is a post-caldera pyroclastic cone (summit elevation 361 m above sea level) constructed within Siwi caldera (Fig. 1c), which formed during a moderate volume (1–2 km^3) ignimbrite-producing eruption probably less than 20 kyr ago (Nairn *et al.* 1988; Allen 2004; Métrich *et al.* 2011). The horseshoe-shaped Siwi caldera is bound on land by ring fractures and the central caldera floor has undergone rapid resurgence (uplift of ∼0.16 m yr^{-1} over the past 1000 yr) resulting in the Yenkahe resurgent dome; Yasur occupies the northwestern portion of the Yenkahe resurgent dome (Chen *et al.* 1995; Brothelande *et al.* 2016b, a). The present Yasur cone likely began to grow about 800 yr ago by deposition of ash, coarse lapilli, bombs and lavas of basaltic-trachyandesite composition on an ash plain extending 1–3 km beyond the main vent within Siwi caldera (Métrich *et al.* 2011).

Yasur is a site of remarkably persistent and long-lived eruptive activity; near-continuous strombolian and vulcanian activity is indicated by intermittent European historical documentation beginning in 1774 and is confirmed by continuous monitoring since the mid-twentieth century (Firth *et al.* 2014). Tephra analyses suggest that the current eruption style at Yasur has persisted in an approximately steady state for the last 630–850 yr, while Yasur eruptive history with greater variability and irregularity extends to ∼1400 yr before present (Firth *et al.* 2014). At the time of our field experiment in 2016 (Fig. 1d), the Yasur cone summit region consisted of a crater of 660 m diameter divided into two subcraters with three main vent areas (vents A and B in the southern subcrater, and vent C in the northern subcrater; Fitzgerald *et al.* 2020). The positions of the multiple active closely spaced vents migrate over time (Simons *et al.* 2020b) and are named differently in the literature; thus we refer simply to North and South Crater (Jolly *et al.* 2017). The multiple vents are thought to originate from a single homogeneous magma supply (Kremers *et al.* 2012, 2013), possibly with branching conduits or dikes at shallow levels (Simons *et al.* 2020b).

In comparison to such longevity of eruptive history, campaign geophysical deployments capture a brief snapshot of eruptive phenomena, yet enable an important quantitative window into the mechanics of subsurface magma movement and eruption (Chouet & Matoza 2013; Kawakatsu & Yamamoto 2015; Matoza *et al.* 2019a, *and references therein*). At present, the local permanent geophysical monitoring network at Yasur consists of a single short-period seismometer, while long-range infrasound from continuous Yasur eruptive activity has been recorded for decades at the permanent International Monitoring System (IMS) infrasound array IS22, New Caledonia at ∼400 km range (Le Pichon *et al.* 2005; Antier *et al.* 2007; Le Pichon *et al.* 2010). Additional temporary local seismic, acoustic, and multiparametric field deployments have elucidated various aspects of Yasur's seismo-acoustic wavefield (e.g. Nabyl *et al.* 1997; Battaglia *et al.* 2012; Perrier *et al.* 2012; Battaglia *et al.* 2013; Kremers *et al.* 2013; Marchetti *et al.* 2013; Battaglia *et al.* 2016; Meier *et al.* 2016; Spina *et al.* 2016b).

Here we present data from a multiparametric field campaign at Yasur providing temporary but locally dense broad-band seismic and infrasonic network coverage from 2016 July 27 to August 3 (Fig. 1). In comparison to previous studies, we deployed a greater number of broad-band seismic and infrasound instrumentation with higher spatial density concentrated locally around Yasur. The broad-band seismic network geometry permits recovery of the source mechanism of high-rate repetitive very-long-period (VLP) (∼2 to 10 s period) seismic events through full-waveform inversion. The broad-band and high-dynamic range seismo-acoustic instrumentation recorded at relatively high sample rate (seismic 200 Hz sample rate; infrasound 400 Hz sample rate) capture Yasur explosion seismo-acoustics with unprecedented fidelity, which we compare with coincident video data from cameras deployed at the crater and on an unoccupied aircraft system (UAS; Fitzgerald *et al.* 2020).

2 TEMPORARY BROAD-BAND SEISMO-ACOUSTIC NETWORK

We conducted a collaborative multiparametric field experiment at Yasur from 2016 July 27 to August 3 (Fig. 1; Matoza *et al.* 2017). Analyses of a subset of the acoustic (infrasound) data from our experiment were previously reported by Jolly *et al.* (2017), Iezzi *et al.* (2019) and Fee *et al.* (2021). Here we focus on data from a temporary network of eight broad-band seismometers, six single infrasound stations and two 3-element infrasound line arrays (Fig. 1). Each seismic station (YS, Fig. 1) consisted of a three-component 120-s Trillium Compact Posthole (Nanometrics) seismometer sampled at

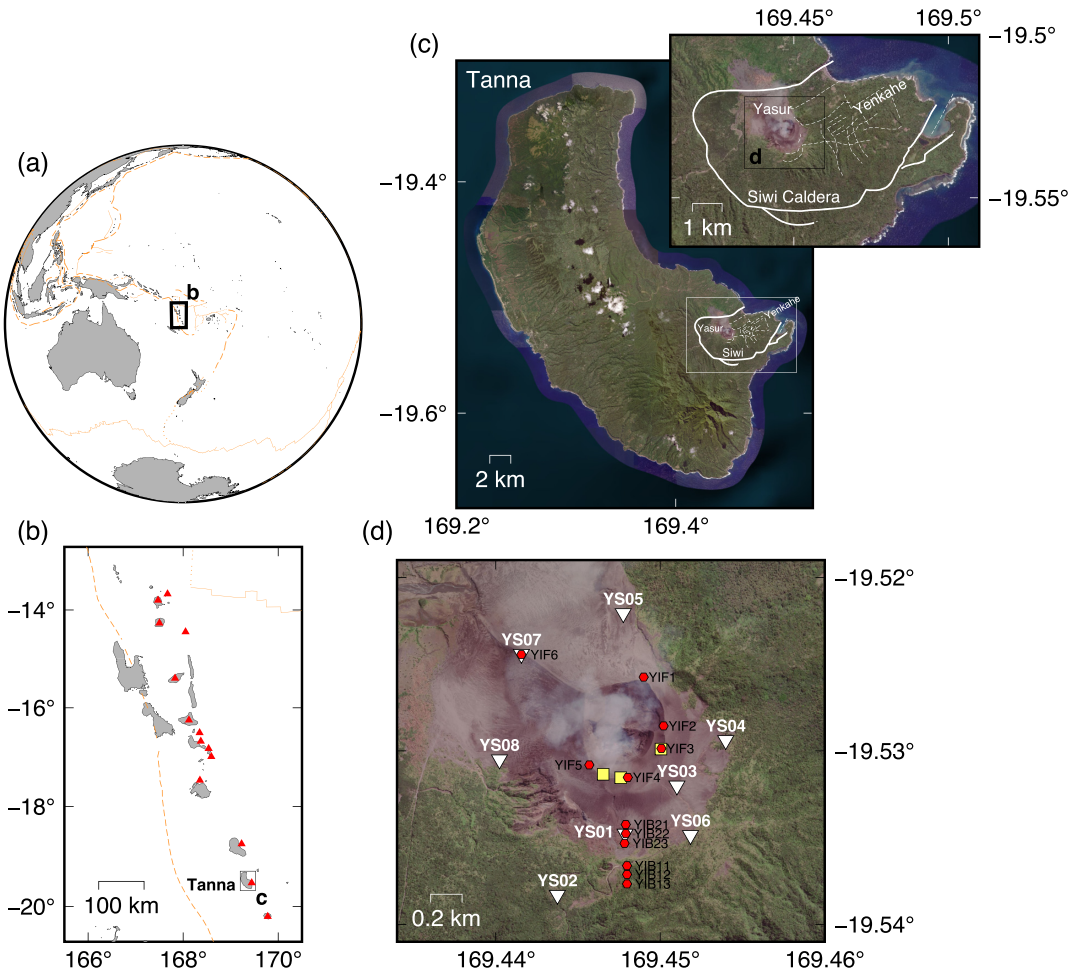

Figure 1. Location map. (a and b) Location of the Vanuatu archipelago in the southwest Pacific, with major plate boundaries (orange lines; Coffin *et al.* 1998) and potentially active Holocene (past 10 000 yr) volcanoes (red triangles) (Global Volcanism Program 2013). (c) Tanna Island, showing the locations of Yasur, Siwi caldera (thick white line), and the Yenkahe resurgent dome (primary faults and lineations indicated by white dashed lines; digitized from Carney & McFarlane 1979). (d) Yasur, showing temporary broad-band seismic and acoustic stations deployed in our field campaign 2016 July 27 to August 3. Inverted white triangles: three-component compact broad-band (120 s) seismometers (sampled at 200 Hz); red hexagons: broad-band infrasound sensors (sampled at 400 Hz); yellow squares: video cameras. Yasur summit is subdivided into North and South crater.

200 Hz on a three-channel Omnirecs (DiGOS) DATA-CUBE digitizer. The infrasound stations consisted of Chaparral Physics Model 60 UHP infrasound sensors with a flat response between 33 s to Nyquist and a pressure range of ±1000 Pa, sampled at 400 Hz on a DATA-CUBE digitizer. The two 3-element infrasound line arrays (YIB, Fig. 1) were identical in configuration to the single infrasound stations (YIF, Fig. 1), except with longer cables (75-m cables; sensor separations ∼55–65 m) and three-channel recording. The relatively high sample rate of 400 Hz used for the infrasound data permits capturing higher order features of acoustic explosion waveforms in the infrasound and low-audio ranges (Rowell *et al.* 2014; Matoza *et al.* 2019b) that is not captured with typical sample rates of permanent infrasound stations (e.g. IMS infrasound stations use a 20 Hz sample rate, with a 10 Hz Nyquist; Matoza *et al.* (2019a)).

The recording window (data availability) of our temporary seismo-acoustic network is shown in Supporting Information Fig. S1 (all times in this paper are reported in UT). Data were recorded between 2016 July 27 and August 3, with the network largely complete between 2016 July 28 and August 2. Data from station YS07 and YIF6 were not recoverable after 2016 July 31.

The video data collected during the field experiment are described by Fitzgerald *et al.* (2020) and utilized a DJI Phantom 3 'drone' (UAS) along with three GoPro Hero 3+ cameras with orthorectified lenses set up around the crater rim (Fig. 1). The GoPro cameras recorded for over 10 hr from 2016 July 30 to August 1. As described by Fitzgerald *et al.* (2020), the UAS was primarily utilized for field mapping volcanic ballistic projectile deposition; explosion observation was not the priority of this system during the field campaign. However, several pertinent UAS videos provide invaluable constraints on eruptive activity and infrasound signal interpretation (e.g. Supporting Information Movies M1–M3). All UAS video observations presented in this study represent a subset of the available UAS data that could be calibrated for timing using coincident GoPro camera and GPS synchronization.

3 SEISMO-ACOUSTIC OBSERVATIONS

3.1 Infrasound waveforms

The waveform data from our short field campaign contain a profusion of signals reflecting the rapidly occurring and persistent explosive activity of Yasur (Jolly *et al.* 2017; Matoza *et al.* 2017; Iezzi *et al.* 2019; Fee *et al.* 2021). The typical infrasonic signatures of Yasur's strombolian explosions (Fig. 2) consist of classic short-duration (∼5 s) explosion waveforms characterized by a sharp compressive onset, which in most cases is asymmetric with a higher amplitude initial compression than subsequent rarefaction. The explosion signals have wideband frequency content extending up to the 200 Hz Nyquist, which includes the low-audio subbass range (Goto *et al.* 2014; Matoza *et al.* 2019a). Numerous explosions and infrasound signals during the field campaign were associated with visible and audible shocks captured in video data and directly observed by field personnel (Austin *et al.* 2017; see Supporting Information Movies M1 and M2). Marchetti *et al.* (2013) previously noted the similarity between the waveform shape of Yasur infrasonic explosion signatures and blast waves from chemical explosions.

In addition to this dominant infrasonic signal type, we also record a variety of infrasonic pulses and tremor signals associated with sustained and pulsatory ash emissions, degassing, and spattering activity, validated through direct video observation (Fitzgerald *et al.* 2020). For example, visible on Fig. 2(c) is a near-continuous low-amplitude broad-band (∼0.1–20 Hz) infrasonic tremor, with a waveform appearance of near-continuous repetitive shocklets, that is directly related to sustained ash emissions from the North Crater as captured by a UAS video (see Supporting Information Movies M1 and M2). A detailed investigation of this infrasonic tremor mechanism is beyond the scope here, but we posit that this near-continuous highly cyclic repetitive shocklet signature reflects the low-level continuous jetting (short-lived sustained compressible gas jet flow with significant ash component) captured in the video footage, rather than a sequence of discrete individual bubble bursts. The repetitive shocklet waveform signature is similar to that associated with the 'crackle' phenomenon in man-made jets (Gee *et al.* 2007; Nichols *et al.* 2013), which has previously been identified in long-range volcanic infrasound signals associated with large explosive eruptions involving sustained jet flows (Fee *et al.* 2013; Matoza *et al.* 2018).

3.2 Seismic waveforms and seismo-acoustic source decoupling

The dominant seismic signals are numerous repetitive VLP signals with periods of ∼2–10 s (Figs 2 and 3), which extend into the long-period (LP) band (Battaglia *et al.* 2013, 2016; see also Section 3.4). We follow the definition of Chouet & Matoza (2013) for LP referring to periods from 0.2 to 2 s (frequencies 0.5 to 5 Hz) and VLP referring to periods from 2 to 100 s (frequencies 0.01 to 0.5 Hz); thus, the observed Yasur VLPs are at the shorter-period (higher-frequency) end of the VLP bandwidth. The VLP seismic events reoccur near-continuously throughout the data set with short-interevent times (∼20 to 60 s, but variable); hence, we use the appellation 'high-rate' to describe them. The explosion waveform example highlighted in Figs 2(c) and (d) shows a clear example of a sequence which begins with ∼4-s-period VLP seismic oscillations (observed across the network) at time ∼115 s in Figs 2(c) and (d); the main explosion occurs at ∼125 s and is characterized by a high-amplitude infrasonic explosion signal accompanied by a higher-frequency (>5 Hz to 100 Hz Nyquist) seismic signature of the explosion.

However, the majority of the data do not follow this simple behaviour and we observe strong variability in the synchronization of seismic and acoustic signals. Explosion events clearly delineated by infrasonic waveforms are underlain by seismic VLPs (seismic VLP and infrasound are 'synchronized'; Fig. 2). However, strong seismic VLPs also occur with only a weak infrasonic expression ('desynchronized'; Fig. 3). This behaviour is obvious in extended waveform plots (Figs 4 and 5; peak seismic amplitude waveform features visible at the scale of these figures is VLP). Fig. 4 spans three days and Fig. 5 spans one day around a transition on 31 July 2016 from weak to strong infrasound (corresponding to an increase in explosion size that is well-documented in video data and field observations by Fitzgerald *et al.* 2020), with only a modest corresponding increase in VLP seismic amplitudes. This transition from weak to strong infrasound with increase in eruption intensity also corresponds to a general shift from activity at North Crater to increased explosive activity at South Crater (Jolly *et al.* 2017; Fitzgerald *et al.* 2020); the violent explosion example highlighted in Figs 2(c) and (d) is one such explosion at South Crater (see Supporting Information Movies M1 and M2).

A consistent increase in infrasound amplitudes is recorded on 2016 July 31 across the YIF crater stations at different source–receiver azimuths (see Supporting Information), inconsistent with atmospheric propagation effects (i.e. wind direction; Matoza *et al.* 2009) and consistent with the increased explosive intensity (Jolly *et al.* 2017; Fitzgerald *et al.* 2020). Furthermore, the YIF crater stations are all within <0.5 km distance from the source, well below the range of ∼10–15 km where boundary layer propagation effects become significant for infrasound in the so-called diffraction zone (Fee & Garces 2007; Matoza *et al.* 2009). Vertical dashed lines in Fig. 5 indicate the times of the waveform examples highlighted in Figs 2 and 3, corresponding to VLP seismic events with (Fig. 2) and without (Fig. 3) accompanying infrasonic explosion signals. In Section 3.3, we quantify these variations using systematic event detection with swarm and multiplet analyses.

We note that air-to-ground coupling (ground-coupled airwaves) can occur in volcano seismo-acoustic data sets (e.g. Ichihara *et al.* 2012; Matoza & Fee 2014; Fee *et al.* 2016a; Matoza *et al.* 2019b). A comprehensive investigation of air-to-ground coupling for this data set is beyond the scope, but we confirmed that air-to-ground coupling does not affect any of the results presented here. The seismic VLP waveform inversion results (Section 4) are not affected by air-to-ground coupling (Section 4.3). A basic analysis of the higher-frequency (>5 Hz) seismic signature of selected Yasur explosions considering relative arrival timing and using methods of Ichihara *et al.* (2012), Matoza & Fee (2014) and Matoza *et al.* (2019b) (not shown here) also indicates that this higher-frequency seismic signature is dominantly a seismic phase (explosion earthquake); however, it remains possible that further work may identify minor contributions from air-to-ground coupling in the seismic waveforms. We also note that most waveforms displayed in the figures are unfiltered (see figure captions for details), such that acausal filter effects on waveform timing (Patrick *et al.* 2011) are not relevant.

3.3 Seismo-acoustic signal evolution and multiplet analysis

3.3.1 STA/LTA

The high event rate presents a challenge to standard automated signal detection procedures. For a preliminary characterization of

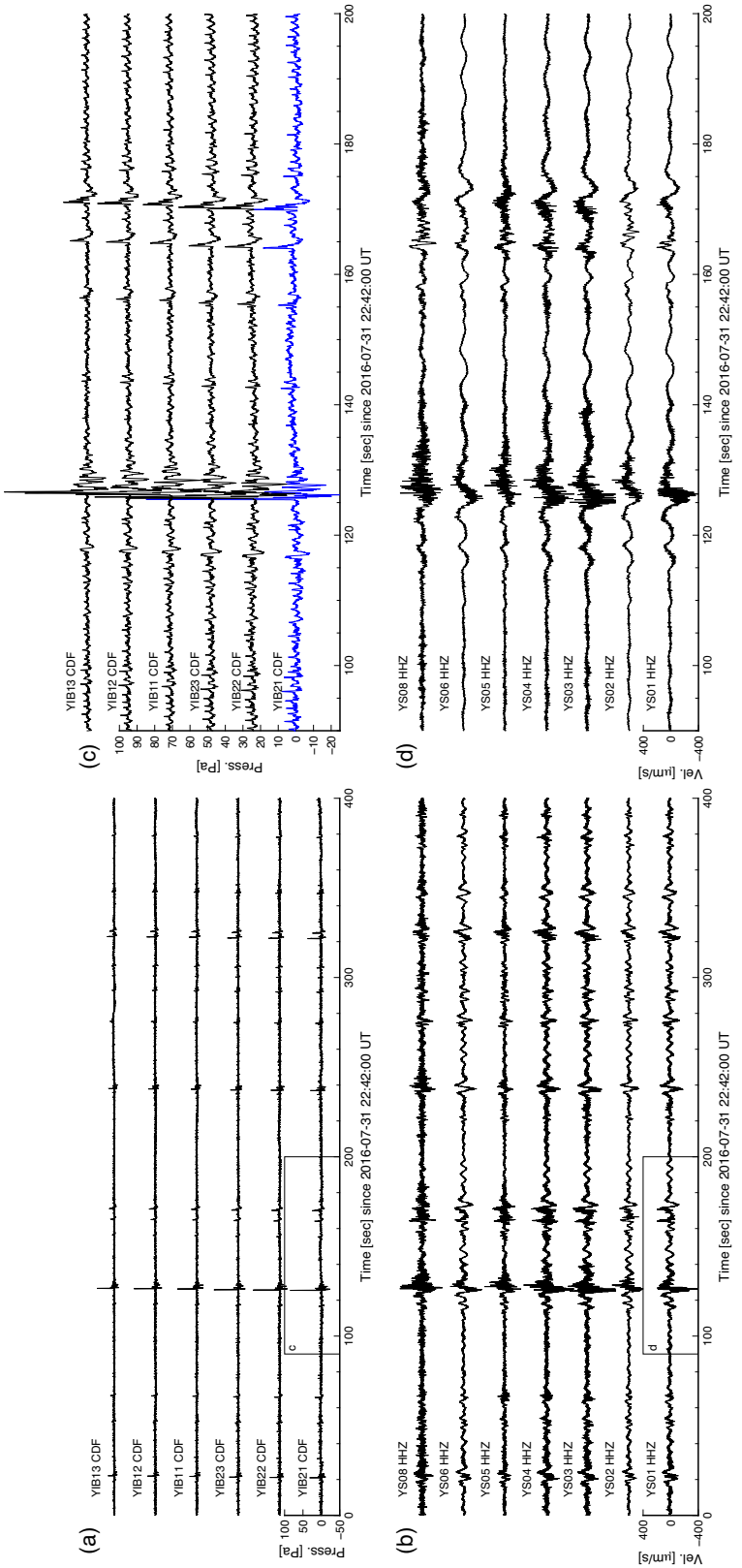

Figure 2. Seismo-acoustic (vertical component velocity and infrasonic pressure) waveform signatures of powerful explosion events at Yasur, including a large ballistic eruption. All data shown are raw, unfiltered waveforms. The same amplitude scale is used for all waveforms on each subfigure (lower-left scale). The left label above each trace indicates the station and channel (see Fig. 1); waveform offsets are arbitrary to display coincident data. (a) Infrasound and (b) vertical-component seismic velocity for a 400 s sequence starting at 22:42:00, 31 July 2016 UT; boxes indicate time-range of zoomed data in (c) and (d). Blue colour in (c) helps with visual separation of the high-amplitude rapid-onset of the waveform which overlaps adjacent traces at this scale. See also Supporting Information Movies M1 and M2.

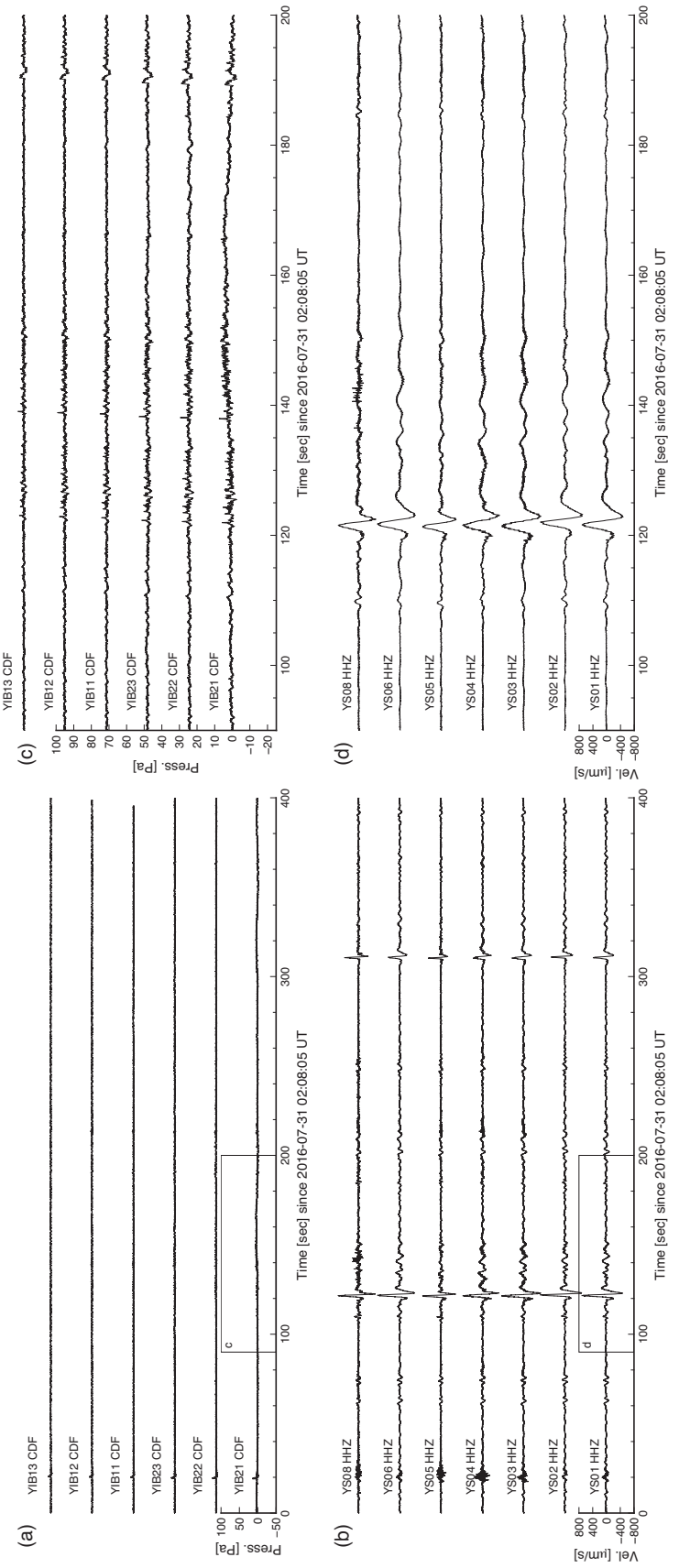

Figure 3. As for Fig. 2, but for a VLP seismic event sequence with weak-to-little accompanying infrasound and not related to immediate surficial explosive activity (plot origin time 02:08:05, 31 July 2016 UT). This event sequence is more typical of the majority of VLP seismic events in the data, which are poorly correlated with surficial explosions and infrasound (see Figs 4–6). Note that the seismic amplitude scale is twice that used in Fig. 2, while the infrasound amplitude scale is the same as that used in Fig. 2.

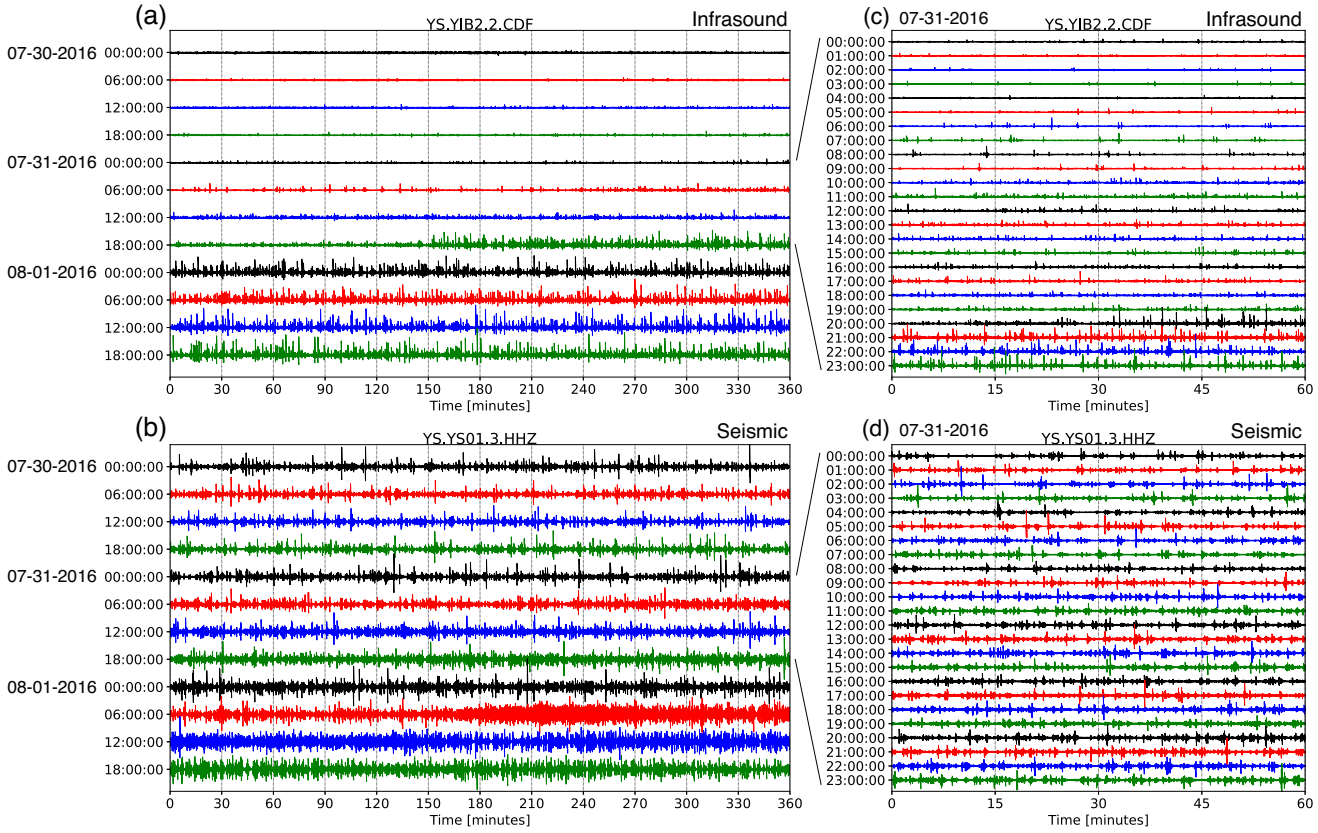

Figure 4. Unfiltered waveforms (helicorder plots) at collocated (a, c) infrasound station YIB22 (channel CDF) and (b, d) broad-band seismometer YS01 (vertical component, HHZ), located approximately 630 m from the summit vents; all times in UT. (a, b) 3 full days from 00:00 30 July to 00:00 2 August 2016; (c, d) day of 31 July 2016. The most prominent individual seismic events visible at this scale are ∼10-s-period VLP seismic events, while the visible infrasound events are classic explosion waveforms (see Figs 2 and 3). Note the dramatic increase in infrasound explosion event amplitudes, with only a modest corresponding increase in VLP seismic amplitudes. The infrasound helicorder plots are qualitatively similar across the YIF crater stations (see Supporting Information Fig. S2), inconsistent with atmospheric propagation effects.

the data set, we attempt network-coincident STA/LTA (short-term average/long-term average) detection (Withers *et al.* 1998; Figs 6a and b). For seismic data, we define triggers with 0.5–8 Hz filtered data using an STA length of 0.5 s, an LTA length of 5 s, and a coincident STA/LTA threshold of 3 on at least four stations of the full network (note that this choice of filter distorts the VLP seismic waveforms, but makes them more detectable with STA/LTA). For infrasound data, we define triggers with 0.1–50 Hz filtered data using an STA length of 0.5 s, an LTA length of 40 s, and a coincident STA/LTA threshold of 3 on at least 2 channels of the 3-element array (YIB21, YIB22, YIB23, Fig. 1). Figs 6(a) and (b) show peak event amplitudes at a reference station in a time-window from −5 to +10 s around the network-coincident STA/LTA trigger. Due to the high event rates and lack of pause between events, this STA/LTA configuration misses many events, but this procedure results in 25 279 infrasonic and 10 735 seismic events (Figs 6a and b). The STA/LTA approach, however, is generally not well-suited for VLP waveforms (see Section 3.3.3).

3.3.2 RSAM and RIAM

A complementary rapid metric for the continuous waveform amplitude variation is provided by 10-min 'real-time' seismic amplitude measurement (RSAM) values (Endo & Murray 1991) and (we define here also) 'real-time' infrasonic amplitude measurement (RIAM) calculated as the 10-min mean of absolute amplitude of 0.1–50 Hz filtered waveforms, plotted at the centre of the time window (Figs 6c–e). We also compare this broad-band (0.1–50 Hz) RSAM with a short-period (1–50 Hz) RSAM in Fig. 6(d), as the short-period RSAM is more similar to the typical monitoring setup with the permanent short-period seismometer at Yasur. RSAM and RIAM (Figs 6c–e) provide useful rapid signal summaries that track the transition to more energetic explosive behaviour on 2016 July 31 (Day 4 in Fig. 6), as documented by Fitzgerald *et al.* (2020). The consistency of the RSAM variations at all seismic stations across the network provides information on source variation that is robust to individual station noise levels and path effects. The consistent RIAM time-series are again incompatible with atmospheric propagation effects (i.e. wind direction) and track the clear waveform amplitude variations shown in Figs 2–5. The short-period RSAM (Fig. 6d) better tracks RIAM than the broad-band RSAM, further highlighting the decoupling of the VLP component from the higher frequency component (>1 Hz), which more closely tracks surficial explosions and infrasound.

3.3.3 Multiplet analysis

We perform multiplet analysis (e.g. Stephens & Chouet 2001; Green & Neuberg 2006; Petersen 2007; Matoza & Chouet 2010; Rodgers *et al.* 2015) to determine the dominant VLP waveform signatures in

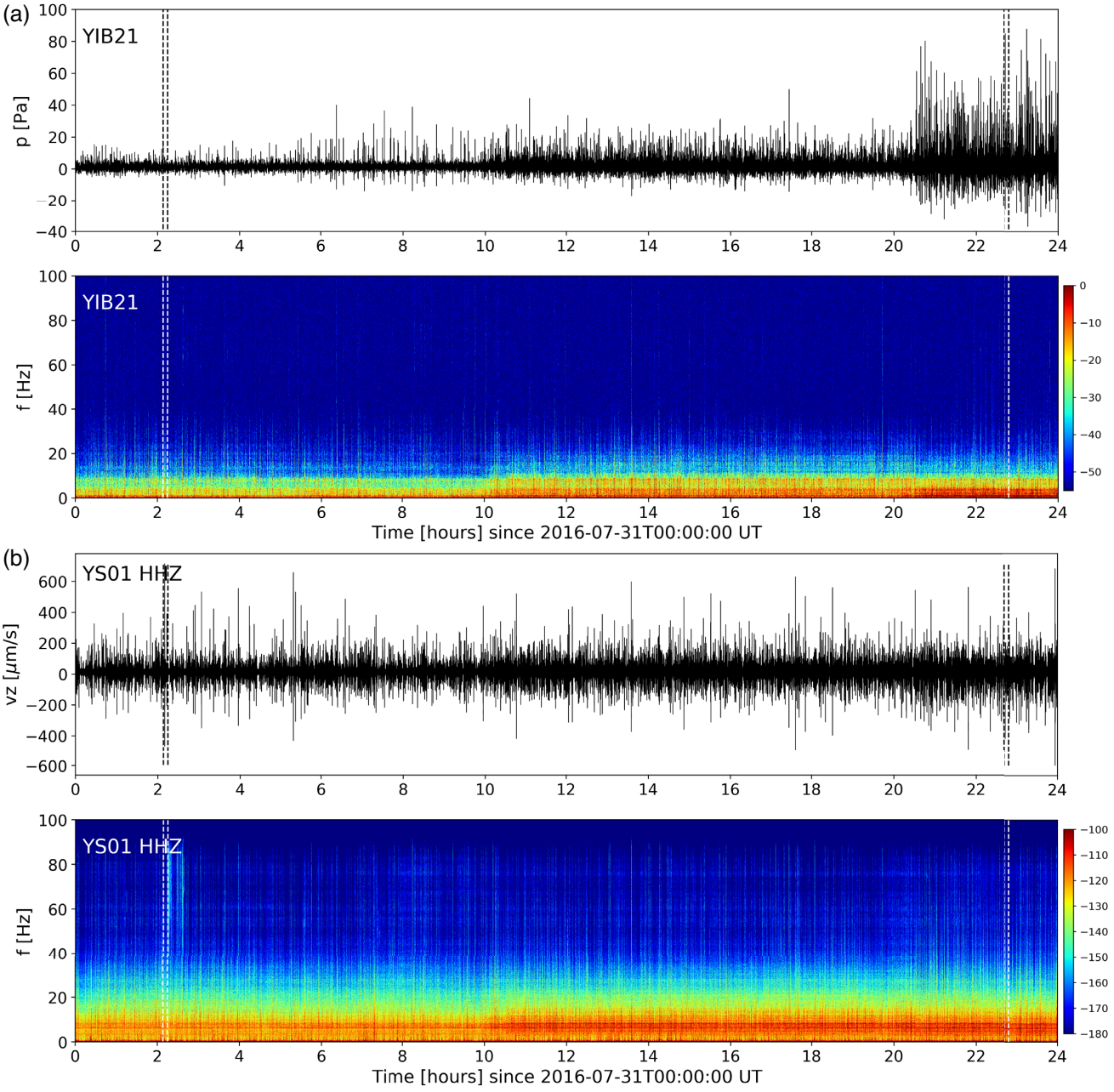

Figure 5. Waveforms (unfiltered) and spectrograms for the day of 31 July 2016 UT at (a) infrasound station YIB21, (b) vertical-component velocity at seismic station YS01. The vertical dashed lines indicate the 400 s time windows of Figs 2 and 3. The spectrogram colour scale units are $10\log_{10}(P)$, where P is the power spectral density in (a) [Pa^2/Hz] and (b) [$(m\ s^{-1})^2$/Hz].

the data set. Our method largely follows that of Matoza & Chouet (2010), but here uses a new parallel implementation in Python for rapid computation. As a starting catalogue, the STA/LTA results (Section 3.3.1) are unsuitable due to inconsistent waveform autopicks. However, the simple VLP pulse shape (see, e.g. Figs 3b and d) motivates the use of a simple event detection scheme using a standard peak detection algorithm to identify peaks in the waveform above an amplitude threshold and with a prescribed minimum time spacing (Duarte & Watanabe 2018). Peak detection performs well for this data set, consistently picking the VLP signal maximum and allowing sharp waveform alignment, as well as producing a detection list that is in general agreement with the independent STA/LTA detections but with more consistent picks (Fig. 7). We use the high-amplitude peak detections (blue dots, Fig. 7a; 7833 events) as input to the multiplet procedure.

For the 7833 events, we window the waveform data at station YS01 (vertical component, HHZ) from −10 to +20 s around the picked peak amplitude. We then cross-correlate each event with every other event, storing the results in a cross-correlation matrix. We group the events into multiplets using a threshold correlation-coefficient $r \geq 0.75$, following the method of Green & Neuberg (2006) and Matoza & Chouet (2010). The amplitudes and timing of the nine most populous multiplets (all each comprising at least 100 events) are shown in Figs 7(b) and (c), but we limit all subsequent analysis to quantifying the dominant and most populous VLP multiplet. There are only minor waveform differences between the two

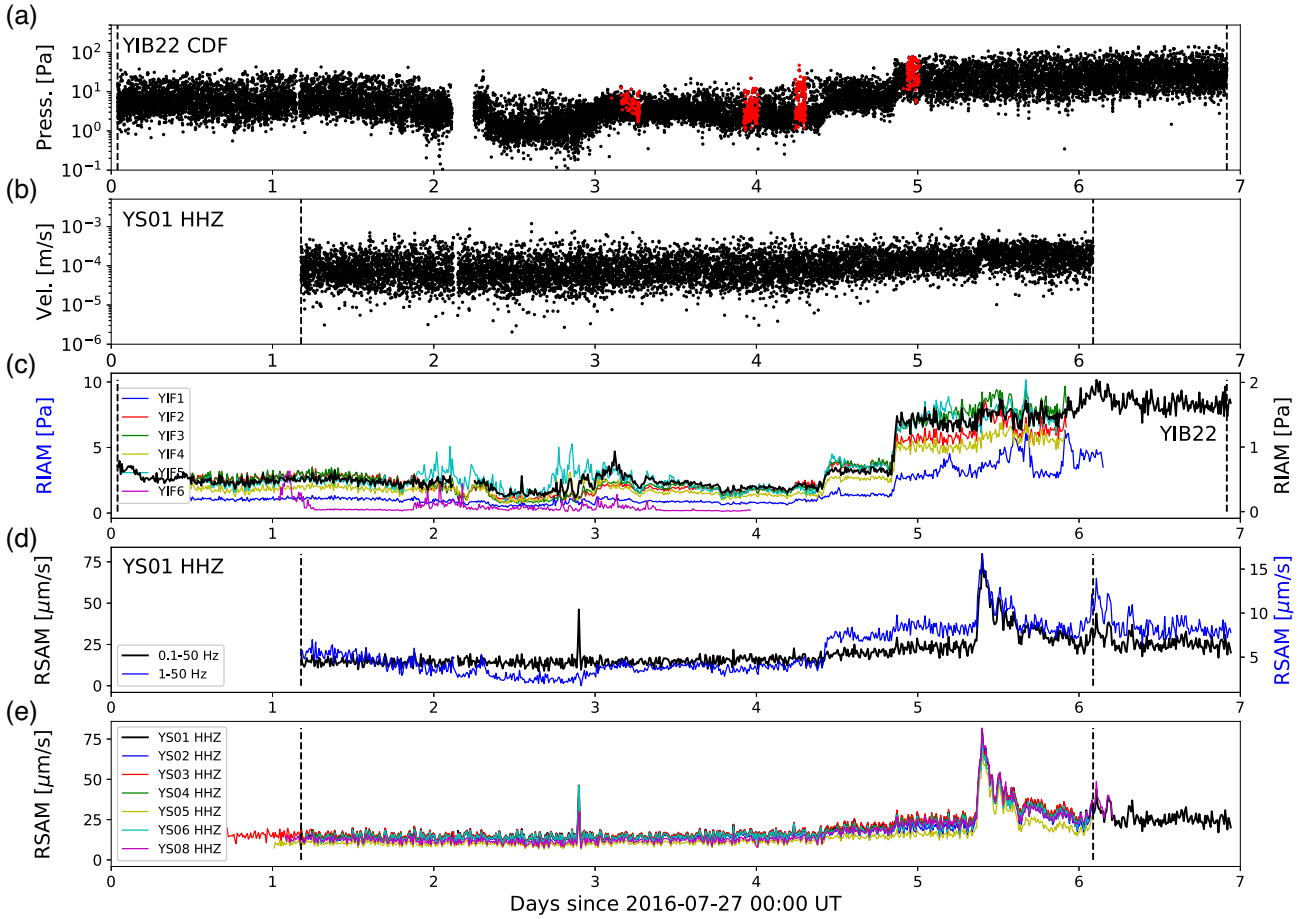

Figure 6. Infrasound and seismic amplitude metrics (see Fig. 1 for station locations). (a, b) Peak event amplitudes at collocated infrasound station YIB22 (channel CDF) and broad-band seismometer YS01 (vertical component, HHZ), located approximately 630 m from the summit vents. Events are defined on this figure using a network-based STA/LTA method; vertical dashed lines in all panels represent times of network completion for coincident triggers. Red events in (a) are explosions with video constraints (Fitzgerald *et al.* 2020). (c, d, e) 10-min 'real-time' infrasonic amplitude measurement (RIAM) and real-time seismic amplitude measurement (RSAM) values calculated as the 10-min mean of absolute amplitude of 0.1–50 Hz filtered waveforms, plotted at the centre of the time window (Endo & Murray 1991). (c) RIAM at YIB22 (black line, right y-scale) and RIAM across the YIF crater stations (colour lines, legend, left y-scale). (d) RSAM for 0.1–50 Hz (black, left y-scale) and 1–50 Hz (blue, right y-scale) filtered data at YS01-HHZ. (e) RSAM (0.1–50 Hz) for vertical components across the seismic network. Note the consistent RSAM (e) and RIAM (c) variations across the network. An increase of infrasound STA/LTA event amplitudes (a) and RIAM (c) on day 4 (2016 July 31) correlates to a visually observed increase in explosion intensity (Fitzgerald *et al.* 2020). The increase in RIAM across the network (c), for stations at different azimuths from the source, is inconsistent with atmospheric (wind) propagation effects.

most populous multiplets (multiplet #1: 932 events and multiplet #2: 922 events), indicating that the threshold correlation-coefficient $r \geq 0.75$ is conservative and that these are essentially the same waveform signature (see Supporting Information Fig. S3). Illustrating this, the waveform stacks of multiplets #1 and #2 are correlated with each other with $r = 0.91$. Thus, the majority of high signal-to-noise ratio VLP events in the data set (i.e. here multiplets #1, #2) result from a similar highly repetitive mechanism, further justifying our focus on the main and dominant VLP signature.

We emphasize that the starting catalogue of 7833 events used here is based on a simple peak detection method, and that most of the remaining multiplets have low populations. For example, Fig. 7(c) shows the temporal evolution of the top nine ranked (by population) multiplets consisting of at least 100 events each (see also Supporting Information Fig. S3). However, multiplets from #3 to #9 (inclusive) have a combined total population of only 1192 events. Additionally, 2416 of the starting 7833 events are not assigned to any multiplet using the threshold correlation-coefficient $r \geq 0.75$, largely reflecting low signal-to-noise ratios of these unassigned events. Here our focus is on quantifying the main and dominant VLP signature (i.e. represented here by multiplets #1 and #2). Considering the less populous multiplets is beyond the scope of the present work, but these other minor multiplets may hold important additional information (Section 5.5). Also beyond the scope of the present work, lowering the correlation-coefficient threshold would assign a greater quantity of (noisier) events to multiplet groupings, which could lead to a more comprehensive characterization.

3.3.4 Template matching and stacking for the dominant VLP multiplet

Finally, we employ template matching and (linear) stacking (Matoza *et al.* 2015) to extract events belonging to the dominant VLP multiplet and form clean stacks for full-waveform inversion (Figs 7d–g).

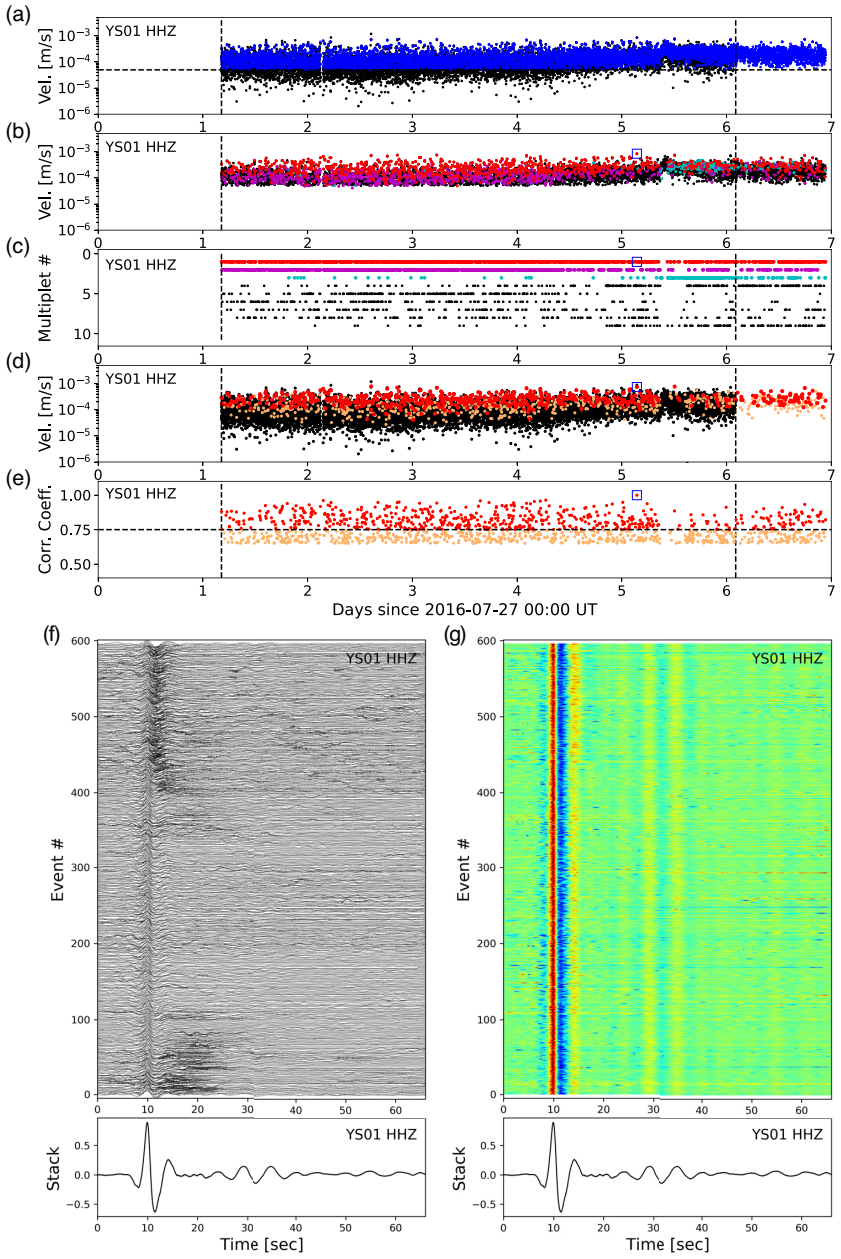

Figure 7. Event detection, multiplet analysis, template matching, and stacking to extract the dominant VLP multiplet for the full data set (see text for method details). All data analysis illustrated here is for station YS01 vertical velocity (HHZ); the vertical dashed lines in (a)–(e) represent times of network completion for coincident STA/LTA triggers as in Fig. 6. (a) Black dots: STA/LTA detections; detections are network-based and the amplitude value is for YS01-HHZ (10 735 events). Blue dots: results of a separate single-station peak-detection algorithm applied only to YS01-HHZ (7833 events). The peak detection requires a minimum amplitude threshold of 5×10^{-5} m s^{-1} (horizontal dashed line) and a minimum time spacing of 30 s between events. The event sequence from peak detection is used as input to the multiplet analysis (b, c). (b, c) Results of multiplet analysis applied to the event catalogue defined by peak detection. (b) Black dots: all events used in multiplet analysis (i.e. the 7833 events shown as blue dots in a); red, magenta, and cyan: multiplets #1, #2 and #3, respectively, which are the three most populous multiplets (multiplet #1: 932 events, multiplet #2: 922 events, multiplet #3: 273 events). Note that the black dots in (b) include 2416 events that did not assign to any multiplet given the threshold criteria. (c) Multiplet number versus time, only showing the top 9 ranked multiplets consisting of at least 100 events each. The colour-scheme matches that shown in (b): red, magenta, and cyan: multiplets #1, #2 and #3, respectively; black: multiplets #4 to #9. The largest-amplitude event from the dominant multiplet #1 (blue square in b–e; an event at 03:27:16.38, 1 August 2016 UT) is then used as a seed in a separate template matching procedure (d–g). (d, e) Template matching results. Red: template-matched detections (597 events) with correlation coefficient $r \geq 0.75$ with the seed event (blue square); orange: additional below-threshold template-matched detections (667 events) with $0.65 \leq r < 0.75$. Black dots in (d) are the network-based STA/LTA detections (same as a) for reference. Horizontal dashed line in (e) shows the threshold r of 0.75. (f, g) Waveforms (unfiltered) of the final 597 events defined by template matching with $r \geq 0.75$, together with their normalized mean (linear) stack. Event # ascends chronologically. (g) Each row of the matrix is the waveform of a different event, with red indicating positive amplitude and blue indicating negative amplitude. Note the consistent oscillatory VLP waveform features in the coda visible until >60 s, which are robust features of the waveform stack. Also note the variability in additional high-frequency component between ∼10–30 s in the multiplet waveform sequence. This stacking procedure is repeated for all stations and channels to produce robust stacks for waveform inversion.

We use the largest-amplitude event belonging to the dominant multiplet (blue square in Figs 7b–e; an event at 03:27:16.38, 1 August 2016 UT) as a 66 s duration seed event in the template matching procedure, which is applied to the continuous waveform data from the full experiment using YS01, HHZ, decimated to a 50 Hz sampling frequency and filtered 0.01–10 Hz. We note that this chosen seed event is also the largest-amplitude VLP event in the entire data set. We identify 597 high signal-to-noise (SNR) ratio events with $r \geq 0.75$ with the template (with a minimum 30 s between events), which we stack and scale by the seed for use in the waveform inversion procedure, following Matoza *et al.* (2015) (Figs 7f and g). This stacking procedure is repeated for all stations and channels to produce robust stacks for waveform inversion. We note that this template-matching produces fewer detections than the previous multiplet approach (Section 3.3.3) because of the longer 66 s template waveform window. However, this workflow produces a robust stack of high SNR events from the dominant multiplet (Figs 7d and e), with individual events having a consistent oscillatory VLP waveform coda visible for >60 s, which is a robust feature of the waveform stacks (Figs 7f and g).

We emphasize that the template matching presented in this section is an entirely separate procedure beginning again from the continuous waveform data. It does not rely on the multiplet groupings identified in the prior Section 3.3.3, other than for identifying the initial seed template event (the seed template event is defined as the highest amplitude event in the most populous multiplet #1 found in the method of Section 3.3.3).

In Supporting Information Fig. S4, we show the results of lowering the threshold correlation coefficient used in the template matching procedure to $r \geq 0.65$, resulting in 1264 template detections compared to the 597 template detections with $r \geq 0.75$. The waveforms shown in Supporting Information Fig. S4 are barely distinguishable from those in Figs 7(f) and (g), showing that more individual VLP events with the dominant waveform signature are pulled into the procedure when lowering the threshold correlation coefficient. Since our emphasis is on producing high SNR robust stacks for waveform inversion, we use the conservative threshold of $r \geq 0.75$ for the main workflow presented. We emphasize that these 597 detections represent the highest SNR selection of events from within the main and dominant VLP signature and thus are representative of the dominant majority of (high signal-to-noise ratio) VLP events in the data set.

3.4 VLP spectral signature

The frequency content of the dominant VLP seismicity is shown in Fig. 8. We first show (Fig. 8a) the 24-hr power-spectral density (PSD) estimates (daily average using Welch's method with 10.92-min, 50 per cent overlapping time windows) for the day of 2016 July 31 for all vertical components across the network. This is then compared with (Fig. 8b) an average stack of PSD estimates for the individual transient VLP events (PSD periodogram estimates from event-windowed data of length 66 s) in the dominant multiplet (i.e. all waveforms shown in Figs 7(f) and (g), but for all stations of the network). In both cases (Figs 8a and b), three pronounced and sharp spectral peaks are present at 0.11 Hz, 0.15 Hz, and 0.2 Hz, confirming that these dominant spectral peaks in the continuous waveform data are the spectral signature of the individual repetitive VLP events and are not an artefact arising from the Dirac-comb effect (e.g. Powell & Neuberg 2003; Hotovec *et al.* 2013). The sharp VLP spectral peaks are temporally stable (Fig. 8d). This spectral signature being present in the individual event-windowed VLP seismic events (Fig. 8b) also indicates that it does not arise from a background continuous VLP tremor; however, given the highly repetitive and high-rate nature of the individual VLP events, the distinction between high-rate individual VLP events and a continuous VLP tremor (which may represent, e.g. continuous conduit mode oscillations; Liang *et al.* 2020) starts to become unclear. Additionally, the consistent spectral peaks across the network (Fig. 8) are inconsistent with path or site effects (Goldstein & Chouet 1994). The VLP signal is partially in the microseismic frequency band (e.g. McNamara *et al.* 2009), but the distinct sharp spectral peaks deviate significantly from a broader microseismic signature (Figs 8c and d).

3.5 Variable seismo-acoustic synchronization and additional video constraints

The multiplet and template matching analyses (Sections 3.3.3 and 3.3.4) systematically confirm the observations of seismo-acoustic source decoupling (variable seismo-acoustic signal synchronization) described in Section 3.2. For example, Fig. 9 shows three seismic VLP events belonging to the dominant VLP multiplet as defined through template matching (Section 3.3.4). Fig. 9(a) shows the initial seed event used for template matching, while Figs 9(b) and (c) show two other events whose 66 s seismic waveforms correlate with the seed event with r of 0.96 and 0.85, respectively. The same seismic VLP multiplet waveform occurs with and without a surface explosion inferred from infrasound.

The low-amplitude infrasonic tremor signal associated with the VLP seismic event in Fig. 9(b) is related to gas-rich spattering and vent 'flaming' activity (see Supporting Information Movie M3). In contrast, the VLP seismic event shown in Fig. 9(c) is accompanied by a powerful infrasonic explosion signal, which also produces additional higher frequency components in the seismic waveform. We do not have a UAS video of this particular event (event in Fig. 9c), but the GoPro video observations (Supporting Information Movie M4) confirm a moderate ballistic eruption at this time (Fitzgerald *et al.* 2020). Numerous GoPro and UAS videos captured at other times in the data set with higher visibility confirm unequivocally the association between such large amplitude infrasonic explosion signals and violent explosions and in some cases visible shocks (see, e.g. Supporting Information Movies M1 and M2).

The VLP seismic event previously shown in Fig. 3 also belongs to the dominant VLP multiplet, correlating with the seed event with r of 0.94. However, the example VLP seismic event accompanied by a powerful infrasound explosion event highlighted in Fig. 2 (and Supporting Information Movies M1 and M2) does not belong to the dominant seismic VLP multiplet and likely corresponds to a shallow magma oscillation and explosion source signature (see Section 5.5).

3.6 Systematic progression in VLP seismic decoupling and reconnection with surficial explosions and infrasound

3.6.1 Waveform variations

A systematic analysis of the seismo-acoustic variability and association between the dominant seismic VLP waveforms and corresponding infrasound (or lack of) is presented in Figs 10 and 11. Fig. 10 shows the seismic VLP waveforms at YS01 (same as Fig. 7f) compared to the corresponding waveforms at infrasound stations

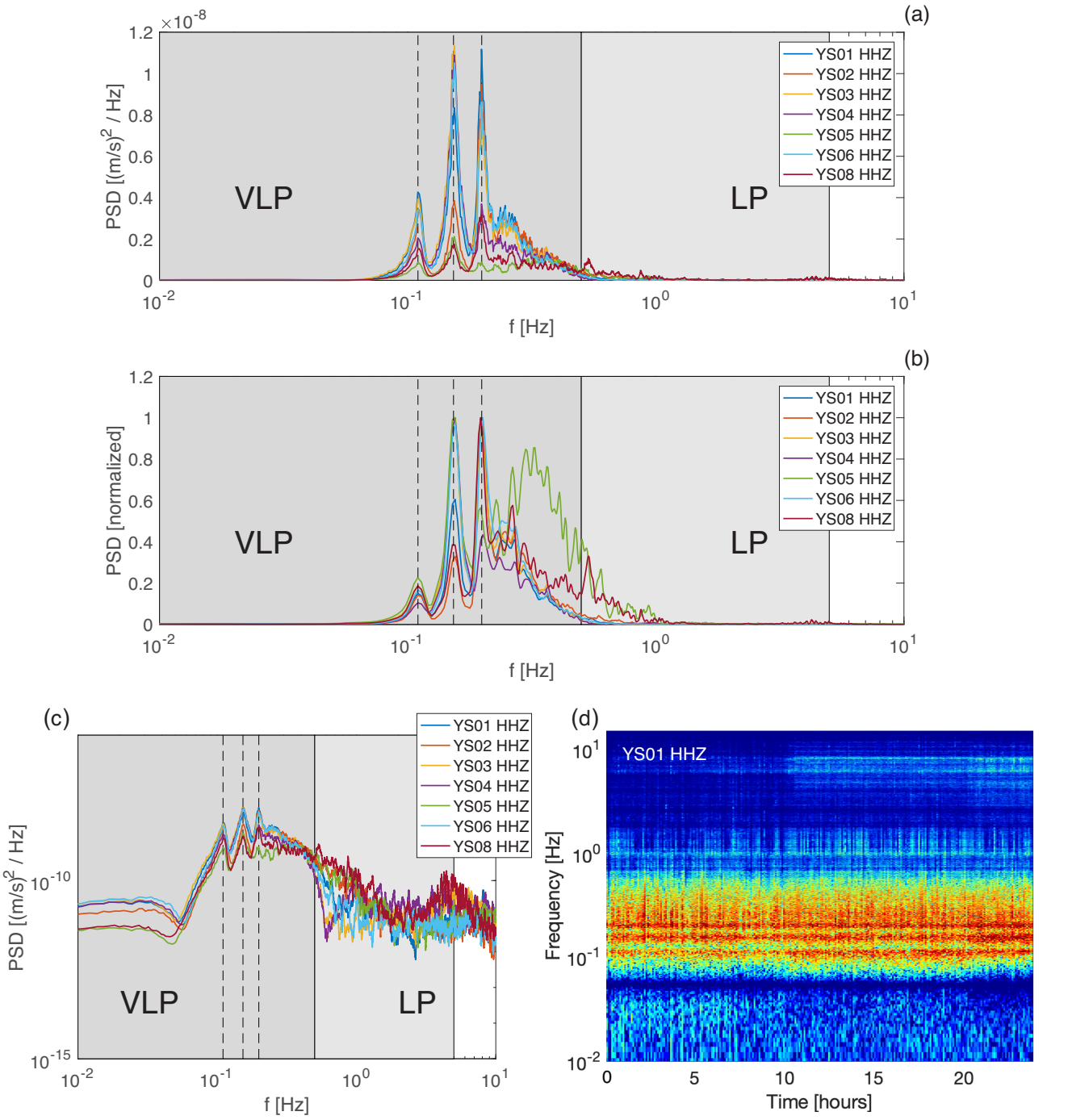

Figure 8. Power spectral density (PSD) of vertical seismic velocity waveforms across the network comparing (a) daily average PSDs from continuous waveform data with (b) stacked short-time duration PSDs estimated from the individual event-windowed waveform data for the dominant VLP multiplet (e.g. Figs 7f and g). (a) one-day PSDs of continuous waveform data computed using Welch's method with 10.92-min sections (2^{17} samples at 200 Hz sampling frequency) that are 50 per cent overlapping (262 sections for the 24-hr) for the day of 2016 July 31; colours and legend indicate the different stations (all vertical component). (b) PSDs of the dominant VLP multiplet computed by averaging PSDs from the 597 individual events in the dominant VLP multiplet (spanning entire data set) using 66 s duration event-windowed waveform data (e.g. see Figs 7f and g), and utilizing a simple periodogram estimate with waveform zero-padding to increase spectral resolution. Three sharp spectral peaks are prominent in both (a) and (b) at 0.11, 0.15 and 0.2 Hz (vertical dashed lines) at all stations, demonstrating the dominance of this VLP spectral signature in the data set. The VLP (0.01 to 0.5 Hz) and LP (0.5 to 5 Hz) band definitions are indicated by shading for reference. (c) Same as (a) (one-day PSDs of continuous waveform data), but with PSD displayed in log-scale. (d) Spectrogram plot for YS01 HHZ showing the temporal evolution of the PSD windows used in (a); i.e. 10.92-min sections (2^{17} samples at 200 Hz sampling frequency) that are 50 per cent overlapping (262 sections for the 24-hr) for the day of 2016 July 31. At station YS05, normalization (Fig. 8b) scales-up the power >0.25 Hz, reflecting the slightly lower signal amplitudes of the 3 main VLP peaks at this station location.

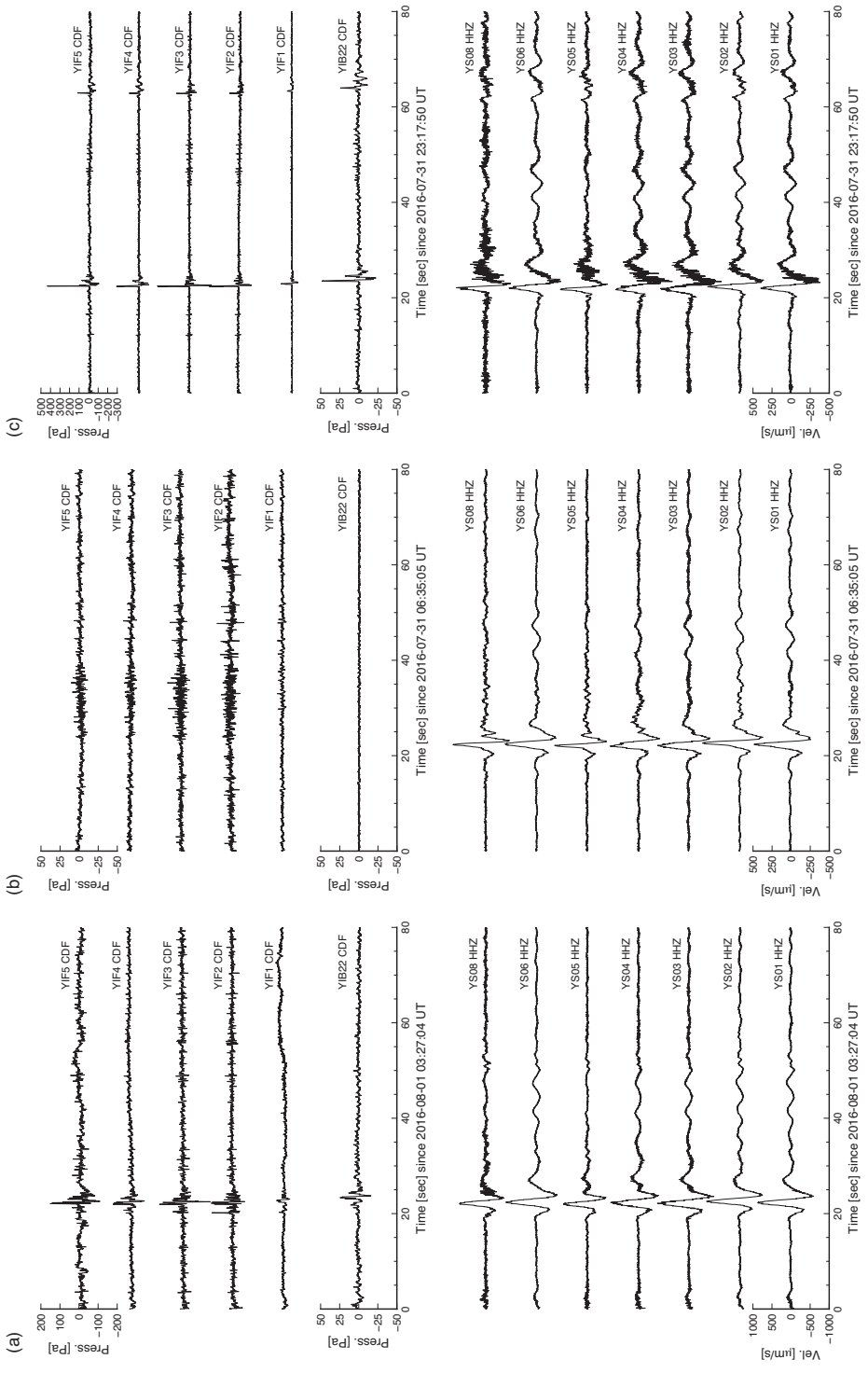

Figure 9. Seismo-acoustic (vertical component velocity and infrasonic pressure) waveforms (all traces unfiltered) at selected stations for three selected events belonging to the dominant seismic VLP multiplet as defined by template matching: (a) the high-amplitude seed event (event used for template matching) for the dominant seismic VLP multiplet (plot origin 03:27:04, 1 August 2016 UT); (b) a VLP seismic event in the multiplet with weak infrasound (plot origin 06:35:05, 31 July 2016 UT); and (c) a VLP seismic event in the multiplet with powerful infrasound (plot origin 23:17:50, 31 July 2016 UT). In each seismic panel, all traces within the panel are displayed at the same scale (lower left scale), but the scale for (a) is twice that of (b) and (c). For the infrasound data, the upper left scale in each case is the same for all traces from YIF stations and adjusted between events, but the infrasound data from station YIB22 have their own amplitude scale axis and are displayed at the same scale across all three events (a, b, c) for comparison. Note the strong variability in infrasound signature for the same seismic VLP multiplet. Using a 66 s duration window for template matching (see Section 3.3.4), the VLP seismic events shown correlate with the seed event (a) with a correlation coefficient of (b) 0.96 and (c) 0.85. The event shown in (c) has a clear powerful infrasonic explosion signature, which also produces additional higher frequency components in the seismic record. The low-amplitude infrasound signal shown in (b) is associated with gas-rich energetic spattering activity, as demonstrated clearly by Supporting Information Movie M3.

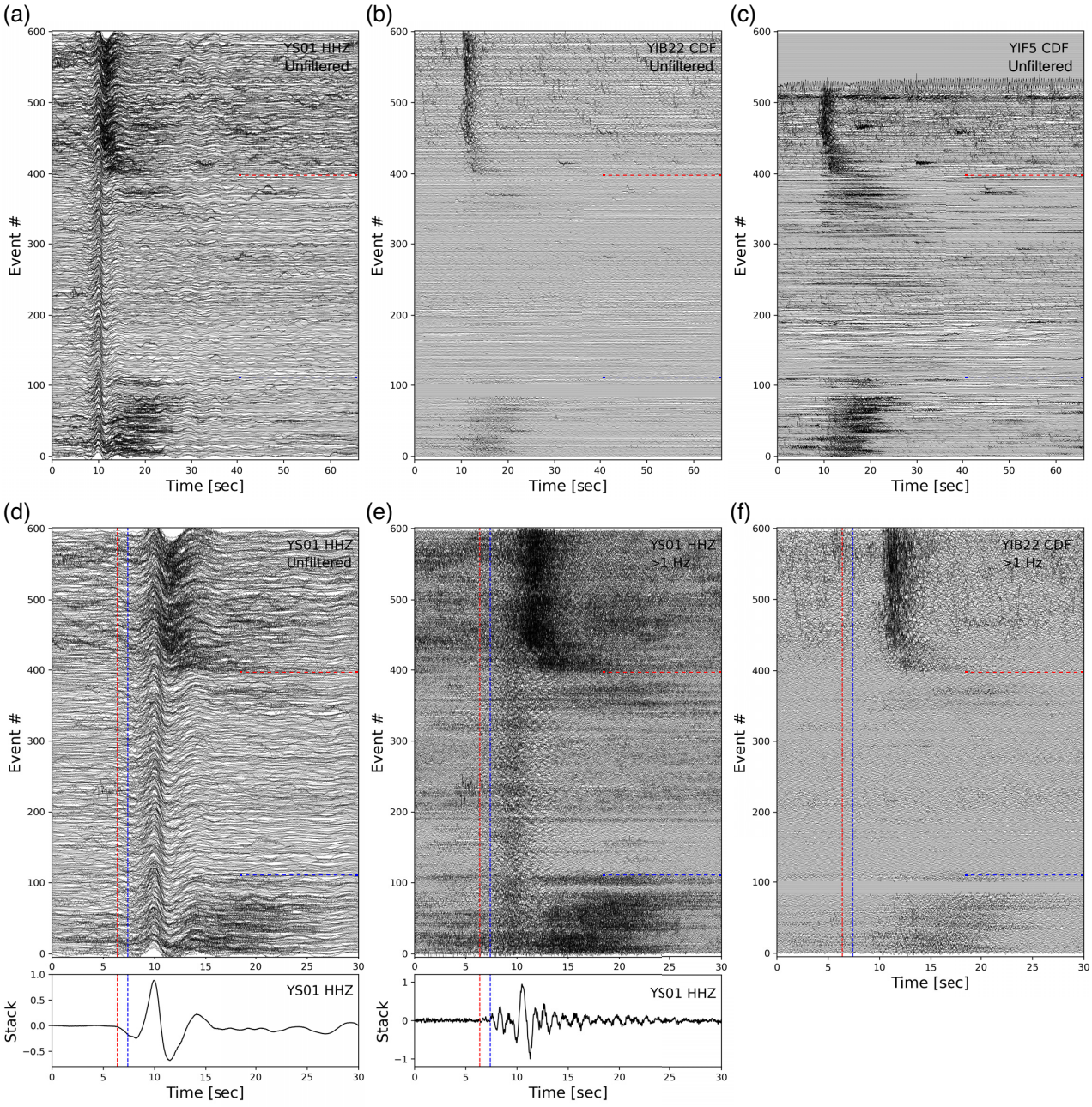

Figure 10. (a) Seismic waveforms (unfiltered) for the dominant VLP multiplet at YS01-HHZ (same as Fig. 7f) compared to the corresponding infrasound waveforms (unfiltered) windowed at the same absolute times for infrasound stations (b) YIB22 and (c) YIF5. In each panel, waveforms are displayed with a correct relative amplitude scale (traces are not normalized; they have been scaled by a common linear factor to allow relative amplitude comparison between events). Event # ascends chronologically. Events ∼100 to 400 have little to no infrasound. Event numbers >400 have clear infrasound and a corresponding high-frequency seismic arrival associated with a surficial explosion. Event numbers <100 have longer duration and lower-amplitude infrasound and high-frequency seismic component. Compare with Fig. 11, which shows amplitude and timing metrics extracted from these waveforms. Horizontal dashed lines on all panels (a–f) represent time markers of (blue) 07:40:49, 29 July 2016 and (red) 09:54:10, 31 July 2016 UT for comparison with Fig. 11. (d), (e), and (f) show a zoom on the first 30 s of the waveforms shown in (a) and (b) to better show arrival time details. (d) Unfiltered YS01-HHZ seismic data; (e) YS01-HHZ seismic data filtered with a high-pass >1 Hz; (f) YIB22 infrasound data filtered with a high-pass >1 Hz. A linear stack is shown for the seismic waveforms in (d) and (e). In (d), (e), and (f), the vertical red dashed line corresponds to the onset time of the VLP downward first motion picked from the stack (6.38 s relative to the start time of the template window); the vertical blue dashed line corresponds to the onset (7.4 s relative to the start time of the template window) of a consistent LP event recorded for all events in this VLP-based multiplet.

YIB22 and YIF5, windowed around the template detection times of the dominant seismic VLP multiplet (597 events). For all waveforms shown in Fig. 10, the trigger times are based on the seismic VLP template matching (Section 3.3.4) and the reference time t=0 is the start of the seismic template. Fig. 11 summarizes amplitude and timing metrics extracted from these waveforms.

Figs 10 and 11 show that the variable synchronization and decoupling of seismic VLP and infrasound is not random and instead

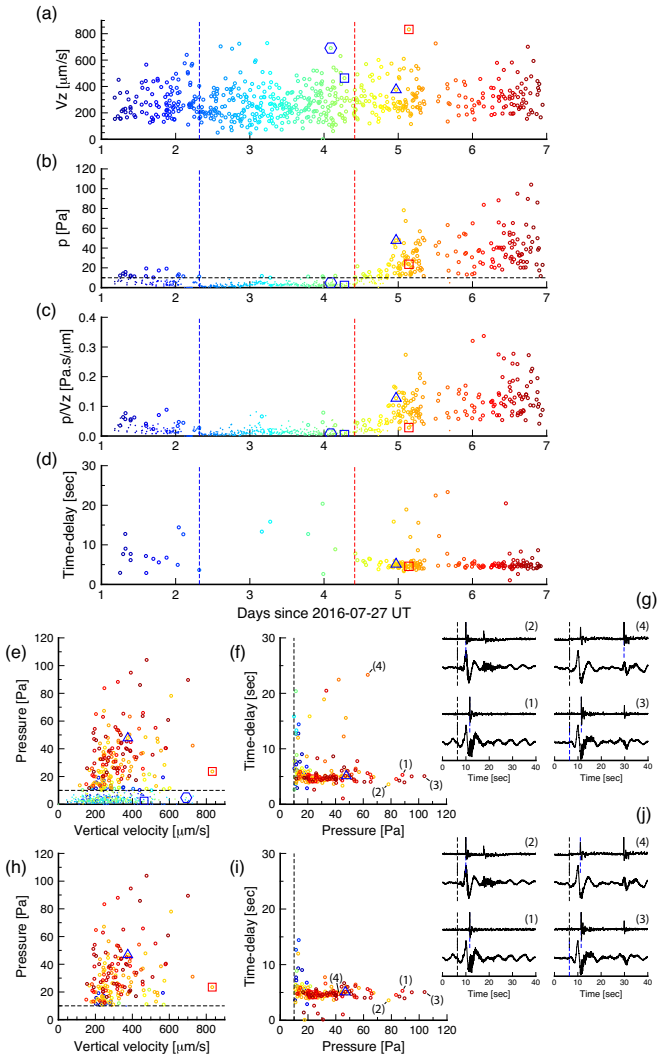

Figure 11. Infrasonic (YIB22) and collocated seismic (YS01-HHZ) amplitude and timing metrics for the 597 events in the dominant VLP seismic multiplet as defined by template matching. Both infrasound and seismic amplitudes are peak amplitudes of unfiltered waveform data in a 30 s window based on the seismic VLP template detection trigger time (i.e. the time from 0 to 30 s for the waveforms shown in Fig. 10). (a)–(d) show events as a function of time since 00:00, 27 July 2016 UT, with events colour-coded by time to facilitate comparison with (e) and (f). (a) Peak vertical-component velocity amplitude [μm s^{-1}] at YS01. (b) Peak infrasonic amplitude [Pa] at YIB22 (within the same absolute 30 s time-window). A threshold value of 10 Pa (horizontal dashed line) is used to approximately discriminate signal (infrasound pulse associated with VLP) from noise measurements (no infrasound pulse associated with VLP). Seismic VLP event times that have a corresponding peak infrasound amplitude less than the threshold 10 Pa are displayed as dots; above the threshold circles are used. (c) Amplitude ratio of infrasonic pressure to vertical seismic velocity p/V_z. Seismic VLP event times that have an infrasound amplitude less than the threshold 10 Pa are displayed as dots. (d) Time-delay of the peak infrasonic amplitude relative to the first-break (downward first-motion) in the seismic VLP. Time-delay measurements are only displayed for events with infrasonic amplitude above the threshold 10 Pa. Time-delay measurements for VLP seismic events with little to no infrasound near the threshold cut-off (low infrasonic amplitude and low p/V_z) prior to Day ~4.5 represent noise. (e) Infrasonic amplitude [Pa] at YIB22 versus collocated seismic vertical-component velocity amplitude [μm s^{-1}] at YS01. Events with infrasound amplitude below the 10 Pa threshold cut-off (horizontal dashed line) are displayed as dots. (f) Time-delay (same as d) versus infrasonic amplitude. The 10 Pa threshold cut-off is shown by a vertical dashed line; scatter in values close to the cut-off represent noise. The tight clustering of time-delay values with modal value 4.5 s is the robust feature of this figure. Time-delays >10 s result from multiple infrasound events contaminating the time-delay measurement in this simple scheme (see g). Four representative events labelled (1) to (4) are highlighted and their waveforms are displayed in (g) for illustration. (g) Unfiltered and normalized vertical seismic (YS01-HHZ) and infrasound (YIB22) waveforms for four representative events highlighted in (f) to illustrate the time-delay measurement. The reference start time is the onset of the downward first motion in the seismic VLP of the multiplet stack (vertical dashed black line). The infrasound time delay is based on the maximum infrasound amplitude (pick time shown as vertical blue dashed line in each case) in a 30 s window beginning at 0 s on this plot. For event (4), the time-delay measurement is contaminated by a later infrasound arrival with higher amplitude; the correct value should be ~4.7 s in this case for the earlier lower amplitude event and more consistent with the other events. However, some smaller scatter in the time-delay is robust; e.g., event (1) has time-delay 5.3 s while event (2) has time-delay 3.6 s. In Figs 11(a)–(f), we also highlight four events displayed in other figures. Red square: the seed event at 03:27:16, 1 August 2016 UT (Fig. 9a); blue square: event at 06:35:17, 31 July 2016 UT (Fig. 9b) (not shown in Fig. 11d or f since below amplitude threshold for time-delay calculation); blue triangle: event at 23:18:02, 31 July 2016 UT (Fig. 9c); blue hexagon: event at 02:09:57, 31 July 2016 UT (Fig. 3) (not shown in Fig. 11d or f since below amplitude threshold for time-delay calculation). Vertical dashed lines in (a)–(d) represent time markers of 07:40:49, 29 July 2016 and 09:54:10, 31 July 2016 UT for comparison with Fig. 10. Figs 11(h)–(j) the same as Figs 11(e)–(g), respectively, but for an alternate procedure for picking the infrasound waveform (see text for details). See also Supporting Information Fig. S5.

follows a systematic temporal progression through the data set. Broadly, we observe a transition from seismic VLPs with infrasound (events ∼0–110) prior to 07:40:49, 29 July 2016, to seismic VLPs with weak or no infrasound (events 110–397); then, beginning at 09:54:10, 31 July 2016 UT, seismic VLPs have increasingly strong associated infrasound (events >397). The presence of powerful explosion infrasound is systematically associated with the high-frequency (>5 Hz) seismic phase (Fig. 10). The transition from VLPs without infrasound to those with powerful infrasound beginning at 09:54:10, 31 July 2016 UT broadly follows the amplitude trends described in Section 3.3 and the increase in explosivity and increased dominance of South Crater activity documented by Fitzgerald *et al.* (2020) and Jolly *et al.* (2017).

In Fig. 10, we also see variations in the duration of the infrasound and corresponding high-frequency (>5 Hz) seismic phase during these times of transition. Infrasound (and high-frequency seismic) waveforms progressively lengthen prior to 07:40:49, 29 July 2016 (events ∼0–110), and rapidly shorten during the transition to a more open system with powerful infrasound beginning at 09:54:10, 31 July 2016 UT.

Furthermore, Fig. 10(e) (which uses a high-pass filter >1 Hz) reveals a consistent LP phase in these waveforms. The waveforms in Fig. 10(e) are the same seismic data windows as in Figs 10(a) and (d) (i.e. time-windowed based on the VLP waveform), but filtered with a high-pass >1 Hz. The LP phase is a consistent and robust feature across all stations and components of the network (not shown here). The LP phase (Fig. 10e) is systematically (always) associated with the VLP with a consistent delay of ∼1 s from the onset of the VLP downward first motion. The LP phase (Fig. 10e) is distinct from the high-frequency (>5 Hz) seismic phase; the LP component is recorded for all VLPs including those without infrasound and a high-frequency seismic phase. Not shown here, we verified that this LP phase is visible when using a filter with a higher corner (up to >5 Hz). We also note that the LP phase for the individual events is not perfectly aligned in Fig. 10(e) (since waveforms are aligned based on the VLP). Future work (beyond the scope) could attempt to align, stack, and invert the LP phase for additional information on the source process (Section 5.5).

3.6.2 Amplitude and timing metrics

Fig. 11 summarizes observations at the collocated infrasonic (YIB22) and seismic (YS01) station, including the signal amplitudes, infrasonic pressure p to vertical seismic velocity v_z amplitude ratio (p/v_z) (Matoza *et al.* 2009), and relative arrival timing (Ripepe *et al.* 2001, 2005; Ishii *et al.* 2019) of infrasound corresponding to the 597 events in the dominant seismic VLP multiplet (i.e. the waveforms shown in Fig. 10). Example events shown in various other figures are highlighted in Fig. 11 for reference. Peak seismic amplitudes in Fig. 11 are based on the unfiltered data shown in Fig. 10(a) and thus reflect the dominant VLP signals.

We automatically estimate the time-delay of an infrasound signal relative to the first-break (downward first-motion) in the seismic VLP in two ways, representing two different first-order methods for automatically picking the infrasound: (1) by simply designating the infrasound 'associated' with the seismic VLP to be the maximum (highest) unfiltered infrasonic amplitude in a 30 s window based on the seismic VLP template detection trigger time (i.e. the time from 0 to 30 s for the waveforms shown in Fig. 10) (results shown in Figs 11d–g); and (2) by using peak detection (Duarte & Watanabe 2018) to identify the *first* occurring peak in the infrasonic waveform (high-pass filtered >0.1 Hz) above a threshold of 10 Pa in the same 30 s window used for (1) (results shown in Figs 11h–j and Supporting Information Fig. S5). Method (1) is more automated with fewer parameter choices, but fails in the presence of another infrasound event closely following in time from the initial event associated with the seismic VLP (see example event (4) in Fig. 11g). All time-delay values greater than ∼10 s shown in Figs 11(d) and (f) are artefacts of this issue with another infrasound event appearing in the time window. Time-delay measurements for VLP seismic events with little to no infrasound (low infrasonic amplitude and low p/V_z) prior to Day ∼4.5 in Fig. 11 represent noise. Motivated by these shortcomings, Method (2) is a more manually tuned method that performs better at picking the correct infrasound arrival associated with the seismic VLP (see example event (4) in Fig. 11j). Both methods are highly simplified and this procedure could be refined in future work by considering alternative methods for picking the infrasound arrival (e.g. Bueno *et al.* 2019).

Nevertheless, the following are robust results of the analyses presented (see also Supporting Information Fig. S5). The transition beginning at 09:54:10, 31 July 2016 UT from VLPs with weak or no infrasound to VLPs with powerful infrasound is marked by a progressive increase in infrasonic amplitude (Fig. 11b) while seismic VLP amplitudes remain in a similar range to those before the transition (Fig. 11a); accordingly, the p/v_z ratio increases after 09:54:10, 31 July 2016 UT (Fig. 11c). Once clear infrasonic signals are established (after 09:54:10, 31 July 2016 UT), infrasonic amplitude becomes loosely correlated with VLP seismic amplitude (Figs 11e and h), and the time-delays between seismic VLP onset and infrasound peak amplitude become relatively consistent (modal delay time is 4.5 s) (Figs 11d, f and i). However, the time-delay is not precise; there is minor variability in the time-delay on the order of ∼2 s (Figs 11f, g, i and j). The waveforms used for the time-delay measurement (modal delay time 4.5 s) were not corrected for seismic and acoustic propagation time (see Section 5.3). Station YIB22 is ∼630 m from the South Crater vents. Acoustic traveltimes computed using finite-differences incorporating topography (Iezzi *et al.* 2019) are 2.02 s and 2.39 s, for South and North Crater vents, respectively to the collocated station YIB22 and YS01 (Section 5.3).

3.7 Source localization of infrasound associated with seismic VLPs

The transition on 31 July 2016 from weak to strong infrasound with increase in eruption intensity (Fig. 4, Fig. 10, Fig. 11) also corresponds to a general shift from activity at North Crater to increased explosive activity at South Crater (Jolly *et al.* 2017; Fitzgerald *et al.* 2020). Jolly *et al.* (2017) determined this general infrasonic source migration by systematically computing the time-lag (relative acoustic arrival time) between infrasound stations YIF1 and YIF4 for coherent waveforms on the north and south sides of the crater rim (Fig. 1).

A comprehensive infrasound signal detection, discrimination, cataloguing, and source localization for this data set is beyond the scope of the present work. However, in Fig. 12, we show the locations of infrasound associated with the dominant seismic VLP multiplet using the reverse time migration finite-difference time-domain (RTM-FDTD) method of Fee *et al.* (2021). We attempt infrasound RTM-FDTD locations using the infrasound waveforms windowed around 522 seismic VLP event times (i.e. the infrasound waveforms shown in Fig. 10(c), but for stations YIF1 to YIF5), representing a subset of the 597 VLP dominant multiplet event times

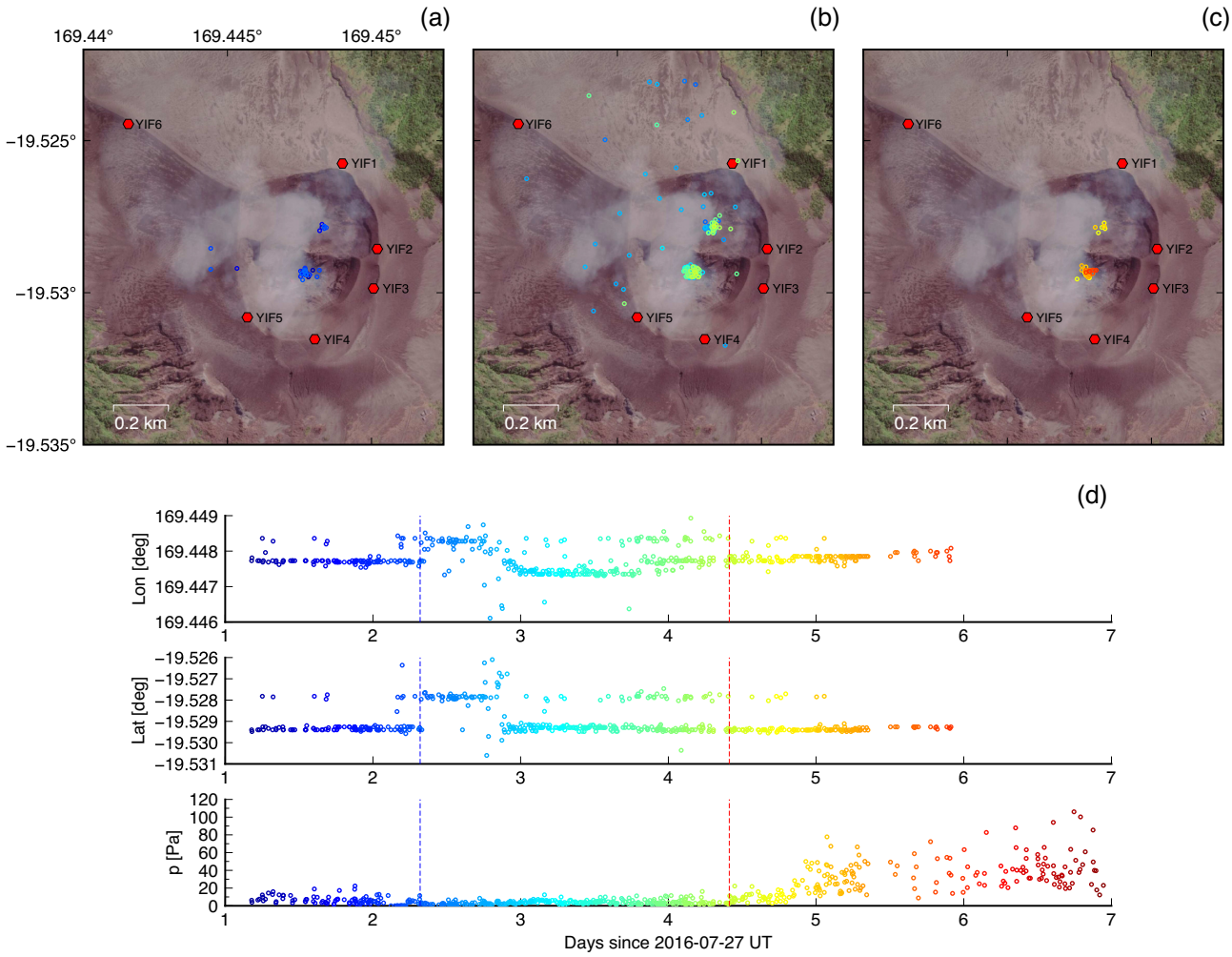

Figure 12. Location of infrasound associated with the dominant seismic VLP multiplet using the reverse time migration finite-difference time-domain (RTM-FDTD) method of Fee *et al.* (2021). Infrasound RTM-FDTD locations are attempted using the infrasound waveforms windowed around 522 seismic VLP event times, representing a subset of the 597 VLP event times for which the crater infrasound stations (YIF1 to YIF5, red hexagons in map panels) were in operation (Supporting Information Fig. S1). In the map panels (a, b, c), the infrasound RTM-FDTD source location estimates are displayed as circles with the colour-scheme corresponding to time (same as Figs 12d and 11). Map panels (a, b, c) are before, during, and after the high-amplitude infrasound decoupling from VLP. (a) events before 07:40:49, 29 July 2016; (b) events between 07:40:49, 29 July 2016 and 09:54:10, 31 July 2016; (c) events after 09:54:10, 31 July 2016 UT. (d) Longitude and latitude of the RTM-FDTD infrasound locations with time along with the infrasound peak pressure at YIB22 (same as Fig. 11b) for reference. Vertical dashed lines in (d) represent the time markers of 07:40:49, 29 July 2016 and 09:54:10, 31 July 2016 UT for comparison with (a, b, c) and Figs 10 and 11.

for which the crater infrasound stations (YIF1 to YIF5) were in operation. The RTM-FDTD was applied to the infrasound waveforms with a window duration of 20 s beginning 5 s after the seismic VLP template trigger (in Fig. 10, $t = 0$ is the start or trigger time of the seismic template), a (decimated) sampling rate of 40 Hz, a 0.2–4 Hz bandpass filter, and using a grid spacing of 4 meters in a 1400 × 1400 meter grid around the centre of the summit region. An RTM-FDTD solution is attempted for an infrasound waveform window at all of these VLP seismic trigger times, even for times when the infrasound amplitude is low or presumably noise (Fig. 12); RTM-FDTD solutions for noise produce scattered locations (see especially Fig. 12b). The map panels in Figs 12(a)–(c) correspond, respectively, to before, during, and after the significant change in seismic VLP and infrasound signal synchronization (Figs 10 and 11).

From the infrasound RTM-FDTD results shown in Fig. 12, the following interpretations can be made. Firstly, vents in both North and South craters were active acoustic sources at all times, even during the times of weak or no infrasound associated with seismic VLP (source decoupling). Thus, for seismic VLPs without strong infrasound between 07:40:49, 29 July 2016 and 09:54:10, 31 July 2016 (Figs 10 and 11), there is still weak signal that localizes to the vents in the RTM-FDTD (Fig. 12b). Presumably, this reflects low-level degassing and spattering activity as captured in Supporting Information Movie M3 (Section 3.5). These weak infrasound signals can be seen on Fig. 10(c) for station YIF5 between events ∼110–397, with other examples shown in Figs 3 and 9(b).

Secondly, at the initial transition into infrasound decoupling at 07:40:49, 29 July 2016, the infrasound (directly windowed around seismic VLP trigger time) abruptly changes location from the South to North crater. This lasts until approximately 19:12, 29 July 2016 UT (Day 2.8 on Fig. 12d), upon which infrasound source locations switch back to the South Crater and remain there through the transition back to powerful infrasound associated with seismic VLP.

Lastly, the infrasound source location results (Fig. 12) apparently capture activity at multiple closely spaced vents in South Crater, consistent with analysis by Jolly *et al.* (2017) and with the field (Fitzgerald *et al.* 2020) and video observations (Supporting Information Movies). However, this minor source location separation for the multiple closely spaced vents within South Crater is within the error of the RTM-FDTD procedure (Fee *et al.* 2021) and will require further evaluation in future work.

4 VLP WAVEFORM INVERSION

For the dominant VLP multiplet stack (Section 3.3.4, Fig. 7), we apply full-waveform inversion for a point-source representation consisting of a full moment-tensor (6 independent components) and a single-force vector (3 components). We begin with a 'free' inversion, without constraining the source geometry or mechanism (Section 4.1). Subsequently, based on results from the free-inversion, we perform inversions with moment-tensor mechanisms constrained to volumetric sources of a single-crack, single-pipe, dual-crack, dual-pipe, and pipe-crack, plus a single-force vector in each case (Section 4.2). The full-waveform inversion methodology follows that of previous literature (e.g. Ohminato *et al.* 1998; Kumagai *et al.* 2002; Chouet *et al.* 2003, 2005; Nakano & Kumagai 2005; Waite *et al.* 2008; Chouet *et al.* 2008, 2010; Chouet & Dawson 2011; Dawson *et al.* 2011; Lyons & Waite 2011; Chouet & Dawson 2013; Arciniega–Ceballos *et al.* 2012; Matoza *et al.* 2015; Chouet & Dawson 2015; Dawson & Chouet 2019) and is summarized in Appendix A. The inversions are performed here in the band from 0.02 to 2 Hz, but the observed VLP waveforms are dominated by frequencies >0.1 Hz (Fig. 8, Section 3.4) such that tilt (Maeda *et al.* 2011) can be neglected.

We compute the synthetic Green's functions using 3-D finite-differences (Ohminato & Chouet 1997) with 10-m discretized topography and a homogeneous velocity model with compressional wave velocity $V_p = 2400$ m s^{-1}, shear wave velocity $V_s = 1380$ m s^{-1}, and solid density $\rho = 2500$ kg m^{-3} based on values from Perrier *et al.* (2012) (a sensitivity test of the homogeneous velocity values is presented in Section 4.3). The topography model is based on a high-resolution (∼2 m) 2016 digital elevation model (DEM) for Yasur derived from a UAS survey and satellite images as described by Iezzi *et al.* (2019) and Fitzgerald *et al.* (2020). The model domain extends from 3 km depth below sea-level to the maximum DEM elevation of 350 m above sea-level.

We perform a grid search over trial source nodes with increasing spatial density in three stages down to 20-m spacing (Fig. 13), defining the solution with the minimum E_2 residual error and evaluating the relevance of model parameters using Akaike's information criterion (AIC) (Appendix A). The grid of trial source nodes is adapted around the resultant minimum E_2 solution at each stage in three iterations with: (1) 200-m spacing in X (east), Y (north) and 250-m spacing in Z; (2) 50-m spacing in X (east), Y (north) and 50-m spacing in Z; (3) 20-m spacing in X (east), Y (north) and 20-m spacing in Z (Fig. 13).

4.1 Free-inversion

The trial source nodes and the eight three-component seismic stations used in this study are shown in Fig. 13. Data were not recovered from seismic station YS07 after 31 July 2016; thus, all waveform inversion results presented here are for the seven stations excluding station YS07. A separate inversion for a subset of the data (waveform stack over a shorter time-range) including YS07 is presented in the Supporting Information (Fig. S6), demonstrating robustness of the results to dropping this station.

Residual per cent errors (E_2) for moment-only (6-mechanism; E_2 of 17.5 per cent) or force-only (3-mechanism; E_2 of 29.5 per cent) solutions are approximately an order of magnitude greater than for the 9-mechanism solution (moment-tensor plus single-force source; E_2 of 4.21 per cent). The source locations for the moment-only and force-only solutions are also mislocated away from the summit region; thus, we do not consider these source-types further and focus on the 9-mechanism solution. AIC further confirms the relevance of the 9-mechanism solution.

The 9-mechanism free-inversion solution (minimum E_2 of 4.21 per cent) is located directly beneath the summit vent region at 740 meters below sea-level or 910 meters below the topography at this location (Table 1, Fig. 13). We note that the best-fit (minimum) E_1 (e.g. Matoza *et al.* 2015) location is within 20 meters of the E_2 solution in both X and Y and at the same depth. The 9-mechanism solution is composed of a dominantly volumetric moment-tensor plus a single-force vector with a significant vertical component (Fig. 14a). The source–time functions are consistent between separate mechanism components (Fig. 14a), which is not prescribed in the free-inversion and thus an indication of a stable solution. Observed and synthetic waveforms are in close agreement (Fig. 15), as reflected by the relatively low residual error. Additionally, the residual error volume (Fig. 13b) has a simple ellipsoidal structure with one clear minimum, indicating a well-defined source location solution. We note that the source–time functions are relatively long duration, with an oscillatory component visible especially in the M_{zz} and F_z waveforms beyond ∼40 s (Fig. 14a), reflecting the observed protracted multiplet waveform (Figs 7f and g).

For the minimum E_2 solution, the weighted arithmetic mean of eigenvector ratios as derived from statistics of the source–time functions is approximately [1.00: 1.15: 1.32], pointing to a composite mechanism. For example, assuming hot rock with Lamé coefficients $\lambda = 2\mu$, the principal axes for a horizontal crack are given by: $2\mu\Delta V$[1: 1: 2] (Chouet 1996). Normalizing the observed eigenvector ratios to a maximum value of 2, we obtain ratios [1.52 : 1.74 : 2.00]. This can be obtained with various combinations of cracks and pipes, which we investigate in Section 4.2.

For the minimum E_2 free-inversion solution, the ratio of the peak-to-peak amplitudes of the source–time functions F_z/M_{zz} is approximately 0.7×10^{-3} m^{-1}. The vertical single force F_z contributes ∼6–9 per cent of the observed vertical-component displacements across the network compared to the vertical dipole moment M_{zz} for the minimum E_2 source location; this estimate is derived from the amplitude ratios of the synthetic Green's functions for vertical components across the network for M_{zz} and F_z sources located at the minimum E_2 source location, combined with the $F_z/M_{zz} \sim 0.7 \times 10^{-3}$ m^{-1} for the obtained solution.

The source–time functions between separate mechanism components of the minimum E_2 free-inversion solution (Fig. 14a) track closely and are consistent, but are slightly out of phase, with the maximum of the $M_{zz}(t)$ source–time-function slightly preceding that of the $M_{xx}(t)$ and $M_{yy}(t)$ waveforms by ∼0.15 s. Although minor, this results in a slight torquing of the moment-tensor components when viewed as a point-by-point eigenvector quiver visualization (Fig. 14d). We further investigate this mechanism phase-stability in Section 4.3 using the γ metric of Matoza *et al.* (2015) (Appendix A).

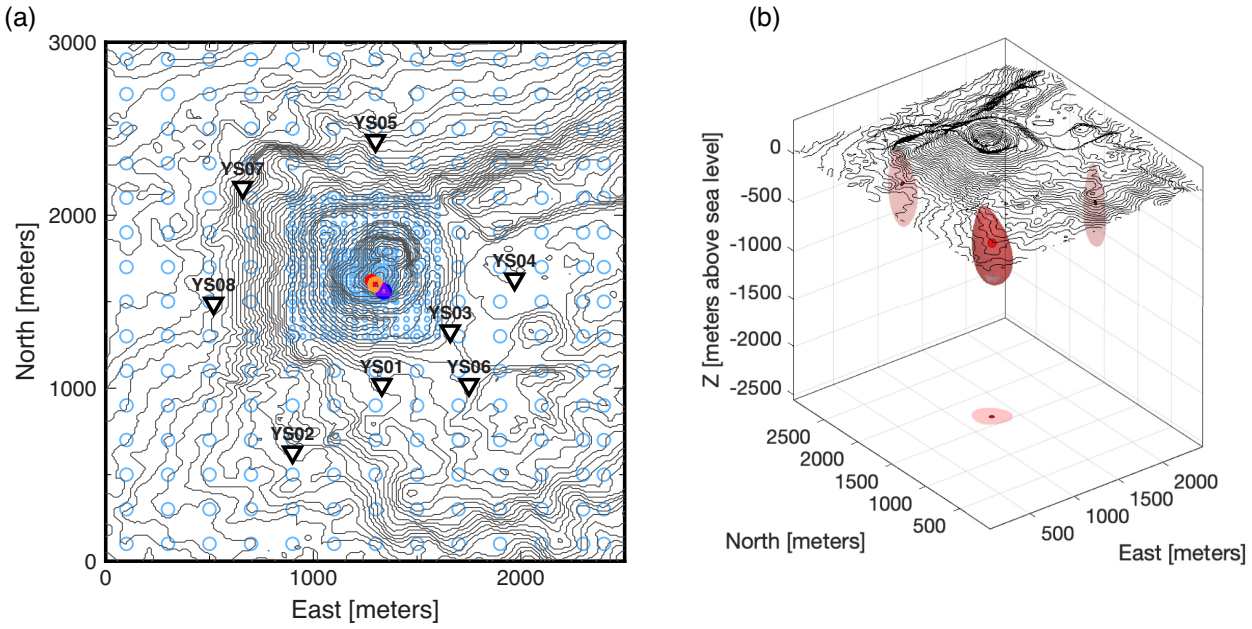

Figure 13. Model domain used for full-waveform inversion with 10-meter digital elevation model (Iezzi *et al.* 2019). East X, and north Y [meters] are with respect to an origin at (335831E, 7838247N) UTM Zone 59 S. (a) Light blue circles are trial source-nodes used for Green's function computations using reciprocity with the seismic station locations (inverted triangles). Inversions were performed adaptively in three stages with a progressively denser trial source-node mesh enclosing the source. Minimum E_2 solution epicentres are shown for the 9-mechanism free-inversion (red filled circle) and mechanism-constrained inversions with one crack (dark blue circle), two cracks (dark blue square), one pipe (orange circle), two pipes (orange square), and pipe-crack (purple triangle) (locations and displayed symbols overlap; see Table 1). (b) E_2 residual error volume for the 9-mechanism free-inversion. The red isosurface is 0.5 per cent above the minimum E_2 location (red dot). Projections of the 0.5 per cent isosurface and minimum E_2 centroid are shown as shadows on the opposite faces of the Cartesian projection. The derived source locations are directly beneath the main summit vents. See Tables 1 and 2 for more details.

Table 1. VLP source-mechanism inversion results based on minimizing E_2. For the free-inversion, number of mechanisms $N_m = 9$ implies six independent moments plus three forces. For the constrained-mechanism inversions, N_m implies three forces plus a moment (volume change) mechanism from each geometrical structure. Source epicentre locations X, Y [meters] are with respect to an origin at (335831E, 7838247N) UTM Zone 59 S (see Fig. 13) and converted to longitude, latitude [degrees] for reference. Z_{sea} is depth [meters] below sea level; Z_{topog} is depth [meters] below topography. E_2 and AIC are computed from a 55 s portion of the waveform.

Description	N_m	X [m]	Y [m]	Lon. [°]	Lat. [°]	Z_{sea} [m]	Z_{topog} [m]	E_2 [%]	AIC
Free	9	1280	1620	169.44754	−19.52930	740	910	4.21	−912149
One crack	4	1340	1560	169.44810	−19.52984	800	1000	9.49	−678946
One pipe	4	1300	1600	169.44773	−19.52948	800	970	12.34	−603072
Two cracks	5	1340	1560	169.44810	−19.52984	760	960	7.20	−758387
Two pipes	5	1300	1600	169.44773	−19.52948	800	970	10.32	−654616
Pipe-crack	5	1340	1560	169.44810	−19.52984	720	920	7.15	−760358

4.2 VLP source reconstruction (constrained-mechanism inversions)

The results for a free-inversion (Section 4.1) point to a composite source mechanism, which we further investigate using inversions with moment-tensor mechanisms constrained to volumetric sources of a single-crack, single-pipe, dual-crack, dual-pipe, and pipe-crack, plus a single-force vector in each case (e.g. Nakano & Kumagai 2005; Chouet *et al.* 2010; Chouet & Dawson 2011). Rather than simply model the source at the free-inversion best-fit E_2 location, we perform these constrained-mechanism inversions at each of the trial source node locations in the finest (3rd-iteration) mesh (Fig. 13) to enable more exploration of the model space and allow trade-offs between mechanism and source location. For each of the trial source nodes in the densest mesh enclosing the free E_2 solution, we investigate a set of forward models for volumetric sources of a single-crack, single-pipe, dual-crack, dual-pipe, and pipe-crack, plus a single-force vector in each case, then identify the minimum E_2 location for each source type.

The number of mechanisms N_m in this case corresponds to three forces plus a moment (volume change) mechanism for each geometrical structure (e.g. $N_m = 4$ for a single-crack plus 3 forces; $N_m = 5$ for a dual-crack or pipe-crack composite plus 3 forces) (Tables 1, 2). Each volumetric source is characterized by two angles: θ (angle from vertical) and ϕ (measured counter-clockwise from the east) (see Table 2). The forward-modelling proceeds in four iterations with progressively finer sampling in (θ, ϕ) down to $\pm 1°$ increments around the best-fit (E_2) angle in each case. For a single mechanism, it takes approximately 215 rotations to find the best fitting orientation. For a dual mechanism, it takes approximately 14 000 individual rotations over both mechanisms to find the minimum error and best orientation of each mechanism.

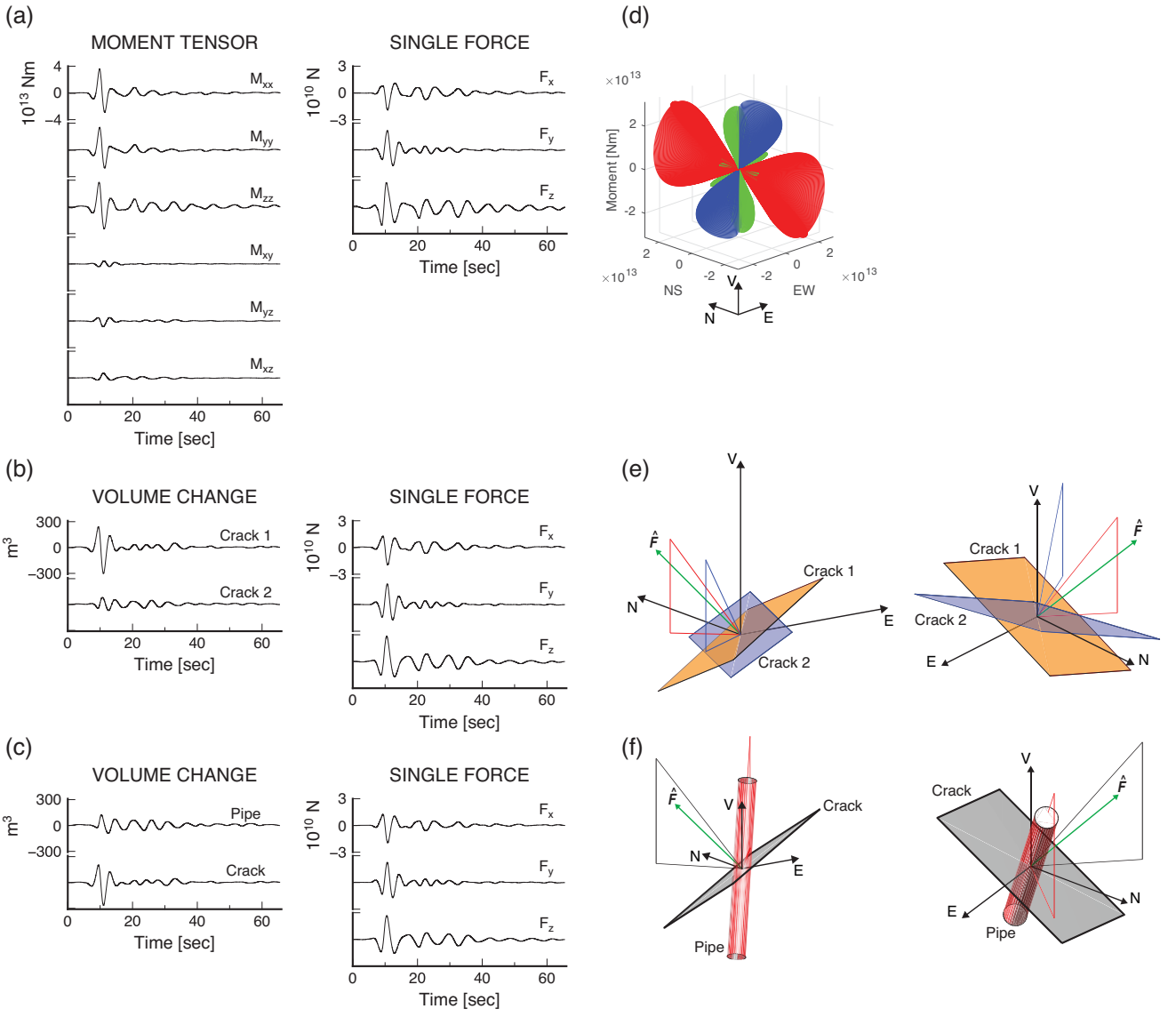

Figure 14. Source–time functions for the minimum E_2 solution in each case for (a) a free-inversion with six independent moment and three single-force components; (b) a constrained mechanism inversion with two cracks and three single-force components; (c) a constrained mechanism inversion with one pipe plus one crack and three single-force components (see Tables 1 and 2). In (b) and (c), the volume-change is calculated from the moment source–time function assuming a shear-modulus $\mu = 1 \times 10^{10}$ Pa and a Poisson's ratio of 1/3 at the source ($\lambda = 2\mu$), appropriate for volcanic rock at or near liquidus temperatures (Chouet 1996). (d) Quiver plot of point-by-point maximum (red), intermediate (blue), and minimum (green) moment-tensor eigenvectors scaled by the eigenvalues for the 9-mechanism free-inversion solution shown in (a); only portions of the source–time functions corresponding to $M_{xx}(t) \geq 0.4 \max\{M_{xx}(t)\}$ are used to construct this plot. (e) Geometry of the dual-crack source shown in (b) at two different viewing angles. (f) Geometry of the pipe-crack source shown in (c) at two different viewing angles. V: Vertical, E: East, N: North. A green arrow shows the single-force vector. Guidelines are shown to indicate the angles θ (from vertical) and ϕ (measured counter-clockwise from east) used in Table 2 for each source. Crack planes are depicted schematically in a rectangular geometry, but a different crack geometry such as a penny-shaped crack (Section 5.4) is also compatible with the solutions.

The results of this procedure are summarized in Tables 1 and 2 and Figs 14b, c, e and f. The constrained-mechanism best-fit (E_2) locations are all close to each other and to that of the free-inversion, showing consistent and stable results. All constrained-mechanism solutions have minimum E_2 values greater than that of the free inversion, as expected for the constrained procedure. Of the constrained-source solutions, the dual-crack and pipe-crack (plus forces in each case) have comparable E_2 and AIC values (Table 2) and are essentially indistinguishable given the available data. Thus, the dual-crack or pipe-crack (plus forces) composite sources represent our final (best candidate) solutions. The source–time functions and geometries of the best-fit dual-crack and pipe-crack solutions are shown in Figs 14b , c, e and f.

Nevertheless, the results are consistent for the different inversions. For example, the dominant crack in the dual-crack model has a similar waveform to that of the single-crack model and also has a similar orientation (Table 2). In addition, the dominant crack in the dual-crack model has a similar waveform and orientation to the crack in the pipe-crack model (Table 2). The crack volume-change source–time functions in each case track well with the volumetric components of the free moment-tensor source (Fig. 14a), and the

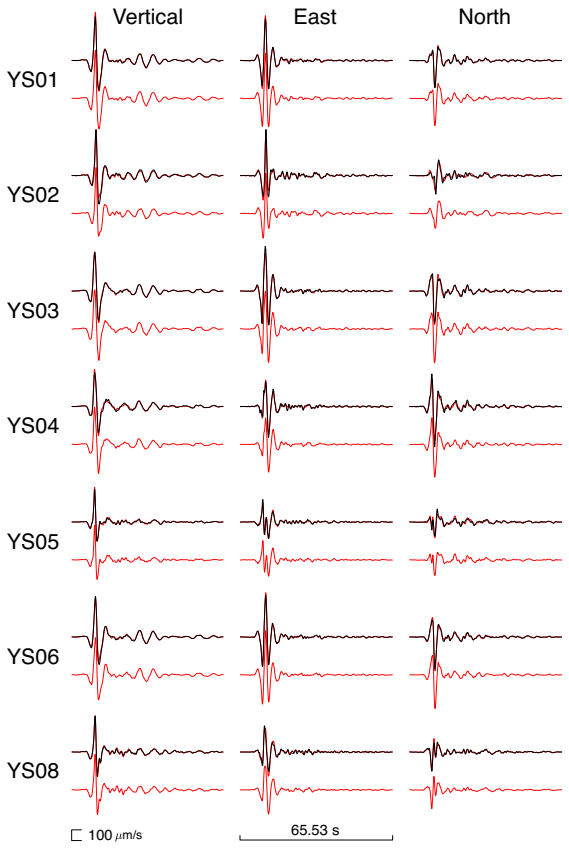

Figure 15. Waveform fits comparing data and model synthetics for the minimum E_2 free-inversion solution. Velocity data filtered in the band 0.02–2 Hz for the dominant multiplet stack used in the inversion are shown in black; synthetic waveforms for a source corresponding to the minimum E_2 free-inversion solution (see Table 1) with six moment and three single-force components are shown in red.

Table 2. Orientations of moment-mechanisms and single-force vectors for the solutions shown in Table 1. All angles in degrees. θ is angle from vertical, ϕ is measured counter-clockwise from the east. For the constrained-mechanism inversions, subscripts 1 and 2 refer to the two constrained mechanisms, respectively (e.g. for the pipe-crack, 1 refers to the pipe while 2 refers to the crack). For the constrained-crack mechanism, (θ, ϕ) correspond to the dominant dipole component normal to the crack plane. For the constrained-pipe mechanism, (θ, ϕ) correspond to the cylinder axis. For the free-inversion, subscript 1 refers to the dominant eigenvector orientation of the full moment-tensor. In all cases, subscript F refers to the accompanying single-force unit vector direction.

Mechanism	θ_1	ϕ_1	θ_2	ϕ_2	θ_F	ϕ_F
Free	40	138	–	–	47	132
One crack	41	129	–	–	46	132
One pipe	35	283	–	–	45	127
Two cracks	36	140	38	207	47	130
Two pipes	40	356	42	265	40	132
Pipe-crack	34	49	39	132	48	131

orientation of the dominant eigenvector of the free-moment tensor points in approximately the same direction as the normal to the dominant crack plane in the single-crack, dual-crack, and pipe-crack mechanisms (Table 2).

Lastly, we estimate the direction (unit vectors) of the single-forces accompanying each source using the peak amplitudes of the source–time functions of the single-forces (Table 2). The derived force-vector is approximately orthogonal to the primary crack plane in the single-crack, dual-crack, and pipe-crack mechanisms, and the force-vector and principal eigenvector for the free-inversion are correspondingly aligned (Tables 2).

4.3 Additional sensitivity testing

The results presented in Sections 4.1 and 4.2 remain our preferred and best solutions given the available data. However, here we further investigate the minor torquing or 'flutter' in the volumetric moment-tensor eigenvector source–time-functions for the minimum E_2 free-inversion solution (Fig. 14d). This minor-phase mismatch in the derived source–time-functions could reflect a real property of the source. For example, this effect could arise from two (or more) radiating point sources or a distributed finite-source insufficiently approximated by a single point-source (Nakano *et al.* 2007; Chouet *et al.* 2008). A dominant source consisting of one or more elements (two cracks) may contribute most of the energy, with a subjacent and subdominant source also present. Here we briefly investigate other possible explanations.

A first possibility is that the minor torquing of moment-tensor eigenvector components (Fig. 14d) results from a stacking artefact. Since we invert multiplet waveform stacks (Section 3.3), minor phase differences in the contributing normalized waveforms for individual events at each station may result in artefacts. To test this, we performed a separate 9-mechanism free-inversion only on the single high-amplitude VLP seed event waveforms (single event at 03:27:16.38, 1 August 2016 UT). The minimum E_2 (3.28 per cent) location for the seed event is very close to that of the multiplet stack (the seed is offset 20-m to the west and 60-m deeper than the multiplet stack). The derived source–time-functions and mechanism for the seed event are highly similar to that of the multiplet stack. The minor torquing of moment-tensor eigenvector components is also observed for the seed event inversion, ruling out a stacking artefact as the explanation.

Next, we investigate the effect of possible source mislocation by systematically assessing the metric γ (Appendix A; Matoza *et al.* 2015) for every node in the intermediate and finest-density trial-source-node meshes (Fig. 13). The metric γ is a measure of source–time-function phase stability; low values of γ correspond to a temporally stable volumetric moment tensor (Appendix A). The minimum E_2 free-inversion solution presented in Section 4.1 (Table 1) has $\gamma = 0.70$, $E_2 = 4.21$ per cent. Within the densest trial-source node mesh, only minor improvements (reduction) in γ at the expense of higher E_2 error could be found. For example, a source location 20-m south and 140-m shallower than the minimum E_2 solution has $\gamma = 0.43$ and $E_2 = 4.29$ per cent; no solutions could be found without the minor torquing of moment-tensor eigenvector components. Within the wider intermediate trial source node mesh (Fig. 13) a minor reduction in γ (global minimum $\gamma = 0.11$) can only be achieved at the expense of significantly higher $E_2 = 15.51$ per cent (poorer waveform fit) and an unrealistic source location that is offset from the main summit vent area in the southeast corner of the model domain; accordingly, we disregard these solutions. Compared to the results of Matoza *et al.* (2015), who presented a solution corresponding to minimum $\gamma \sim 0.01$ within 5 per cent of minimum E_1 and within 10 per cent of minimum E_2, the minor improvement in γ achievable here for the Yasur VLP inversion is not significant. The use of γ does not identify a better solution for this data set.

We also performed a velocity model test, investigating the effect of using higher values of velocity than those used for the main results presented (Sections 4.1 and 4.2). We repeated the entire free-inversion procedure (of the multiplet stack) using a homogeneous velocity model with $V_p = 3500$ m s^{-1}, $V_s = 2000$ m s^{-1}, and $\rho = 2650$ kg m^{-3} based on values used for Stromboli by Chouet *et al.* (2003). The results from this test are very similar to those obtained in Sections 4.1 and 4.2 with the velocity model based on values from Perrier *et al.* (2012). The source location is almost the same, but the E_2 error is slightly higher for a higher velocity model. For this higher velocity model, the resultant minimum E_2 (4.92 per cent) location is close to that obtained in Sections 4.1; the derived source location is 30-m to the west, 50-m to the north, and 40-m shallower than the minimum E_2 location presented in Section 4.1 (Table 1). The corresponding source–time-functions (not presented here) are barely distinguishable from those in Fig. 14(a), but have higher amplitudes; moments are on the order of $\sim 1 \times 10^{14}$ Nm and forces are $\sim 7 \times 10^{10}$ N. These results are consistent with tests by Chouet *et al.* (2003). Similar minor torquing of moment-tensor eigenvector components is also observed for the solution based on the higher velocity model; thus, raising the homogenous velocity values does not eliminate this feature of the derived source–time functions.

Lastly, we eliminate the possibility that air-to-ground coupled waves (Matoza *et al.* 2014, 2019a) may have influenced the seismic VLP waveform stacks and inversion results. We performed a separate VLP waveform stack using only events in the dominant VLP multiplet without significant infrasound; i.e., events between 07:40:49, 29 July 2016 and 09:54:10, 31 July 2016 UT (Figs 10 and 11). The resultant stacks and waveform inversion results are barely distinguishable from the main results presented, confirming that air-to-ground coupling does not significantly affect the inversion results presented. This is also expected since the inversions are performed in the band from 0.02 to 2 Hz and air-to-ground coupling is typically observed at higher frequencies >5 Hz (Matoza *et al.* 2014).

More extensive sensitivity testing is beyond the scope of this study, but the fundamental sensitivity testing presented here supports the relative robustness and self-consistency of the major results presented in Section 4.1–4.2 based on the available data. Given the number of available seismic stations, we do not have adequate data (network coverage) to attempt an inversion for multiple point-sources or an extended (finite) source (Nakano *et al.* 2007; Chouet *et al.* 2008). A future field campaign at Yasur using a greater station density could improve knowledge of the shallow velocity structure and may permit multiple point-source or finite-source inversions.

5 DISCUSSION

Full-waveform inversion of the dominant VLP multiplet stack points to a composite source consisting of either a dual-crack (plus forces) or pipe-crack (plus forces) mechanism (Section 4). All of the derived mechanisms are consistent and correspond to point-source centroid depths in the range ∼900–1000 m below topography and ∼700–800 m below sea level (Table 2). All mechanisms suggest a northeast trending crack dipping relatively shallowly to the northwest; this alignment broadly follows the larger structure shown in Fig. 1(d) (Carney & McFarlane 1979; Brothelande *et al.* 2016b), indicating a VLP source centroid and mechanism controlled by a stable structural geologic feature beneath Yasur (c.f., Matoza *et al.* 2014). We consider the dual-crack (plus forces) solution the most plausible geometry considering geologic and fluid dynamic perspectives (Chouet *et al.* 2010; Section 5.1). A crack-like morphology is more likely from a geologic perspective, as cracks provide a natural geometry for fluid transport at depth in the Earth (Rubin 1995). The VLP source-centroid depths we obtain for Yasur are similar to those obtained for VLPs at Kīlauea, Hawai'i (Chouet *et al.* 2010; Chouet & Dawson 2015) and pre-eruption VLPs at White Island (Whakaari), New Zealand (Jolly *et al.* 2018). In addition, our derived VLP source-mechanism geometries are similar to those obtained for VLP explosion signals at Popocatépetl (Chouet *et al.* 2005), Augustine (Dawson *et al.* 2011), and Redoubt (Haney *et al.* 2013). In these three cases, the sources were interpreted as an inclined sill that sits at the base of the volcanic edifice, at the contact of the volcanic pile with the underlying palaeostructure; this type of structure is discussed by Gudmundsson (2002).

The high-rate and highly repetitive VLP dominant multiplet explains the bulk of seismicity recorded during our experiment, indicating that the dominant VLP source corresponds to a major stable geometrical discontinuity in Yasur's magma transport system. This geometrical discontinuity must provide an efficient coupling location for pressure since the VLP source is narrowly localized in space and highly stable temporally. Additionally, we must explain the major observation of a systematic progression in VLP seismic decoupling and reconnection with surficial explosions, infrasound, and high-frequency seismic phase over a timescale of a few days during our field campaign (Section 3). The additional higher frequencies in the seismic waveforms track well with the infrasound and are a characteristic seismic signature of surficial explosions (e.g. Figs 2, 9 and 10).

We interpret the results in the framework of the transit of a large slug of gas through the conduit responsible for Yasur explosions (Harris & Ripepe 2007). A simplified diagram showing the main elements of our conceptual model is presented in Fig. 16. The basic elements of the interpretation (Fig. 16) are a deep section (>1 km) characterized by gas slug coalescence; an intermediate section in which gas slug ascent occurs relatively aseismically; and a shallow section immediately beneath the summit vents, which may variously buffer the terminal slug ascent. The VLP source for the dominant multiplet is located at the base of the intermediate section, and represents an element of the pathway from the deep to intermediate sections, with the stable geometry possibly controlled by palaeo-Siwi and Yenkahe geologic structure (Carney & McFarlane 1979; Brothelande *et al.* 2016b).

Water exsolution calculations based on conditions suggested by Métrich *et al.* (2011) indicate that Yasur magma would be exsolving water at pressures of ∼15 to 30 MPa. Considering an average ∼20–25 MPa and crustal density $\rho \sim 2500$ kg m^{-3} yields a depth of bubble formation of ∼1 km. This water exsolution depth estimate varies as a function of assumptions on temperature and initial water content. Application of an equilibrium thermodynamic model using water content of 0.2 to 1.8 wt. per cent broadly reproduces the crystal content and composition of the erupted scoria collected during our field campaign at Yasur. The upper bound water content of 1.8 wt. per cent results in exsolution beginning at ∼1.5 km depth, whereas at the lower bound of 0.2 wt. per cent, exsolution occurs at ∼100 m depth and is considered too shallow to be plausible. Therefore, it is possible that between ∼1.5 km and 900 m depth beneath Yasur, slugs are being formed (deep section on Fig. 16).

We envision the VLP source centroid as the base of the intermediate conduit section that feeds from this deeper plumbing system

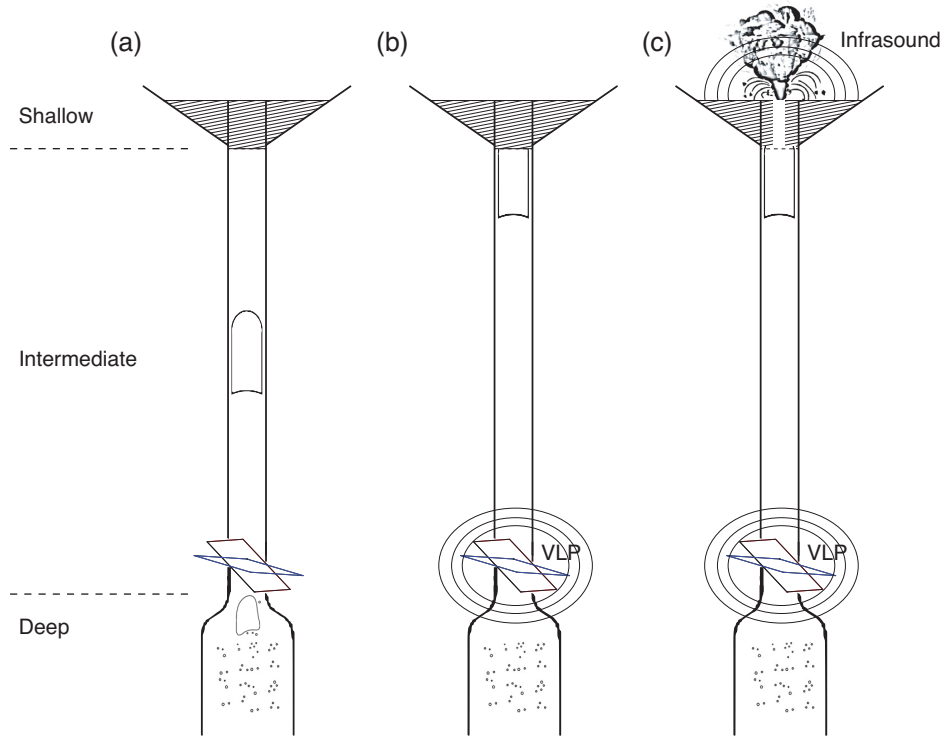

Figure 16. Conceptual diagram of the dominant VLP source at Yasur and its proposed relation to magma and gas transport systems and surficial explosions and infrasound. The basic elements are a deep section (>1 km) characterized by gas slug coalescence; an intermediate section in which gas slug ascent occurs relatively aseismically; and a shallow section immediately beneath the summit vents, which may intermittently buffer the terminal slug ascent. The VLP source for the dominant multiplet is located at the base of the intermediate section, and represents an element of the pathway from the deep to intermediate sections, with geometry controlled by stable geologic structure. (a) Aseismically, a gas slug migrates from the deep to intermediate sections and rises through the intermediate section. (b) Gas slug arrives at the base of the shallow section (top of the intermediate section), upon which the VLP seismic source is triggered in response at the base of the intermediate section (see text for details). In this case, buffering in the shallow section prevents or limits an immediate response of surficial explosion and infrasound. (c) As in (b), but for a relatively open shallow section; the arrival of the slug at the base of the shallow section similarly triggers the same VLP source at depth and is followed rapidly (within a few seconds) by a surficial explosion and infrasound.

section below (Fig. 16). The water exsolution depth range ∼1.5 km to 900 m is slightly below and overlapping the derived VLP source centroid depth of ∼900–1000 m below topography. A natural explanation is that H_2O-rich slugs (H_2O is the dominant gas species identified through Fourier-transform infrared spectroscopy (FTIR) analysis; Woitischek *et al.* (2020)) coalesce in a bubble trap accumulation feature or dendritic feeding system (deep section, Fig. 16), rise from there (aseismically) through the dual-crack system controlled by dominant geologic structure, and up (aseismically) through the intermediate conduit section. Upon reaching the near-surface shallow section which serves as a buffer (Fig. 16), the VLP is triggered at the base of the intermediate section (Fig. 16b). Slug disruption in the near-surface shallow zone (Sections 5.2 and 5.3) triggers a pressure disturbance that propagates downward at the speed of the crack wave and couples at the geometrical discontinuity at the base of the conduit (the location of the VLP centroid). A surficial explosion with corresponding infrasound and high-frequency seismic phase may (Fig. 16c) or may not (Fig. 16b) be produced depending on the state of the buffer. The dual-crack system which serves as the VLP source may be a constriction serving as a valve on the deeper section, but the presence of the dual-crack system or jog in the conduit at this location would suffice to provide an efficient coupling location for the VLP source. We elaborate on and further justify several aspects of this model in the following subsections.

5.1 VLP source mechanism

In the dual-crack mechanism volume-change source–time functions (Figs 14 and 17), we observe a maximum downward swing (deflation) of the dominant crack (Crack 1) starting at about 9.5 s in the source waveform (Fig. 17), which corresponds to an upward swing of the dominant vertical force component. The vertical single force represents an exchange of linear momentum between the source volume and the rest of the Earth. In the fluid-filled conduit or dike envisioned under Yasur, an exchange of linear momentum occurs when the centre of mass of the fluid accelerates upward (or downward) as a result of a change in the mass distribution in the source volume. Momentum exchange takes place through a normal force applied at the top and bottom boundaries of the source volume, or through a shear-force exerted on the boundaries oriented parallel to flow.

Following Chouet *et al.* (2010), two scenarios provide potential explanations for the process underlying the VLP source at Yasur. In scenario one, the causative flow process is collocated with the VLP source and the root cause of the flow disturbance is the transit of a large slug of gas through a conduit discontinuity. An example is a conduit flare at this location (James *et al.* 2006). In scenario two, the VLP source only represents a coupling location for pressure changes generated by a flow process occurring elsewhere in the conduit, namely the near-surface expansion of the decompressing slug (James *et al.* 2008, 2009).

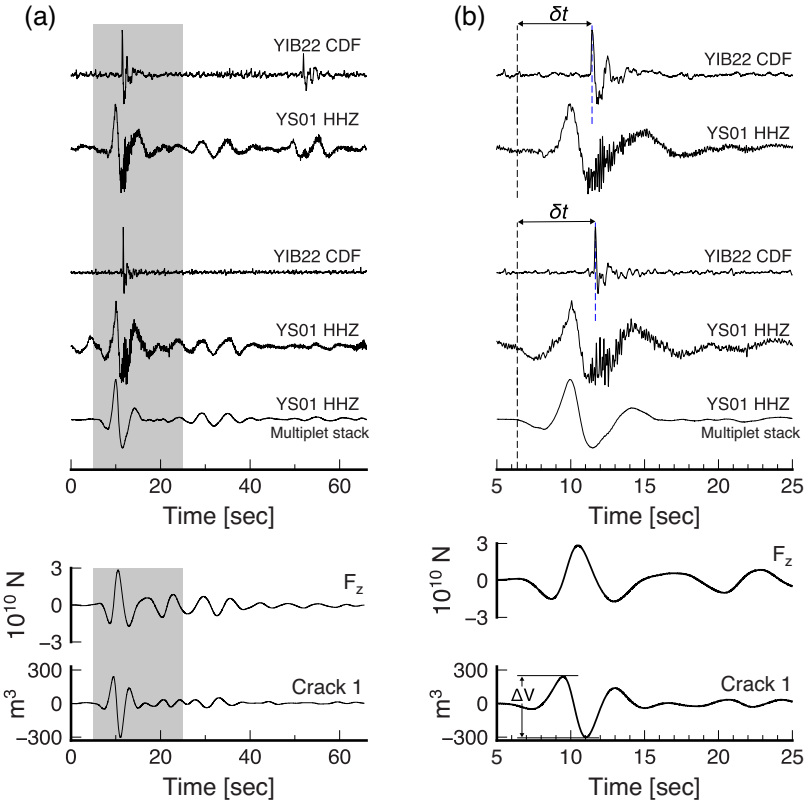

Figure 17. Timing of major waveform features discussed in the text in relation to the source process. Grey region in (a) shows the time-range expanded in (b). The lower panels indicate the source–time functions for the dominant crack (Crack 1) volume change and the vertical single force (F_z) components of the dual-crack plus forces source (same solution as displayed in Fig. 14b; see also Tables 1 and 2). The upper panels show the normalized and unfiltered waveforms at collocated seismic station (YS01, vertical component HHZ channel code) and infrasound station (YIB22; CDF infrasound channel code) for two different individual events within the dominant multiplet defined by template matching, as well as the multiplet template stack for YS01 HHZ. The upper raw event has a plot origin time of 23:18:02 31 July 2016 and is the same event as shown in Fig. 9(c). The lower raw event has a plot origin time of 08:26:04 2 August 2016 and is also displayed in Figs 11(g) and (j) as event (1) there. In (b), δt is the time-delay from the onset of the VLP downward first-motion (picked from the multiplet stack) to the infrasound peak amplitude (Sections 3.6.2 and 5.3) and has values $\delta t \sim 5.1$ and 5.3 s, for the upper and lower events, respectively (modal δt for all events is 4.5 s; Section 3.6.2). ΔV is the maximum peak-to-peak volume change of Crack 1 (Section 5.4). No corrections for seismic or acoustic propagation time have been made to any waveforms in this figure.

A complex picture emerges when considering these scenarios for the VLP driving process in light of the observed decoupling and desynchronization of the dominant VLP seismic source with surficial infrasound and large explosions (Section 3). For the case of VLPs within the dominant multiplet that do have appreciable infrasound (e.g. the event shown in Fig. 9c), scenario one (above) is implausible. If the causative flow disturbance driving the VLP occurs at a conduit discontinuity at ∼900–1000 m depth, the slug ascent from there to the surface with an estimated velocity of ∼5 m s^{-1} would take approximately ∼3 min. This is much longer than indicated by the relative timing of infrasound explosion signals (modal delay time of 4.5 s between seismic VLP onset and peak infrasonic amplitude) when they are present (e.g. Figs 9c, 11 and 17). The observed time-delays between VLP onset and infrasound explosions (when present) (Fig. 11) imply implausibly high slug ascent velocities of hundreds of meters per second (Harris & Ripepe 2007; Jolly *et al.* 2018; Ishii *et al.* 2019) (discussed further in Section 5.3). Thus, scenario one is implausible and can be rejected.

Alternatively (scenario two), the VLP source at ∼900–1000 m depth may be connected to surficial explosions and infrasound through dynamic stress propagation or pressure wave (i.e. a crack wave or Stoneley wave through the conduit; Chouet 1988; Kumagai & Chouet 2000). Computational fluid dynamic simulations of the final ascent stage of a gas slug in a liquid-filled vertical cylindrical conduit (closed at the base) (James *et al.* 2008; Chouet *et al.* 2010) show that, during most of the slug ascent, the total force on the tube does not change significantly because upward and downward forces are delicately balanced. However, upon slug burst, the rapid dynamics deviate from this balance and a net transient upward force is exerted at the tube base with both shear and pressure components (Chouet *et al.* 2010). This scenario is consistent with the dominant features of our derived source–time-functions (Figs 14 and 17) for both the crack volume changes (deflation beginning at ∼9.5 s in the Crack 1 source waveform, Fig. 17) and the corresponding vertical single-force component (upward force) in the mechanism. Thus, in the case of VLPs accompanied by large surficial explosions and infrasound, dynamic stress and pressure disturbances propagating down through the intermediate magma system (Fig. 16) down to the VLP centroid depth ∼900–1000 m offer a partial explanation for the observations. This top-down model (Patrick *et al.* 2011) explains well the major VLP source-waveform features of a volume change and vertical force imaged at the source centroid in addition to the timing with infrasound and surficial explosions (when present) (see Section 5.3).

5.2 Decoupling and desynchronization of VLPs from surficial explosions and infrasound

The decoupling and desynchronization of the dominant VLPs at ∼900–1000 m depth from surficial explosions and infrasound could be explained in several ways. Taken together, our infrasound and seismic observations imply a buffering effect on the terminal ascent of the slug (shallow section, Figs 16b and c). The connection between seismic VLPs at depth and surficial eruptive activity and infrasound may be modulated by a variety of conditions at or directly beneath the vents in this shallow zone, such as a high-viscosity layer (HVL) or crystal-rich degassed plug of magma (Gurioli *et al.* 2014; Del Bello *et al.* 2015; Gaudin *et al.* 2017; Capponi *et al.* 2017; Oppenheimer *et al.* 2020), the level of backfill and corresponding muffling by this rubble or debris cap (Patrick *et al.* 2007; Simons *et al.* 2020a), or a near-surface zone characterized by fracturing and sintering breccia plugs, for example a vertically extensive messy magma breccia pipe (Schipper *et al.* 2021). If the interval between explosions is long enough, partial solidification of near-surface magma may occur, or the vent may fill with debris, both with similar effects on the near-surface slug dynamics. Another relatively simple possibility for muting the explosive release of gas is a near-surface layer of foam, with or without the presence of crystals (Garces *et al.* 1998; Weaire & Hutzler 1999; Koehler *et al.* 2000; Hilgenfeldt *et al.* 2008; Chouet & Dawson 2015; Spina *et al.* 2016a). An HVL that is rubble-driven and a foam layer are not mutually exclusive, as the HVL could be a rubbly foamy breccia (scoria recycled into magma); observed vesicularity of bombs and scoria during the field campaign supports the existence of a foam.

Over a timescale of a few days, we observe a gradual progression in VLP seismic decoupling and reconnection with surficial explosions, infrasound, and high-frequency seismic phase (Section 3, Figs 10 and 11). This timescale is generally consistent with the temporary formation of a crystal-rich degassed plug (or foamy HVL) through partial solidification of near-surface magma (shallow buffer zone sealed by 07:40:49, 29 July 2016) and its subsequent reopening via increased explosive activity which excavates a path through or destroys this buffer (Simons *et al.* 2020b); this is achieved by 09:54:10, 31 July 2016 UT when high-amplitude infrasound reappears in direct association with the VLPs (Fig. 11). Thus, the shallow buffer is an ephemeral feature that is liberated after some pressure build-up.

Recent analogue laboratory experiments by Oppenheimer *et al.* (2020) provide initial insight on the relevant dynamics of slug ascent in the presence of a 'weak plug'. Their experiments considered large bubbles rising in a vertical tube (idealized vertical conduit) filled with silicone oil and polypropylene particles as an analogue to strombolian slug flow for a crystal-rich magma with high crystallinity approaching the eruptibility limit for magma. The experiments of Oppenheimer *et al.* (2020) did not include pressure and force sensors in the tube (*cf.* James *et al.* 2006, 2008; Del Bello *et al.* 2015) and thus do not provide a quantification of possible VLP mechanisms when a slug encounters the crystal-rich layer. Nevertheless, the experiments provide insight into a range of first-order effects such as single slugs transiting quickly, slugs being pinned to the edge of the conduit, or slugs breaking up or stalling.

A temporary physical barrier such as a crystal-rich plug (or foamy HVL) in the shallow buffer region may trap the slug below or within the plug (Oppenheimer *et al.* 2020) and provides an explanation for the observation of seismic VLPs without infrasound. Similarly, the minor spattering activity we observe associated with some of the VLPs (Figs 9b, Supporting Information Movie M3) may be related to situations in which slug expansion in the liquid below the plug can cause the slug to migrate as a finger pinned along one side of the conduit wall (Oppenheimer *et al.* 2020). In this situation, slug burst occurs at the side of the conduit and is often accompanied by spattering. Slugs may also travel through the cap separated into several pieces (dissipated into smaller gas volumes), which would be expected to lead to a succession of smaller bursts at the surface (Oppenheimer *et al.* 2020). Supporting this interpretation, in Fig. 10, we also observe progressive lengthening of infrasound signal durations prior to the sealing of the shallow buffer zone (events ∼0–110, prior to 07:40:49, 29 July 2016) and abrupt shortening of infrasound signal durations once the shallow section has reopened (events >397, beginning at 09:54:10, 31 July 2016 UT).

We note, however, that the preferred dual-crack composite solution (Fig. 14, Section 4.2) does not include a geometrical component that leads to the summit vents (the pipe-crack solution has the pipe dipping 34° from vertical). Thus, based on the VLP waveform inversion results, we do not have a clear picture for how the magmatic system transitions from depth to the surface summit vents. Since the derived VLP source-centroid is directly beneath the summit vents and clearly connected to the surficial activity, an implication is that there must be an intermediate depth range in the conduit system that is relatively aseismic or at least not well captured by our single point-source approximation applied to the dominant VLP multiplet (intermediate section, Fig. 16).

During our field campaign, Yasur was erupting from multiple vents (Sections 3.5 and 3.7; Jolly *et al.* 2017; Iezzi *et al.* 2019; Fitzgerald *et al.* 2020; Fee *et al.* 2021), adding greater complexity to the dynamics of the shallow buffer region that could be investigated further in future work through a more systematic analysis of the infrasound data (e.g. more comprehensive infrasound signal discrimination and source localization). In particular, the transition from weak to strong infrasound with increase in eruption intensity (opening up of the shallow section; Figs 10 and 11) also corresponds to a general shift from activity at North Crater to increased explosive activity at South Crater (Jolly *et al.* 2017; Fitzgerald *et al.* 2020). However, as shown in Section 3.7 (Fig. 12), the infrasound signals associated with the dominant seismic VLPs have a more complex spatio-temporal evolution. The initial transition into diminished infrasound amplitudes at 07:40:49, 29 July 2016 corresponds with an abrupt shift in acoustic source locations from South to North Craters, which is maintained until approximately 19:12 29 July 2016 UT; subsequently, weak acoustic signals localize to both South and North crater vents, and the transition back to powerful infrasound beginning at 09:54:10, 31 July 2016 UT is largely localized to the South crater.

It is important to note that infrasound sources did not completely shut down at Yasur even during the time when the dominant seismic VLP multiplet was not immediately associated with surficial explosions and large-amplitude infrasound (see Fig. 4). During the times between 07:40:49, 29 July 2016 and 09:54:10, 31 July 2016 UT when high-amplitude infrasound is not immediately associated with seismic VLPs, infrasound signal amplitudes are significantly lower overall across the network (Fig. 6), but low-level infrasound activity continues (localized to both South and North craters, Fig. 12b). Thus, the lid was not completely sealed in the shallow buffer zone and gas found a way to the surface, but erupted with lower vigour. The vent flaming and spattering activity captured in Supporting Information Movie M2 are presumably representative of this behaviour.

The multiple active vents and bifurcated summit with North and South Craters (Simons *et al.* 2020b) are major surface features

of Yasur during our field experiment. Within the shallow feeding system beneath the multiple summit vents, the idea of individual vertical pipes extending down to a magma storage reservoir is likely an oversimplification. The shallow structure is more likely dominated by dikes, and a shallow planar volume would provide a more viable path for distributing gas to the various vents, as well as room to buffer or accommodate gas without strong venting. Overall, our observations indicate temporary clogging and sealing, then reopening, of elements of these multiple branching pathways within the shallow feeding system beneath the summit.

5.3 VLP and infrasound relative timing

Based on relative VLP and infrasound timing considerations alone (raw time-delays ∼4.5 s not accounting for wave propagation time, Fig. 11), a variety of interpretations are possible. For example, a VLP at depth followed this rapidly by surficial explosion and infrasound could be explained in a 'bottom-up' model by rapid gas ascent via annular flow (Ishii *et al.* 2019), fracture propagation in magma (if relatively high-viscosity) (Lavallée *et al.* 2008; Cordonnier *et al.* 2012), or a fragmentation front and upward pressure transient (Scheu *et al.* 2006). However, here we show that a shallow-buffered top-down model as outlined in Fig. 16 is also compatible with the time-delay observations (Figs 11, 17 and 18), and is further supported through quantitative considerations of the derived VLP source mechanism (Section 5.1).

We consider a shallow-buffered top-down model in which the slug ascends the intermediate conduit section relatively aseismically until it reaches the base of the shallow buffer section (Figs 16 and 18). Slug disruption in this shallow zone triggers a pressure disturbance that propagates downward at the speed of the crack wave (Chouet 1988; Kumagai & Chouet 2000) and couples at the geometrical discontinuity at the base of the conduit (the location of the VLP centroid) (Fig. 18). What happens in the shallow terminal zone depends upon the prevailing rheological conditions in this zone (Section 5.2). If the shallow section is partially or entirely sealed, the slug is trapped or splits up into several components and weak or no infrasound is produced (Fig. 16b). If the shallow section is open, the slug bursts and an explosion propagates to the surface, producing a powerful infrasound signal (Fig. 16c).

We investigate the relative arrival times of seismic VLP and associated infrasound (when present) to first-order using a simplified geometry and propagation assumptions (Fig. 18). Fig. 17 defines the various reference times in the VLP seismic and infrasound waveforms. The basic feature of our interpretation (Fig. 18) is that slug disruption in the shallow zone is not instantaneous and there is some time-delay between a slug first encountering the base of the shallow zone, its explosive burst, and the subsequent propagation of the explosion front through the shallow section to the surface to form an explosive eruption; i.e., explosive fragmentation through the partially sealed HVL (Scheu *et al.* 2006; Lavallée *et al.* 2008; Cordonnier *et al.* 2012). Infrasound, if present, is produced at or immediately above the vent in direct association with surficial explosive eruption into the atmosphere. Our video data, such as those presented in Supporting Information Movies M1–M4, strongly support the interpretation that the explosion infrasound signals are produced at the vent by surface explosive eruption rather than at depth in the conduit below the surface (e.g. Ripepe *et al.* 2001; Ruiz *et al.* 2006; Iezzi *et al.* 2020).

This complexity is captured by stating simply that the absolute time t_{explo} of the surface explosion (and thus the infrasound source origin time) is given by:

$$t_{\text{explo}} = t_{\text{entry}} + T_B, \tag{1}$$

where t_{entry} is the absolute time of entry of the slug into the base of the shallow section and the 'buffer time' T_B is a finite response time in seconds of the shallow buffer section. The buffer time T_B includes all finite-duration effects of slug expansion, slug burst, and propagation of the explosion front through the shallow section. For example, laboratory experiments indicate that slug arrival in the shallow zone is characterized by slug expansion until slug burst as the slug begins to be influenced by the decreasing magmastatic head in the upper part of the conduit. As the slug rises and expands, an increasing amount of liquid is supported by the wall along the slug (James *et al.* 2008, 2009; Del Bello *et al.* 2015). This induces a decrease in the magmastatic head at the VLP source location (at the base of the intermediate section), which results in an upward force and accompanying deflation of the dominant crack in our source model (Figs 14b and 17). Thus, the VLP source process begins prior to the slug burst.

With the VLP source centroid at depth z_S ∼900 m below topography (Fig. 18), the pressure disturbance propagates downward at the speed v_M of the inhomogeneous crack wave; it takes time $T_M \sim z_M/v_M$ for the pressure disturbance to propagate through the magma from the shallow triggering event (at the base of the buffer region, depth z_B) to reach the VLP centroid location (with z_M the length of the intermediate section; $z_M = z_S - z_B$). The VLP source is then activated and radiates a signal that propagates toward the receiver at the speed of the compressional wave in the solid $V_p \sim$ 2400 m s^{-1}, resulting in an approximate seismic propagation traveltime T_S of 0.5 s to the collocated seismic and infrasonic station YS01 and YIB22 (Fig. 18) (radial distance 630 m, station elevation 272 m above sea level).

Under these assumptions, the absolute arrival time of the seismic VLP first-onset t_{Vonset} at station YS01 relates to the absolute time of slug entry into the base of the shallow section t_{entry} by:

$$t_{\text{Vonset}} = t_{\text{entry}} + T_M + T_S. \tag{2}$$

For the infrasound signal, the source origin time is the time of the surficial explosion t_{explo} and the acoustic propagation time from source to receiver is T_A (Fig. 18). We compute the acoustic propagation time T_A using finite-differences as described and parametrized by Iezzi *et al.* (2019), taking into account the topography (resampled to a 2-meter grid spacing) and an adiabatic (windless) static sound speed of 346.4 m s^{-1}, corresponding to an air temperature of ∼30 °C. The computed traveltimes T_A are 2.02 and 2.39 s, for South and North Crater vents, respectively to the collocated station YIB22 and YS01. At this recording range (630 m), topography (i.e. diffraction from vent over crater wall to receiver) is the dominant factor influencing infrasonic traveltime (Iezzi *et al.* 2020; Fee *et al.* 2021). For example, an upper bound 10 m s^{-1} wind speed during the experiment (Jolly *et al.* 2017; Iezzi *et al.* 2019) would result in acoustic traveltime variations on the order of not more than ∼0.1 s (estimated from a 10 m s^{-1} upwind versus downwind influence on an effective sound speed).

Given the estimate of T_A, the absolute arrival time t_{inf} of the infrasound signal at YIB22 and YS01 is thus:

$$t_{\text{inf}} = t_{\text{explo}} + T_A \tag{3}$$

$$= t_{\text{entry}} + T_B + T_A. \tag{4}$$

The observed time-delay δt between the VLP first-onset t_{Vonset} and the infrasound pulse arrival t_{inf} is given by:

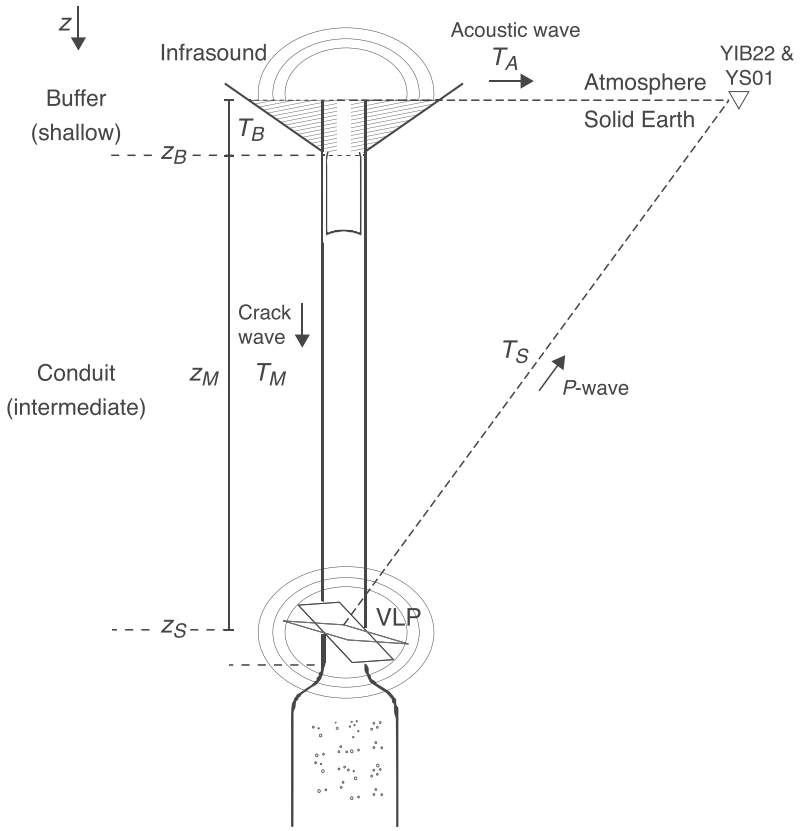

Figure 18. Geometry of the shallow-buffered top-down model used to interpret the observed time-delays (at collocated seismic station YS01 and infrasound station YIB22) between the onset of the seismic VLP and the infrasound pulse arrival. The VLP source centroid lies at depth z_S below the summit vents. z_B is the depth (thickness) of the shallow buffer section, $z_M = z_S - z_B$ is the length of the intermediate magma transport section traversed by the crack wave in time T_M in communicating the pressure disturbance at the base of the shallow section to the VLP centroid. T_A is the acoustic wave propagation time in the atmosphere from vent to station and T_S is the seismic propagation time from the VLP centroid to the seismic station. T_B is the buffer response time in the shallow section including all finite-duration effects of slug expansion, slug burst, and propagation of the fragmentation front through the partially sealed high-viscosity layer.

$$\delta t = t_{\text{inf}} - t_{\text{Vonset}} \tag{5}$$

$$= T_B + T_A - T_M - T_S. \tag{6}$$

In Section 3.6.2, we found the modal delay time $\delta t \sim 4.5$ s. Combined with the above first-order estimates for $T_S \sim 0.5$ s and $T_A \sim 2.02$ s (South Crater), yields $T_B - T_M = 2.98$ s. To place constraints on plausible T_M, in Appendix B we investigate various estimates of the crack-wave velocity v_M. As a limit, the crack-wave velocity cannot be higher than the acoustic speed ($\sim$2000 m s^{-1}) of the liquid basalt. For a lower mode such as $m = 2$ with a wavelength of 800 meters, the crack-wave velocity is expected to be no more than a few hundred meters per second. For example, for the lowest $m = 2$ mode with crack stiffness $C = 50$ and frequency $f_2 = 0.320$ Hz, the crack-wave velocity v_M is 256 m s^{-1}. Or with $C = 10$, $f_2 = 0.638$ Hz, v_M is 510 m s^{-1}. Assuming a shallow buffer region of thickness $z_B \sim 100$ m; gives $T_M \sim z_M/v_M = 800/256 \sim 3.1$ s or alternatively $T_M \sim 800/510 \sim 1.6$ s, for these illustrative crack-wave speeds, respectively. These estimates result in values of $T_B \sim 5$–6 s for the buffer time in the shallow section including all finite-duration effects of slug expansion, slug burst, and propagation of the fragmentation front through the partially sealed HVL. In Section 3.6.2, we found variability in the time-delays δt on the order of up to an additional $\sim$2 s; this variability is attributed to variable duration buffering in the shallow section (and $\sim$+0.4 s delay-time would be expected for an infrasound signal from North Crater propagating the greater distance to YIB22 compared to South Crater).

The above estimates are illustrative to demonstrate feasibility. It is beyond the scope to identify the precise timing of slug burst within the observed VLP waveform features (or the derived VLP source–time-functions). However, we further note that the time-duration in the seismic waveform (in both the observed waveforms and the derived Crack 1 source–time-function) between the initial volumetric VLP onset (downward first motion) and the first positive pulse peak in the VLP waveform is $\sim$3.5 s (i.e. 3.5 s from the initial VLP onset to the beginning of the dominant Crack 1 deflation discussed in Section 5.1), consistent with accounting for a portion of the inferred range for T_B above.

Our shallow-buffered top-down model is therefore compatible with the VLP and infrasound time-delay observations as well as the derived VLP source–time histories (Section 5.1). The alternative bottom-up model with annular flow, fracture propagation, or fragmentation front in the intermediate section (Ishii *et al.* 2019) is unlikely to provide a realistic explanation for the source–time histories of volume change and single force we have imaged at Yasur (Section 5.1). In addition, the inferred slug formation depth

of ∼1.5 km and 900 m depth beneath Yasur (based on water exsolution) is immediately below the VLP centroid (∼900–1000 m depth). This renders unlikely the scenario of a high-speed slug passing through a constriction at the VLP centroid as the (bottom-up) causative mechanism of the VLP. An energetic foam collapse at the VLP centroid (Ripepe *et al.* 2001; Ishii *et al.* 2019) as the driver of the VLP is also unlikely based on the high-rate nature of repetitive VLP occurrence reported here (short-interevent times ∼20 to 60 s).

5.4 Source volume change, dimension, and force balance

For the preferred dual-crack source (Fig. 14b), the scalar magnitude F of the single-force vector based on the maximum peak-to-peak amplitudes of the three-components of force-time history is ∼6.9 × 10^{10} N and the maximum peak-to-peak amplitude of the volume change ΔV is ∼540 m^3 in the dominant Crack 1 (Fig. 17). Assuming a penny-shaped crack, pressure change ΔP is (Sneddon & Lowengrub 1969):

$$\Delta P = \frac{3}{4}\frac{\mu(\lambda+\mu)}{\lambda+2\mu}\left(\frac{\Delta V}{a^3}\right), \tag{7}$$

where λ and μ are the Lamé coefficients of the solid, a is the crack radius, and ΔV is the volume change in the crack. Assuming that the force vector is aligned with the surface normal of the dominant Crack 1 plane (see Table 2) and assuming $\lambda = 2\mu$ (hot rock), yields:

$$\Delta P = \frac{9\mu}{16}\left(\frac{\Delta V}{a^3}\right) = \frac{F}{\pi a^2}, \tag{8}$$

$$a = \frac{9\pi\mu}{16}\frac{\Delta V}{F}. \tag{9}$$

Assuming a shear modulus μ = 10 GPa, the maximum peak-to-peak values of F and ΔV result in a crack radius a ∼139 m and area of the dominant Crack 1 ∼60 000 m^2.

According to our interpretation, the changes in vertical pressure force exerted by the liquid on the base of the intermediate transport section (Fig. 16) reflect decreasing static pressures below the slug. As the slug ascends and expands, viscous shear along the wall-rock provides support for an increasing mass of liquid. Consequently, the static pressure below the slug decreases, reducing the downward pressure force coupling at the upward facing base of the intermediate section (i.e. effectively producing an upward force). We can estimate the basal pressure drop ΔP assuming a cylindrical conduit and using some realistic values for the conduit diameter $D = 5$ m, together with a liquid density $\rho_l = 2500$ kg m^{-3}, and liquid viscosity $\eta = 500$ Pa s. Brown (1965) gave an equation for the equilibrium thickness, δ_0, of the liquid film that is present over the entire length of a gas slug ascending a vertical tube:

$$\delta_0 = \frac{(-1+\sqrt{1+ND})}{N}, \tag{10}$$

where

$$N = \sqrt[3]{14.5\frac{\rho_l^2 g}{\eta^2}}. \tag{11}$$

With $g = 9.81$ m s^{-2}, $\rho_l = 2500$ kg m^{-3}, $\eta = 500$ Pa s, and $D = 5$ m, we obtain $N = 15.26367$ and $\delta_0 = 0.51$ m.

Assuming a slug length H = 100 m yields the volume of liquid hanging on the conduit wall, $V_l = \pi D\delta_0 H \sim 802$ m^3. This volume represents a mass $m_l = V_l\rho_l$ of 802 × 2500 = 2 × 10^6 kg, yielding a pressure drop $\Delta P = m_l g/[\pi(D/2)^2] \sim (2\times10^7)/(\pi 2.5^2) \sim 1$ MPa. Accordingly, the source region experiences a substatic pressure of ∼1 MPa. Applying this ΔP to our penny-shaped crack and using our estimated volume change in the crack, $\Delta V \sim 540$ m^3, together with a shear modulus μ = 10 GPa, we obtain the crack radius, a, as

$$a = \sqrt[3]{\frac{9\mu}{16}\frac{\Delta V}{\Delta P}}, \tag{12}$$

from which we obtain $a \sim 145$ m, representing an area of Crack 1 ∼ 65 890 m^2, in agreement with the values obtained above. The volume of the cylindrical slug with height H = 100 m and radius of ∼2 m is ∼1244 m^3.

In this analysis, the fluid involved in producing the volume change of 540 m^3 is the liquid hanging on the wall alongside a slug with volume of ∼1244 m^3. These values only represent first-order estimates given our lack of knowledge of the actual in situ viscosity and conduit size and geometry. We emphasize that the volume change of 540 m^3 is derived from inverting the multiplet stack with amplitude scaled by the seed event, which is the largest amplitude VLP in the data set (Section 3.3.4). Implied volume changes for other smaller VLP events in the multiplet are lower, scaled linearly with observed waveform amplitude (same source location assumed for events in the multiplet) (Matoza & Chouet 2010).

5.5 Limitations and future work

The profusion of VLPs occurring at a high rate (repetitive VLP seismic events reoccurring near-continuously throughout the data set with short but variable inter-event times ∼20 to 60 s) reflects a high gas supply (Nairn *et al.* 1988; Oppenheimer *et al.* 2006; Métrich *et al.* 2011) coupled with low magma viscosity. Scoria samples collected during our field campaign (collected at the same time that these seismic and infrasound data were recorded) had very low microlite content, consistent with low-viscosity magma. However, our limited temporal sampling of the scoria precludes a more quantitative investigation of the link between magma viscosity, crystallinity, and variable seismo-acoustic source syncronization. Higher temporal sampling of eruptive products could test these hypotheses.

We have presented waveform inversion results for the dominant VLP multiplet observed during our field campaign. Additional significant VLP and LP signals present in the data do not fall into this dominant multiplet, and future work expanded to include other VLP multiplets or LP period bands (see Section 3.6.1, Fig. 10e) may be able to capture more of the seismic source complexity. We note, for example, that the event highlighted in Figs 2 and Supporting Information Movies M1 and M2 does not belong to the dominant VLP multiplet. This event (Figs 2, Movies M1 and M2) has a high-amplitude and long-duration oscillatory VLP that precedes and accompanies a powerful explosion, high-amplitude infrasound and associated high-frequency seismic signature, and a clear visible shock wave or 'flashing arc' (Perret 1950; Austin *et al.* 2017). We attempted a seismic VLP waveform inversion for this event, but a stable solution could not be obtained using the methods presented here. This may partially reflect signal contamination from air-to-ground coupling (e.g. Matoza *et al.* 2019b) of the infrasound explosion signature into the seismic waveforms for this particular event (Fig. 2). Alternatively or additionally, this VLP event (Fig. 2) may represent a shallower event with a VLP source mechanism arising from disruption of a larger distributed shallow magma source (e.g. foam collapse in a shallow magma volume immediately beneath the summit). Such a large shallow distributed source would not be adequately captured by our single point-source approximation. Future field campaigns at Yasur using a greater station density could

improve knowledge of the shallow velocity structure and in tandem may permit multiple point-source or distributed finite-source inversions that would be needed to capture such source complexity.

We have largely restricted the analysis of infrasound signals to those directly associated with the dominant VLP seismic multiplet. However, this represents only a small subset of the infrasound signals recorded during the experiment (Fig. 6) (Matoza *et al.* 2017; Jolly *et al.* 2017; Iezzi *et al.* 2019; Fee *et al.* 2021). More comprehensive infrasound signal discrimination, source localization, and waveform inversion will better track the spatio-temporal evolution of the explosions, degassing, and role of multiple vents, better characterizing the spatio-temporal fate of gas buffered in the shallow zone.

6 CONCLUSIONS

Our seismo-acoustic campaign deployment (from 2016 July 27 to August 3) captures a brief snapshot of Yasur's remarkably persistent and long-lived eruptive activity, but enables a quantitative window into the seismo-acoustic source mechanics at this continuously active open-vent basaltic-andesite volcano. We observe strong variability in the synchronization of seismic and acoustic sources, with a systematic progression in VLP seismic decoupling and reconnection with surficial explosions and infrasound over a timescale of a few days during our field campaign. UAS video imaging demonstrates that low-amplitude infrasonic tremor signal associated with some VLP seismic events in the dominant multiplet is related to gas-rich spattering and vent 'flaming' activity. Full-waveform inversion of the dominant VLP multiplet stack points to a composite source consisting of either a dual-crack (plus forces) or pipe-crack (plus forces) mechanism. The derived mechanisms correspond to a point-source directly beneath the summit vents with centroid depths in the range ∼900–1000 m below topography and ∼700–800 m below sea level. All mechanisms suggest a northeast trending crack dipping relatively shallowly to the northwest and indicate a VLP source centroid and mechanism controlled by a stable structural geologic feature beneath Yasur that is part of the plumbing system that feeds the surficial activity.

The seismo-acoustic observations are consistent with a variously shallow-buffered top-down model in which a gas slug ascends a conduit relatively aseismically until it reaches a shallow section. Slug disruption in this shallow zone triggers a pressure disturbance that propagates downward at the speed of the crack wave and couples at the geometrical discontinuity at the base of the conduit (the location of the VLP centroid), producing a VLP. If the shallow section is relatively open, an explosion propagates to the surface, producing infrasound. This shallow-buffered top-down model explains the major VLP source-waveform features and mechanism, in addition to the relative timing with infrasound signals (when present). The decoupling and desynchronization of the dominant VLPs at ∼900–1000 m depth from surficial explosions and infrasound strongly indicates an enhanced buffering of the terminal slug ascent. This buffering between seismic VLPs at depth and surficial eruptive activity and infrasound may be accomplished through a variety of conditions at or directly beneath the vents, such as a high-viscosity layer of crystal-rich magma, a debris cap from backfill, a foam layer, or a combination of these. The dominant VLP at Yasur captured by our experiment has a source depth and mechanism separated from surface processes and is stable over time.

ACKNOWLEDGMENTS

This work was supported by NSF grants EAR-1847736 and EAR-1620576 to Matoza, with seed funds provided by a UC Regents Junior Faculty fellowship to RSM. ADJ and GNK were funded by the New Zealand Ministry of Business, Innovation, and Employment (MBIE) for the field campaign. RHF acknowledges funding from the New Zealand Earthquake Commission (EQC) biennial grant (16/727) and a Ngāi Tahu Research Centre Doctoral Scholarship. BMK acknowledges MBIE RNC2 volcano theme for funding support. DF acknowledges funding from NSF EAR-1901614. AMI acknowledges funding from NSF EAR-PF-1952392. We thank Simon Bloomberg for providing some of the digitized lineations used in Fig. 1. The workflows included use of ObsPy (Beyreuther *et al.* 2010; Krischer *et al.* 2015), QGIS, and GMT (Wessel & Smith 1991). We thank Michael Colee, Aaron Martin, and Darla Sharp at the Earth Research Institute, University of California, Santa Barbara for providing and maintaining the high-performance computing (HPC) systems used in this study. We thank Philippe Lesage and John Lyons for manuscript review. Any use of trade, firm, or product names is for descriptive purposes only and does not imply endorsement by the U.S. Government.

AUTHOR CONTRIBUTIONS

Matoza performed all of the seismic and infrasonic data analyses and inversions (except RTM-FDTD acoustic source location), produced all of the figures and supplementary materials, and conceived and wrote the paper. Matoza performed the VLP waveform inversions and VLP source mechanism analyses in collaboration with Chouet and Dawson. Matoza analysed the video data (as presented here) and produced the supplementary movies in consultation with Fitzgerald and Kennedy. Fee performed the infrasound source locations based on the event catalogue provided by Matoza. Iezzi performed the infrasound wave propagation simulation. The field experiment was conceived and organized by Matoza, Jolly, Fee, Kennedy, and Garaebiti. Seismic and acoustic instrumentation prepared and deployed by Matoza, Fee, Iezzi, and Jolly. Field video data collection, processing, and cataloguing by Fitzgerald and Kennedy. Eruption products collected and analysed by Kilgour. All authors discussed the results and interpretations and provided input at various stages in the research progression. All authors provided comments on and approved the manuscript.

For their assistance in the field, we acknowledge Nick Key (video and UAS data collection), Adrien Tessier (video data collection), Allison Austin (seismic, acoustic, video data collection), Richard Johnson (seismic and acoustic data collection), Janvion Cevuard (seismic and acoustic data collection), Athanase Worwor (seismic and acoustic data collection) and Julius Mala (seismic and acoustic data collection).

DATA AVAILABILITY STATEMENT

Infrasound waveform data are available at the IRIS Data Management Center (DMC) with temporary FDSN network code 3E (Fee *et al.* 2016b). Seismic data will be made available at the IRIS DMC in future. Supplementary Movies (video data) are available in the accompanying Dryad data repository (Matoza et al. 2021).

REFERENCES

Akaike, H., 1974. A new look at the statistical model identification, *IEEE Trans. Autom. Control,* **AC-9,** 716–723.

Allen, S.R., 2004. Complex spatter- and pumice-rich pyroclastic deposits from an andesitic caldera-forming eruption: the Siwi pyroclastic sequence, Tanna, Vanuatu, *Bull. Volcanol.,* **67,** 27–41.

Antier, K., Le Pichon, A., Vergniolle, S., Zielinski, C. & Lardy, M., 2007. Multiyear validation of the NRL-G2S wind fields using infrasound from Yasur, *J. Geophys. Res.,* **112,** D23110.

Arciniega–Ceballos, A., Dawson, P. & Chouet, B.A., 2012. Long period seismic source characterization at Popocatépetl volcano, Mexico, *Geophys. Res. Lett.,* **39,** L20307.

Auger, E., D'Auria, L., Martini, M., Chouet, B. & Dawson, P., 2006. Real-time monitoring and massive inversion of source parameters of very long period seismic signals: an application to Stromboli Volcano, Italy, *Geophys. Res. Lett.,* **33,** L04301.

Austin, A.K. *et al.*, 2017. Flashing arcs at Yasur Volcano, Vanuatu and their relationship to strombolian eruption mechanics, International Association of Volcanology and Chemistry of the Earth's Interior (IAVCEI) Scientific Assembly, Portland, OR.

Bani, P., Oppenheimer, C., Allard, P., Shinohara, S., Tsanev, V., Carn, S., Lardy, M. & Garaebiti, E., 2012. First estimate of volcanic SO_2 budget for Vanuatu island arc, *J. Volc. Geotherm. Res.,* **211–212,** 36–46.

Bani, P., Harris, A.J.L., Shinohara, H. & Donnadieu, F., 2013. Magma dynamics feeding Yasur's explosive activity observed using thermal infrared remote sensing, *Geophys. Res. Lett.,* **40,** 3830–3835.

Battaglia, J., Métaxian, J.-P. & Garaebiti, E., 2012. Earthquake-volcano interaction imaged by coda wave interferometry, *Geophys. Res. Lett.,* **39,** L11309.

Battaglia, J., Métaxian, J.-P. & Garaebiti, E., 2013. Short term precursors of Strombolian explosions at Yasur volcano (Vanuatu), *Geophys. Res. Lett.,* **43,** 1960–1965.

Battaglia, J., Métaxian, J.-P. & Garaebiti, E., 2016. Families of similar events and modes of oscillation of the conduit at Yasur volcano (Vanuatu), *J. Volc. Geotherm. Res.,* **322,** 196–211.

Beyreuther, M., Barsch, R., Krischer, L., Megies, T., Behr, Y. & Wassermann, J., 2010. ObsPy: a Python toolbox for seismology, *Seismol. Res. Lett.,* **81**(3), 530–533.

Brothelande, E. *et al.*, 2016a. Structure and evolution of an active resurgent dome evidenced by geophysical investigations: The Yenkahe dome-Yasur volcano system (Siwi caldera, Vanuatu), *J. Volc. Geotherm. Res.,* **322,** 241–262.

Brothelande, E. *et al.*, 2016b. Insights into the evolution of the Yenkahe resurgent dome (Siwi caldera, Tanna Island, Vanuatu) inferred from aerial high-resolution photogrammetry, *J. Volc. Geotherm. Res.,* **322,** 212–224.

Brown, R.A.S., 1965. The mechanics of large gas bubbles in tubes: I. Bubble velocities in stagnant liquids, *Can. J. Chem. Eng.,* **43,** 217–223.

Bueno, A., Diaz-Moreno, A., Álvarez, I., De la Torre, A., Lamb, O.D., Zuccarello, L. & De Angelis, S., 2019. VINEDA–Volcanic INfrasound Explosions Detector Algorithm, *Front. Earth Sci.,* **7,** 335.

Capponi, A., Lane, S.J. & James, M.R., 2017. The implications of gas slug ascent in a stratified magma for acoustic and ground deformation source mechanisms in Strombolian eruptions, *Earth Planet. Sci. Lett.,* **468,** 101–111.

Carney, J.N. & McFarlane, A., 1979. Geology of Tanna, Aneityum, Futuna and Aniwa, *New Hebrides Government Geol. Surv.,* 5–29.

Chen, J.K., Taylor, F.W., Edwards, R.L., Cheng, H. & Burr, G.S., 1995. Recent emerged reef terraces of the Yenkahe resurgent block, Tanna, Vanuatu: implications for volcanic, landslide and tsunami hazards, *J. Geol.,* **103**(5), 577–590.

Chouet, B., 1988. Resonance of a fluid-driven crack: radiation properties and implications for the source of long-period events and harmonic tremor, *J. geophys. Res.,* **93,** 4375–4400.

Chouet, B. & Dawson, P., 2013. Very long period conduit oscillations induced by rockfalls at Kilauea Volcano, Hawaii, *J. geophys. Res.,* **118,** 5352–5371.

Chouet, B. & Dawson, P., 2015. Seismic source dynamics of gas-piston activity at Kilauea Volcano, Hawai'i, *J. geophys. Res.,* **120,** 2525–2560.

Chouet, B. *et al.*, 2003. Source mechanisms of explosions at Stromboli Volcano, Italy, determined from moment tensor inversions of very-long-period data, *J. geophys. Res.,* **108,** 2019.

Chouet, B., Dawson, P. & Arciniega-Ceballos, A., 2005. Source mechanism of Vulcanian degassing at Popocatepetl Volcano, Mexico, determined from waveform inversions of very long period signals, *J. geophys. Res.,* **110,** B070301.

Chouet, B., Dawson, P. & Martini, M., 2008. Shallow-conduit dynamics at Stromboli Volcano, Italy, imaged from waveform inversions, in *Fluid Motions in Volcanic Conduits: A Source of Seismic and Acoustic Signals,* Vol. 307, pp. 57–84, eds Lane, S.J. & Gilbert, J.S., Geological Society, London, Special Publications.

Chouet, B.A., 1996. New methods and future trends in seismological volcano monitoring, in *Volcanic Seismology: IAVCEI Proceedings in Volcanology 3,* pp. 23–97, eds Scarpa, R. & Tilling, R., Springer.

Chouet, B.A. & Dawson, P.B., 2011. Shallow conduit system at Kilauea Volcano, Hawaii, revealed by seismic signals associated with degassing bursts, *J. geophys. Res.,* **116,** B12317.

Chouet, B.A. & Matoza, R.S., 2013. A multi-decadal view of seismic methods for detecting precursors of magma movement and eruption, *J. Volc. Geotherm. Res.,* **252,** 108–175.

Chouet, B.A., Dawson, P.B., James, M.R. & Lane, S.J., 2010. Seismic source mechanism of degassing bursts at Kilauea Volcano, Hawaii: Results from waveform inversion in the 10–50 s band, *J. geophys. Res.,* **115,** B09311.

Coffin, M.F., Gahagan, L.M. & Lawver, L.A., 1998. Present-day plate boundary digital data compilation, University of Texas Institute for Geophysics Technical Report No. 174.

Cordonnier, B. *et al.*, 2012. The viscous-brittle transition of crystal-bearing silicic melt: direct observation of magma rupture and healing, *Geology,* **40,** 611–614.

Dawson, P.B. & Chouet, B.A., 2019. Long period seismicity at Mammoth Mountain, *J. geophys. Res.,* **124,** 6751–6778.

Dawson, P.B., Chouet, B.A. & Power, J., 2011. Determining the seismic source mechanism and location for an explosive eruption with limited observational data: Augustine Volcano, Alaska, *Geophys. Res. Lett.,* **38,** L03302.

Del Bello, E., Lane, S.J., James, M.R., Llewellin, E.W., Taddeucci, J., Scarlato, P. & Capponi, A., 2015. Viscous plugging can enhance and modulate explosivity of strombolian eruptions, *Earth planet. Sci. Lett.,* **423,** 210–218.

Duarte, M. & Watanabe, R.N., 2018. Notes on scientific computing for biomechanics and motor control, GitHub (https://github.com/BMClab/BMC).

Endo, E.T. & Murray, T., 1991. Real-time seismic amplitude measurement (RSAM): a volcano monitoring and prediction tool, *Bull. Volcanol.,* **53**(7), 533–545.

Fee, D. & Garces, M., 2007. Infrasonic tremor in the diffraction zone, *Geophys. Res. Lett.,* **34**(16), L16826.

Fee, D., Matoza, R.S., Gee, K.L., Neilsen, T.B. & Ogden, D.E., 2013. Infrasonic crackle and supersonic jet noise from the eruption of Nabro volcano, Eritrea, *Geophys. Res. Lett.,* **40,** 1–5.

Fee, D., Haney, M., Matoza, R., Szuberla, C., Lyons, J. & Waythomas, C., 2016a. Seismic envelope-based detection and location of ground-coupled airwaves from volcanoes in Alaska, *Bull. seism. Soc. Am.,* **106,** 3.

Fee, D., Matoza, R. & Jolly, A., 2016b. Yasur volcano temporary deployment, summer 2016 (data set), International Federation of Digital Seismograph Networks, doi:10.7914/SN/3E_2016.

Fee, D. *et al.*, 2021. Local explosion detection and infrasound localization by reverse time migration using 3-D finite-difference wave propagation, *Front. Earth Sci.,* **9,** 620813, doi:10.3389/feart.2021.620813.

Firth, C.W., Handley, H.K., Cronin, S.J. & Turner, S.P., 2014. The eruptive history and chemical stratigraphy of a post-caldera, steady-state volcano: Yasur, Vanuatu, *Bull. Volcanol.,* **76**(837), doi:10.1007/s00445–014–0837–3.

Fitzgerald, R.H. *et al.*, 2020. Volcanic ballistic projectile deposition from a continuously erupting volcano: Yasur volcano, Vanuatu, *Volcanica,* **3**(2), 183–204.

Garces, M.A., Hagerty, M.T. & Schwartz, S.Y., 1998. Magma acoustics and time-varying melt properties at Arenal Volcano, Costa Rica, *Geophys. Res. Lett.,* **25,** 2293–2296.

Gaudin, D., Taddeucci, J., Scarlato, P., Moroni, M., Freda, C., Gaeta, M. & Palladino, D., 2014. Pyroclast tracking velocimetry illuminates bomb ejection and explosion dynamics at Stromboli (Italy) and Yasur (Vanuatu) volcanoes, *J. geophys. Res.,* **119,** 5384–5397.

Gaudin, D. *et al.*, 2017. Integrating puffing and explosions in a general scheme for Strombolian-style activity, *J. geophys. Res.,* **122,** 1860–1875.

Gee, K.L., Sparrow, V.W., Atchley, A. & Gabrielson, T.B., 2007. On the perception of crackle in high-amplitude jet noise, *AIAA J.,* **45**(3), 593–598.

Global Volcanism Program, 2013. *Volcanoes of the World 4.5.3,* ed. Venzke, E., Smithsonian Institution, Downloaded 6 Nov 2014, doi:10.5479/si.GVP.VOTW4–2013.

Goldstein, P. & Chouet, B., 1994. Array measurements and modeling of sources of shallow volcanic tremor at Kilauea Volcano, Hawaii, *J. geophys. Res.,* **99,** 2637–2652.

Goto, A., Ripepe, M. & Lacanna, G., 2014. Wideband acoustic records of explosive volcanic eruptions at Stromboli: new insights on the explosive process and the acoustic source, *Geophys. Res. Lett.,* **41,** 3851–3857.

Green, D.N. & Neuberg, J., 2006. Waveform classification of volcanic low-frequency earthquake swarms and its implication at Soufriere Hills Volcano, Montserrat, *J. Volc. Geotherm. Res.,* **153,** 51–63.

Gudmundsson, A., 2002. Emplacement and arrest of sheets and dykes in central volcanoes, *J. Volc. Geotherm. Res.,* **116,** 279–298.

Gurioli, L., Colo, L., Bollasina, A.J., Harris, A.J.L., Whittington, A. & Ripepe, M., 2014. Dynamics of Strombolian explosions: inferences from field and laboratory studies of erupted bombs from Stromboli volcano, *J. geophys. Res.,* **119,** 319–345.

Haney, M.M., Chouet, B.A., Dawson, P.B. & Power, J.A., 2013. Source characterization for an explosion during the 2009 eruption of Redoubt Volcano from very-long-period seismic waves, *J. Volc. Geotherm. Res.,* **259,** 77–88.

Harris, A. & Ripepe, M., 2007. Synergy of multiple geophysical approaches to unravel explosive eruption conduit and source dynamics – a case study from Stromboli, *Geochemistry,* **67,** 1–35.

Hilgenfeldt, S., Arif, S. & Tsai, J.-C., 2008. Foam: a multiphase system with many facets, *Phil. Trans. R. Soc. A,* **366,** 2145–2159.

Hotovec, A.J., Prejean, S.G., Vidale, J.E. & Gomberg, J., 2013. Strongly gliding harmonic tremor during the 2009 eruption of Redoubt Volcano, *J. Volc. Geotherm. Res.,* **259,** 89–99.

Ichihara, M., Takeo, M., Yokoo, A., Oikawa, J. & Ohminato, T., 2012. Monitoring volcanic activity using correlation patterns between infrasound and ground motion, *Geophys. Res. Lett.,* **39,** L04304.

Iezzi, A.M., Fee, D., Kim, K., Jolly, A.D. & Matoza, R.S., 2019. Three-dimensional acoustic multipole waveform inversion at Yasur volcano, Vanuatu, *J. geophys. Res.,* **124,** 8679–8703.

Iezzi, A.M., Fee, D., Haney, M.M. & Lyons, J.J., 2020. Seismo-acoustic characterization of Mount Cleveland volcano explosions, *Front. Earth Sci.,* **24,** 573368.

Ishii, K., Yokoo, A., Kagiyama, T., Ohkura, T., Yoshikawa, S. & Inoue, H., 2019. Gas flow dynamics in the conduit of Strombolian explosions inferred from seismo-acoustic observations at Aso volcano, Japan, *Earth Planets Space,* **71,** 13.

James, M.R., Lane, S.J. & Chouet, B., 2006. Gas slug ascent through changes in conduit diameter: laboratory insights into a volcano-seismic source process in low-viscosity magmas, *J. geophys. Res.,* **111,** B05201.

James, M.R., Lane, S.J. & Corder, S.B., 2008. Modelling the rapid near-surface expansion of gas slugs in low-viscosity magmas, in *Fluid Motions in Volcanic Conduits: A Source of Seismic and Acoustic Signals,* Vol. 307, pp. 147–167, eds Lane, S.J. & ,Gilbert, J.S., Geological Society, London, Special Publications.

James, M.R., Lane, S.J., Wilson, L. & Corder, S.B., 2009. Degassing at low magma-viscosity volcanoes: quantifying the transition between passive bubble-burst and Strombolian eruption, *J. Volc. Geotherm. Res.,* **180,** 81–88.

Jolly, A., Lokmer, I., Christenson, B. & Thun, J., 2018. Relating gas ascent to eruption triggering for the April 27, 2016, White Island (Whakaari), New Zealand eruption sequence, *Earth Planets Space,* **70**(177), doi:10.1186/s40623–018–0948–8.

Jolly, A.D., Matoza, R.S., Fee, D., Kennedy, B.M., Iezzi, A.M., Fitzgerald, R.H., Austin, A.C. & Johnson, R., 2017. Capturing the acoustic radiation pattern of strombolian eruptions using infrasound sensors aboard a tethered aerostat, Yasur volcano, Vanuatu, *Geophys. Res. Lett.,* **44,** 9672–9680.

Kawakatsu, H. & Yamamoto, M., 2015. Volcano seismology, in *Treatise on Geophysics,* 2nd edn, Chap. 4.15, Vol. 4, pp., 389–419, ed. Schubert, G., Elsevier.

Koehler, S.A., Hilgenfeldt, S. & Stone, H.A., 2000. A generalized view of foam drainage: Experiment and theory, *Langmuir,* **16,** 6327–6341.

Kremers, S., Lavallée, Y., Hanson, J., Hess, K.U., Chevrel, M.O., Wassermann, J. & Dingwell, D.B., 2012. Shallow magma-mingling-driven Strombolian eruptions at Mt. Yasur volcano, Vanuatu, *Geophys. Res. Lett.,* **39,** L213047.

Kremers, S., Wassermann, J., Meier, K., Pelties, C., van Driel, M., Vasseur, J. & Hort, M., 2013. Inverting the source mechanism of Strombolian explosions at Mt. Yasur, Vanuatu, using a multi-parameter dataset, *J. Volc. Geotherm. Res.,* **262,** 104–122.

Krischer, L., Megies, T., Barsch, R., Beyreuther, M., Lecocq, T., Caudron, C. & Wassermann, J., 2015. ObsPy: a bridge for seismology into the scientific Python ecosystem, *Comput. Sci. Discovery,* **8,** 014003.

Kumagai, H. & Chouet, B.A., 2000. Acoustic properties of a crack containing magmatic or hydrothermal fluids, *J. geophys. Res.,* **105,** 25 493–25 512.

Kumagai, H., Chouet, B.A. & Nakano, M., 2002. Waveform inversion of oscillatory signatures in long-period events beneath volcanoes, *J. geophys. Res.,* **107,** 2301.

Lavallée, Y., Meredith, P.G., Dingwell, D.B., Hess, K.-U., Wassermann, J., Cordonnier, B., Gerik, A. & Kruhl, J.H., 2008. Seismogenic lavas and explosive eruption forecasting, *Nature,* **453,** 507–510.

Le Pichon, A., Blanc, E., Drob, D., Lambotte, S., Dessa, J.X., Lardy, M., Bani, P. & Vergniolle, S., 2005. Infrasound monitoring of volcanoes to probe high-altitude winds, *J. geophys. Res.,* **110,** D13106.

Le Pichon, A., Matoza, R., Brachet, N. & Cansi, Y., 2010. Recent enhancements of the PMCC infrasound signal detector, *Inframatics,* **26,** 5–8.

Liang, C., Karlstrom, L. & Dunham, E.M., 2020. Magma oscillations in a conduit-reservoir system, application to very long period (VLP) seismicity at basaltic volcanoes: 1. Theory, *J. geophys. Res.,* **125,** e2019JB017437.

Lyons, J.J. & Waite, G.P., 2011. Dynamics of explosive volcanism at Fuego volcano imaged with very long period seismicity, *J. geophys. Res.,* **116,** B09303.

Maeda, Y. & Kumagai, H., 2017. A generalized equation for the resonance frequencies of a fluid-filled crack, *Geophys. J. Int.,* **209,** 192–201.

Maeda, Y., Takeo, M. & Ohminato, T., 2011. A waveform inversion including tilt: method and simple tests, *Geophys. J. Int.,* **184,** 907–918.

Marchetti, E., Ripepe, M., Delle Donne, D., Genco, R., Finizola, A. & Garaebiti, E., 2013. Blast waves from violent explosive activity at Yasur Volcano, Vanuatu, *Geophys. Res. Lett.,* **40,** 5838–5843.

Matoza, R., Fee, D., Green, D. & Mialle, P., 2019a. Volcano infrasound and the International Monitoring System chapter 33, in *Infrasound Monitoring for Atmospheric Studies: Challenges in Middle-Atmosphere Dynamics and Societal Benefits,* chap. 33, pp. 1023–1077, eds Le Pichon, A., Blanc, E. & Hauchecorne, A., Springer.

Matoza, R.S. & Chouet, B., 2010. Subevents of long-period seismicity: implications for hydrothermal dynamics during the 2004–2008 eruption of Mount St. Helens, *J. geophys. Res.,* **115,** B12206.

Matoza, R.S. & Fee, D., 2014. Infrasonic component of volcano-seismic eruption tremor, *Geophys. Res. Lett.,* **41,** 964–1970.

Matoza, R.S., Shearer, P.M. & Okubo, P.G., 2014. High-precision relocation of long-period events beneath the summit region of Kilauea Volcano, Hawai'i, from 1986 to 2009, *Geophys. Res. Lett.,* **41,** 3413–3421.

Matoza, R.S., Chouet, B., Dawson, P.B., Shearer, P.M., Haney, M.M., Waite, G.P., Moran, S.C. & Mikesell, T.D., 2015. Source mechanism of small long-period events at Mount St. Helens in July 2005 using template matching, phase-weighted stacking, and full-waveform inversion, *J. geophys. Res.,* **120,** 6351–6364.

Matoza, R.S. *et al.*, 2017. Seismo-acoustic wavefield of strombolian explosions at Yasur volcano, Vanuatu, using a broadband seismo-acoustic network, infrasound arrays, and infrasonic sensors on tethered balloons, *J. acoust. Soc. Am.,* **141**(5), 3566–3566.

Matoza, R.S. *et al.*, 2018. Local, regional, and remote seismo-acoustic observations of the April 2015 VEI 4 eruption of Calbuco volcano, Chile, *J. geophys. Res.,* **123,** 3814–3827.

Matoza, R.S., Arciniega-Ceballos, A., Sanderson, R.W., Mendo-Pérez, G., Rosado-Fuentes, A. & Chouet, B.A., 2019b. High-broadband seismoacoustic signature of Vulcanian explosions at Popocatépetl volcano, Mexico, *Geophys. Res. Lett.,* **46,** 148–157.

Matoza, R.S., Garces, M.A., Chouet, B.A., D'Auria, L., Hedlin, M. A.H., De Groot-Hedlin, C. & Waite, G.P., 2009. The source of infrasound associated with long-period events at Mount St. Helens, *J. geophys. Res.,* **114,** B04305.

McNamara, D.E., Hutt, C.R., Gee, L.S., Benz, H.M. & Buland, R.P., 2009. A method to establish seismic noise baselines for automated station assessment, *Seismol. Res. Lett.,* **80**(4), 628–637.

Meier, K., Hort, M., Wassermann, J. & Garaebiti, E., 2016. Strombolian surface activity regimes at Yasur volcano, Vanuatu, as observed by Doppler radar, infrared camera and infrasound, *J. Volc. Geotherm. Res.,* **322,** 184–195.

Métrich, N. *et al.*, 2011. Magma and volatile supply to post-collapse volcanism and block resurgence in Siwi caldera (Tanna Island, Vanuatu arc), *J. Petrol.,* **52,** 1077–1105.

Nabyl, A., Dorel, J. & Lardy, M., 1997. A comparative study of low-frequency seismic signals recorded at Stromboli volcano, Italy, and at Yasur volcano, Vanuatu, *N.Z. J. Geol. Geophys.,* **40**(4), 549–558.

Nairn, I.A., Scott, B.J. & Giggenbach, W.F., 1988. Yasur volcano investigations, Vanuatu, September 1988, *N.Z. Geol. Surv. Rep. G,* **134,** 1–74.

Nakano, M. & Kumagai, H., 2005. Waveform inversion of volcano-seismic signals assuming possible source geometries, *Geophys. Res. Lett.,* **32,** L12302.

Nakano, M., Kumagai, H., Chouet, B. & Dawson, P., 2007. Waveform inversion of volcano-seismic signals for an extended source, *J. geophys. Res.,* **112,** B02306.

Nichols, J.W., Lele, S.K., Ham, F.E., Martens, S. & Spyropoulos, J.T., 2013. Crackle noise in heated supersonic jets, *ASME J. Eng. Gas Turbines Power,* **135**(5), 051202.

Ohminato, T. & Chouet, B.A., 1997. A free-surface boundary condition for including 3D topography in the finite-difference method, *Bull. seism. Soc. Am.,* **87,** 494–515.

Ohminato, T., Chouet, B.A., Dawson, P.B. & Kedar, S., 1998. Waveform inversion of very-long-period impulsive signals associated with magmatic injection beneath Kilauea Volcano, Hawaii, *J. geophys. Res.,* **103,** 23 839–23 862.

Oppenheimer, C., Bani, P., Calkins, J.A., Burton, M.R. & Sawyer, G.M., 2006. Rapid FTIR sensing of volcanic gasses released by Strombolian explosions at Yasur volcano, Vanuatu, *Appl. Phys. B,* **85,** 453–460.

Oppenheimer, J., Capponi, A., Cashman, K.V., Lane, S.J., Rust, A.C. & James, M.R., 2020. Analogue experiments on the rise of large bubbles through a solids-rich suspension: a "weak plug" model for Strombolian eruptions, *Earth planet. Sci. Lett.,* **531,** 115931.

Patrick, M., Wilson, D., Fee, D., Orr, T. & Swanson, D., 2011. Shallow degassing events as a trigger for very-long-period seismicity at Kilauea volcano, Hawai'i, *Bull. Volcanol.,* **73,** 1179–1186.

Patrick, M.R., Harris, A.J.L., Ripepe, M., Dehn, J., Rothery, D.A. & Calvari, S., 2007. Strombolian explosive styles and source conditions: insights from thermal (FLIR) video, *Bull. Volcanol.,* **69,** 769–784.

Perret, F.A., 1950. *Volcanological Observations,* Carnegie Inst. Wash. Publ.

Perrier, L., Métaxian, J.-P., Battaglia, J. & Garaebiti, E., 2012. Estimation of the near-surface velocity structure of the Yasur-Yenkahe volcanic complex, Vanuatu, *J. Volc. Geotherm. Res.,* **227–228,** 50–60.

Petersen, T., 2007. Swarms of repeating long-period earthquakes at Shishaldin Volcano, Alaska, 2001–2004, *J. Volc. Geotherm. Res.,* **166,** 177–192.

Powell, T.W. & Neuberg, J., 2003. Time dependent features in tremor spectra, *J. Volc. Geotherm. Res.,* **128**(1–3), 177–185.

Ripepe, M., Ciliberto, S. & Della Schiava, M., 2001. Time constraints for modeling source dynamics of volcanic explosions at Stromboli, *J. geophys. Res.,* **106**(B5), 8713–8727.

Ripepe, M., Marchetti, E., Ulivieri, G., Harris, A., Dehn, J., Burton, M., Caltabiano, T. & Salerno, G., 2005. Effusive to explosive transition during the 2003 eruption of Stromboli volcano, *Geology,* **33**(5), 341–344.

Rodgers, M., Rodgers, S. & Roman, D.C., 2015. Peakmatch: a Java program for multiplet analysis of large seismic datasets, *J. Volc. Geotherm. Res.,* **86,** 1208–1218.

Rowell, C.R., Fee, D., Szuberla, C.A.L., Arnoult, K., Matoza, R.S., Firstov, P.P., Kim, K. & Makhmudov, E., 2014. Three-dimensional volcano-acoustic source localization at Karymsky Volcano, Kamchatka, Russia, *J. Volc. Geotherm. Res.,* **283,** 101–115.

Rubin, A.M., 1995. Propagation of magma-filled cracks, *Annu. Rev. Earth planet. Sci.,* **23:1,** 287–336.

Ruiz, M.C., Lees, J.M. & Johnson, J.B., 2006. Source constraints of Tungurahua volcano explosion events, *Bull. Volcanol.,* **68,** 480–490.

Scheu, B., Spieler, O. & Dingwell, D.B., 2006. Dynamics of explosive volcanism at Unzen volcano: an experimental contribution, *Bull. Volcanol.,* **69,** 175–187.

Schipper, C.I. *et al.*, 2021. Silicic conduits as supersized tuffisites: Clastogenic influences on shifting eruption styles at Cordón Caulle volcano (Chile), *Bull. Volcanol.,* **83,** 11.

Simons, B.C., Cronin, S.J., Eccles, J.D., Bebbington, M.S. & Jolly, A.D., 2020a. Spatiotemporal variations in eruption style, magnitude and vent morphology at Yasur volcano, Vanuatu: insights into the conduit system, *Bull. Volcanol.,* **82**(59), 1–22.

Simons, B.C., Jolly, A.D., Eccles, J.D. & Cronin, S.J., 2020b. Spatiotemporal relationships between two closely-spaced strombolian-style vents, Yasur, Vanuatu, *Geophys. Res. Lett.,* **47,** e2019GL085687.

Sneddon, I.N. & Lowengrub, M., 1969. *Crack Problems in the Classical Theory of Elasticity,* John Wiley.

Spina, L., Scheu, B., Cimarelli, C., Arciniega-Ceballos, A. & Dingwell, D.B., 2016a. Time scales of foam stability in shallow conduits: Insights from analogue experiments, *Geochem. Geophys. Geosyst.,* **17**(10), 4179–4194.

Spina, L. *et al.*, 2016b. Explosive volcanic activity at Mt. Yasur: a characterization of the acoustic events (9–12th July 2011), *J. Volc. Geotherm. Res.,* **322,** 175–183.

Stephens, C.D. & Chouet, B.A., 2001. Evolution of the December 14, 1989 precursory long-period event swarm at Redoubt Volcano, Alaska, *J. Volc. Geotherm. Res.,* **109,** 133–148.

Vergniolle, S. & Métrich, N., 2016. A bird's eye view of "Understanding volcanoes in the Vanuatu arc", *J. Volc. Geotherm. Res.,* **322,** 1–5.

Waite, G.P., Chouet, B.A. & Dawson, P.B., 2008. Eruption dynamics at Mount St. Helens imaged from broadband seismic waveforms: Interaction of the shallow magmatic and hydrothermal systems, *J. geophys. Res.,* **113,** B02305.

Weaire, D. & Hutzler, S., 1999. *The Physics of Foams,* Clarendon Press.

Wessel, P. & Smith, W.H.F., 1991. Free software helps map and display data, *EOS, Trans. Am. geophys. Un.,* **72**(41), 441–446.

Withers, M., Aster, R., Young, C., Beiriger, J., Harris, M., Moore, S. & Trujillo, J., 1998. A comparison of select trigger algorithms for automated global seismic phase and event detection, *Bull. seism. Soc. Am.,* **88**(1), 95–106.

Woitischek, J., Woods, A.W., Edmonds, M., Oppenheimer, C., Aiuppa, A., Pering, T.D., Ilanko, T., D'Aleo, R. & Garaebiti, E., 2020. Strombolian eruptions and dynamics of magma degassing at Yasur volcano (Vanuatu), *J. Volc. Geotherm. Res.,* **398,** 106869.

SUPPLEMENTARY INFORMATION

Supplementary data are available at *GJI* online.

Figure S1: Waveform data availability for the temporary broadband network (a) seismic and (b) infrasound stations (see Fig. 1 of main text). All times in UT. Horizontal blue lines indicate times of recorded waveform data. Vertical red bars indicate brief gaps (data checks during field deployment). Percentage availability is indicated for each channel relative to its total recording time.

Figure S2: As for Fig. 4(a) of main text, but for station YIF1 (Fig. 1) on the north side of the crater. Here we show unfiltered waveforms (helicorder plot) at YIF1 (channel CDF) for 3 full days from 00:00 30 July to 00:00 2 August 2016. The infrasound event amplitude increase is consistent with that observed at YIB22 (Fig. 4) to the south of the source.

Figure S3: Waveforms at station YS01 (vertical component, HHZ) of the 9 most populous multiplets that all contain at least 100 events each (see Section 3.3.3). Each row of the matrix displayed as an image is the waveform of a different event, with red indicating positive amplitude and blue indicating negative amplitude. Waveforms are unfiltered and normalized by their peak waveform amplitude. Waveforms are aligned on their peak amplitude (picked using the peak detection algorithm), which is set to $t = 0$ for this display. Here we display the waveforms from -10 to $+60$ s around the picked peak amplitude, but we emphasize that the multiplet analysis (see Section 3.3.3 for the details) used a window of -10 to $+20$ s around the picked peak amplitude for the cross-correlation windows. The multiplets are ranked by population: multiplet #1 (932 events), multiplet #2 (922 events), multiplet #3 (273 events), multiplet #4 (212 events), multiplet #5 (190 events), multiplet #6 (137 events), multiplet #7 (136 events), multiplet #8 (131 events), multiplet #9 (113 events). All other multiplets have fewer than 100 events. (a) Zoom on multiplets #1 and #2 only; (b) Multiplets #1 to #9. Horizontal dashed lines separate the different multiplets. Multiplets #1 and #2 are similar to each other, but significantly different from other multiplets. Note also the consistent protracted waveform features visible to 60 s in most cases.

Figure S4: As for Figs 7(f) and (g) of the main text, but using a lower correlation coefficient threshold $r \geq 0.65$ to define the template detection (see Fig. 7e). This figure uses the same template and identical methodology and parameters as used in Fig. 7 and the main text, but with a lower threshold $r \geq 0.65$ used here compared to $r \geq 0.75$ used in the main text and Fig. 7. In this case, 1264 events are detected with $r \geq 0.65$ compared to the 597 events with $r \geq 0.75$. All waveforms are unfiltered and the stack is a normalized mean (linear) stack.

Figure S5: As for Figs 11(a)–(f) of main text, but for infrasonic event timings and amplitudes picked using Method (2) described in Section 3.6.2 of the main text. Method (2) picks the first occurring infrasonic peak with amplitude threshold >10 Pa that occurs after the onset of the seismic VLP waveform. Figs S5e,f here are identical to Figs 11(h) and (i), respectively in the main text. Figs S5b,c differ from Figs 11(b) and (c) in that the infrasonic amplitude is based on the infrasound event picked using Method (2).

Figure S6: Inversion comparison with and without station YS07. Source–time functions for the minimum E_2 free-inversion solution in each case for (a) a multiplet stack formed from data during the day of 31 July 2016 (without station YS07) and (b) a multiplet stack formed from data during the day of 29 July 2016 (with station YS07). For (a) the template matching and stacking was based on a seed template at 02:09:45, 31 July 2016 UT. For (b) the template matching and stacking was based on a seed template at 14:32:43, 29 July 2016 UT. The results for (a) 31 July 2016 and (b) 29 July 2016 are remarkably similar and consistent, giving confidence in the results. These stacks represent independent samples of the data – stacks from different days of non-overlapping data with a different seed event chosen in each case (although both seeds belong in the dominant multiplet considered in the main manuscript). Data and inversion for 2016 July 29 include data from station YS07 while data from 2016 July 31 do not, demonstrating relative robustness to the loss of this station.

Figure S7: Phase velocity v_m of the crack wave as a function of crack stiffness $C = (b/\mu)(L/d)$ for modes $m = 2$ to $m = 10$ using the formulation of Maeda & Kumagai (2017) (Appendix B). We assume a square crack $L = W = 800$ m and acoustic velocity $v_a = 2000$ m s^{-1} for liquid basalt. See Appendix B for explanation of symbols. (b) is the same as (a), but with a logarithmic axis for crack stiffness.

Movie M1: DJI Phantom 3 UAS movie compared with waveforms from ground-based and collocated broad-band seismic station YS01 (vertical component velocity) and infrasound station YIB22 (see Fig. 1 of the main text for station location). The view is from approximately southeast looking toward northwest, with the North Crater shown to the right and South Crater to the left. The movie start time is 22:43:50, 31 July 2016 UT. Waveforms are displayed unfiltered and at absolute recording time with no traveltime correction. On the waveforms, a solid yellow bar tracks actual time synchronized with video; the dashed bar on the infrasound trace indicates an approximate traveltime to the station assuming 340 m s^{-1} velocity. The 30 s clip begins with low-level ash venting at North Crater linked to low-amplitude infrasonic tremor, which is followed by a violent explosion at South Crater. The sequence is the same as that displayed in Fig. 2 of the main text. Note the spattering and oscillations at South Crater associated with the onset of the seismic VLP and prior to the main explosive blast. This seismic VLP event does not belong in the dominant VLP multiplet and is likely a shallow magma oscillation and explosion signature; reliable mechanisms for this particular VLP could not be obtained through waveform inversion.

Movie M2: As for Movie M1 but showing a longer time sequence: the movie start time is 22:43:00, 31 July 2016 UT in this case. We show here also the waveform from crater infrasound station YIF3 (approximately 280 m from crater centre) (see Fig. 1 of the main text for station locations). The longer movie sequence and closer range infrasound data better show the relation between ash venting at the North Crater and low-amplitude infrasonic tremor.

Movie M3: Similar to Movies M1 and M2, but showing a 6-min time window beginning at 06:39:33, 31 July 2016 UT. The view is approximately from the east toward west, with the North Crater shown to the right and South Crater to the left. Waveforms are displayed unfiltered and at absolute recording time with no traveltime correction. We show waveforms from broad-band station YS01 (vertical component velocity), infrasound station YIB21 (approximately 630 m from crater centre), and crater infrasound station YIF3 (approximately 280 m from crater centre) (see Fig. 1 of the main text for station locations). On the waveforms, a solid yellow bar tracks actual time synchronized with video; the dashed bars on the infrasound traces indicate an approximate traveltime to the stations assuming 340 m s^{-1} velocity. Seismic VLP events highlighted in cyan on the YS01-HHZ trace are events belonging to the dominant seismic VLP multiplet as determined by template matching. Correlation-coefficient values with the main seed event based on a 66 s waveform are: 0.88, 0.88, and 0.82, respectively. The infrasound signal during this time is low-amplitude, and corresponds to the relatively minor spattering activity at both vents captured in the video. The amplitude scale of the infrasound traces was chosen to be the same as that shown in Movie M1 for direct comparison. Note

that the closer infrasound station YIF3 records the low-amplitude spattering activity more clearly. The low-level spattering activity appears related to minor VLP events, particularly during the intervals 0–90 s and 250–300 s in the displayed sequence. The time-window covered by this movie begins shortly after the time covered by Fig. 9(b) of the main text, providing a clear physical explanation for the infrasound signals shown in Fig. 9(b).

Movie M4: Movie from GoPro camera on crater, showing an 80 s time window beginning at 23:17:50, 31 July 2016 UT, corresponding to the time-range of Fig. 9(c) of the main text. View is approximately from south to north, with the south crater in the foreground, from which two explosions (moderate ballistic eruptions) occur. The waveforms from seismic station YS01 (vertical component velocity) and infrasound stations YIB22 and YIF5 (see Fig. 1 of the main text for station locations) are also shown. On the waveforms, a solid yellow bar tracks actual time synchronized with video; the dashed bars on the infrasound traces indicate an approximate traveltime to the stations assuming 340 m s^{-1} velocity. This movie includes an audio recording from the microphone on the GoPro camera, which captures audible sounds from the explosions. The VLP seismic event shown here at ∼20 s (same as Fig. 9c) is accompanied by a powerful infrasonic explosion signal, which also produces additional higher frequency components in the seismic waveform. Visibility in this video clip is limited by a thick opaque gas and ash plume occupying the summit craters at this time from prior explosions and degassing, and obscuring the active vents. However, a moderate ballistic eruption is confirmed by a strong audible explosion sound on the GoPro audio channel, a visible shock wave passing through the gas plume, and ballistics launched above the gas plume and landing on the lower crater rim in the video foreground. The second explosion at ∼63 s is more visible in the video.

Please note: Oxford University Press is not responsible for the content or functionality of any supporting materials supplied by the authors. Any queries (other than missing material) should be directed to the corresponding author for the paper.

APPENDIX A: FULL-WAVEFORM INVERSION METHODOLOGY

We apply full seismic waveform inversion for a point-source moment-tensor and single-force vector representation of the VLP source. The representation theorem for this source is written (Chouet 1996):

$$u_n(\underline{x}, t) = M_{pq}(t) * G_{np,q}(\underline{x}, t) + F_p(t) * G_{np}(\underline{x}, t), \tag{A1}$$

where the summation convention is assumed (p, $q = 1, 2, 3$), u_n is the nth-component of displacement at receiver location $\underline{x}$ and time t, $F_p(t)$ is the time-history of a single-force applied in the p-direction at the source, $M_{pq}(t)$ is the time-history of the pqth-component of the moment-tensor, and $G_{np}(\underline{x}, t)$ is the tensor of elastodynamic Green's functions relating the nth-component of displacement at the receiver at $\underline{x}$ to the pth-component of force applied at the source (the notation '$,q$' denotes spatial differentiation with respect to q). The frequency-domain matrix form of eq. (A1) is:

$$\mathbf{U}(\omega) = \mathbf{G}(\omega)\mathbf{S}(\omega), \tag{A2}$$

where $\mathbf{U}$ is the $N_\tau \times 1$ vector of Fourier-transformed ground displacement components, $\mathbf{G}$ is the $N_\tau \times 9$ matrix of Fourier transforms of synthetic Green's functions, $\mathbf{S}$ is the 9×1 vector of Fourier-transformed force and moment-tensor components, and N_τ is the number of observed seismic traces. Eq. (A2) is of form $\mathbf{d} = \mathbf{Gm}$, which we invert separately for each frequency, recombining the results with inverse Fourier transforms to obtain the desired time-domain solutions (Auger *et al.* 2006). We invert velocity data then integrate the resulting source–time functions to obtain moment and force functions.

The elementary source–time functions used in the Green's function calculations using finite differences and in the waveform inversion procedure are:

$$s(t) = \begin{cases} \frac{1}{2}\left[1 - \cos\left(\frac{2\pi t}{t_p}\right)\right], & 0 \le t \le t_p \\ 0, & t > t_p, \end{cases} \tag{A3}$$

where $t_p = 0.25$ s, a value appropriate for producing stable results for the 10-m grid spacing used.

Since the point-source location is not known *a priori*, we repeat the inversion at multiple trial source nodes and evaluate the best-fit source centroid. To compute Green's functions for multiple trial source nodes, we exploit reciprocity between source and receiver (Chouet *et al.* 2005). We evaluate the solutions using the squared error, the relevance of the free parameters, and the temporal stability of the derived source mechanisms (consistency in derived source–time functions for individual moment and single-force components).

We use two measures of squared error (Ohminato *et al.* 1998; Chouet *et al.* 2003):

$$E_1 = \frac{\sum_{n=1}^{N_\tau}\sum_{p=1}^{N_s}(u_n^o(p\Delta t) - u_n^s(p\Delta t))^2}{\sum_{n=1}^{N_\tau}\sum_{p=1}^{N_s}(u_n^o(p\Delta t))^2}, \tag{A4}$$

and

$$E_2 = \frac{1}{N_r}\sum_{n=1}^{N_r}\left[\frac{\sum_{j=1}^{3}\sum_{p=1}^{N_s}(u_{n,j}^o(p\Delta t) - u_{n,j}^s(p\Delta t))^2}{\sum_{j=1}^{3}\sum_{p=1}^{N_s}(u_{n,j}^o(p\Delta t))^2}\right], \tag{A5}$$

where $u_n^o(p\Delta t)$ is the pth sample of the nth data trace, $u_n^s(p\Delta t)$ is the pth sample of the nth synthetic trace, N_τ is the number of data traces, N_s is the number of samples in each trace, N_r is the number of three-component receivers, and j represents the 3 receiver components in eq. (A5). E_2 weights each station equally because the error is normalized by station, while E_1 is not normalized by station and thus emphasizes the fit on nearby stations that record higher amplitudes. We primarily use the E_2 measure, but our solutions based on E_2 and E_1 are consistent. We repeat the inversions for a varying number of assumed mechanisms, $N_m = [9; 6; 3]$, implying [6 independent moments + 3 forces; 6 moments; and 3 forces], respectively; where N_m is the number of source mechanism components, and evaluate the significance of the number of free parameters using Akaike's information criterion (AIC) (Akaike 1974):

$$\mathrm{AIC} = N_\tau N_s \ln E_2 + 2N_m N_f, \tag{A6}$$

where N_f is the number of frequencies used in the inversion, and E_2 is the residual error (eq. A5).

In Section 4.3, we further evaluate the volumetric source–time-function phase stability by performing a point-by-point eigenvector decomposition of the moment-tensor source–time functions and evaluating (Matoza *et al.* 2015):

$$\gamma = [\sigma^2(2\frac{\alpha_1}{\alpha_3}) + \sigma^2(2\frac{\alpha_2}{\alpha_3})]^{\frac{1}{2}}, \tag{A7}$$

where σ is the standard deviation (over the history of the source–time function) and α_1, α_2 and α_3 are the minimum, intermediate, and maximum moment-tensor eigenvalues, respectively. Normalization with 2 assumes $\lambda = 2\mu$. Low values of γ correspond to a temporally stable volumetric moment tensor (in-phase eigenvector source–time-functions).

APPENDIX B: CRACK-WAVE VELOCITY

In Section 5.3, we consider a shallow-buffered top-down model. Slug disruption in the shallow zone triggers a pressure disturbance that propagates downward at the speed of the crack wave (Kumagai & Chouet 2000; Chouet 1988) and couples at the geometrical discontinuity at the base of the conduit (VLP centroid). We estimate crack-wave velocities using the formulation of Maeda & Kumagai (2017), who provide analytical formulas of resonance frequencies for both longitudinal and transverse modes of a resonating rectangular fluid-filled crack. At Yasur, the intermediate magma transport section may be a vertical conduit of length z_M (Figs 16 and 18).

For a first-order estimate using the formulation of Maeda & Kumagai (2017), we assume a vertical crack with a square geometry with crack length L and width W ($W = L$), for which longitudinal and transverse resonance frequencies are equal and given by (Maeda & Kumagai 2017):

$$f_m = \frac{(m-1)v_a}{2L\sqrt{1+2\epsilon_m C}}, \tag{B1}$$

where m represents the mode number, v_a is the acoustic velocity of the liquid ($v_a = 2000$ m s^{-1} for liquid basalt), C is the crack stiffness ($C = (b/\mu)(L/d)$, where b is the fluid bulk modulus, μ is the elastic shear modulus, and d is the crack aperture; Chouet (1988)), and ϵ_m is a constant depending on the ratio W/L (here equal to 1) and m. An analytical expression for the constant ϵ_m is derived in Maeda & Kumagai (2017); for the case $W/L = 1$, this expression becomes:

$$\epsilon_m = \frac{1}{3m}\left[1 - \frac{4\Gamma}{3m}\right], \tag{B2}$$

where $\Gamma = 0.22$. The wavelengths associated with each mode are:

$$\lambda_m = \frac{2L}{m}. \tag{B3}$$

Assuming a crack length $L = 800$ m (Section 5.3), we calculate dispersion curves for the modes from $m = 2$ to $m = 10$ (Supporting Information Fig. S7). For $m = 2$, $\lambda_m = 800$ meters; for $m = 10$, $\lambda_m = 160$ meters. Using the above expressions for f_m and λ_m, the associated phase-velocity of the crack wave is:

$$v_m = f_m \lambda_m = \frac{(m-1)v_a}{m\sqrt{1+2\epsilon_m C}}. \tag{B4}$$

We note that the m used here denotes the mode number, while in Section 5.3 we use the subscript M for a general representative crack-wave speed of the intermediate magma transport section v_M. In the above formulation, v_m is invariant to the assumed length L, but resonant frequency f_m depends on L. For the illustrative crack stiffness $C = 50$ used in Section 5.3, assuming $b/\mu = 0.1$ with length $L = 800$ m results in a crack aperture $d \sim 0.6$ m.